UNIVERSITY OF THE FREE STATE
UNIVERSITEIT VAN DIE VRYSTAAT
YUNIVESITHI YA FREISTATA

MONTE CARLO STUDY ON MEGAVOLT X-RAY THERAPY FOR DEVELOPMENT OF SUITABLE TARGETS FOR THE EVALUATION OF NANO PARTICLE DOSE ENHANCEMENT

A Dissertation

Presented to

The Academic Faculty

By

Stalyn Mutsakanyi

University of The Free State, September 2016

Bloemfontein, South Africa

Supervisor: Dr. FCP Du Plessis

In Fulfilment

of the Requirements for the Degree

Masters of Science in Medical Physics, University of the Free State

DECLARATION

I declare that all of the work contained within this document is my own, with the exception of incidents where I have specifically cited or references the works of others. This work is solely mine, and has not previously been submitted for at another university or faculty. All research carried out in pursuit of this project was carried out within the guidelines of the ethical standards of University of the Free State.

Stalyn Mutsakanyi September 2016

ACKNOWLEDGEMENTS

First and foremost, I would like to thank my advisor, Dr. FCP Du Plessis, for his insight and direction as the ideas for this work developed, and for his continued guidance and support throughout my time at the University of the Free State. His academic guidance he offered me has proven to be invaluable throughout the course of this study .

I would like to avail the opportunity to thank Prof W Rae for his support and encouragement. He has always been there to respond my challenges I encountered throughout the study. I believe, without him my stay at University of the Free State was going to be very difficult.

I must not forget to acknowledge Mr C Mahuvava for his friendship, ideas, encouragement, support and trust. I am grateful to all my friends and colleagues in the Medical Physics department and more specifically to Mr L Strauss, Mr I Setilo, Dr W Shaw, Mr C Smith, Mrs D O'Reilly, Mr M Oderinde, Mr F Makosa and Mr L Netshivhera, thanks so much for your patients and ideas.

I am indebted to the South African Medical Research Council (MRC) for the HARD bursary award with funds from National Treasury under its Economic Competitiveness and Support Package for its support and commitment in allowing me to undertake this study. This research and the publication thereof is the result of funding provided by the MRC of South Africa in terms of the MRC's Flagship Awards Project SAMRC-RFA-UFSP-01-2013/HARD.

I would like to express my sincere gratitude and appreciation to my parents for their everlasting love and prayers. And finally, none of this would have been possible without the love and support of my wife, Pauline and son, Tinaye as I strove to complete this work.

To all others that I did not mention, I extend my deepest gratitude and appreciation. It was a pleasure having all of you as a working team.

ABSTRACT

INTRODUCTION: Radiation dose enhancement with nanoparticles is a treatment technique involving the irradiation of tumour seeded with high atomic number (high Z) material. This work describes the generation of x-ray beams using a 6 MeV Elekta Precise linac head using low-Z Bremsstrahlung target materials, water and carbon combined with tungsten. The aim of the study was to simulate photon energy spectra appropriate for high-Z nanoparticles dose enhancement in tumour using EGSnrc MC codes.

MATERIALS AND METHOD: BEAMnrc Monte Carlo (MC) code successfully modelled the treatment head components of a flattening filter free 6 MV Elekta Precise linear accelerator. Simulations were run using suitable histories to generate high energy x-ray beams of differing quality from electron spectra obtained using 6 MeV electron beam. Water and carbon layers were the primary target which were inserted in the path of the 6 MeV electron pencil beam before it hits the tungsten Bremsstrahlung target to act as moderators that slow down electron before they hit a tungsten layer. The electron spectra obtained just after the primary target was used as the incident beam to the tungsten target which acts as the secondary target to generate x-ray photon beams. Therefore the x-ray beam source target was either water/tungsten or carbon/tungsten combination. Different photon spectra were obtained for investigation in nanoparticles (NPs) based photon therapy. An original linac using a normal tungsten target of 0.3 cm thickness was also simulated to benchmark the results. The photon spectra obtained below X,Y jaws were used as input sources in the DOSXYZnrc MC code to simulate dose distribution in water and a patient CT phantom. The simulations were carried out using source 2 in DOSXYZnrc.

A 40 x 40 x 40 cm^3 water phantom was simulated at 100 cm SSD using a range of field sizes to characterize the beams. The phantom had voxel size of 0.2 × 0.2 × 0.2 cm^3. The photon beams were characterised in terms of percentage depth doses and beam profiles. These x-ray beams were then used to quantify the variation of tumour dose enhancement in a constructed patient CT phantom. The prostate tumour was used as the planning target volume (PTV). The PTV

composition was either a tumour only or a tumour volume seeded with atoms of gold nanoparticles with concentration of 7mg/g of tumour.

These tumour/NPs model was manually drawn on to the CT dataset from actual CT images of the patient using MCSHOW graphical user interface (GUI). The tumour composition was made part of the patient CT data set using a locally-developed Interactive Data Language (IDL) code that converts the density of the drawn volume into the desired tumour density. The 3DCRT was used as the treatment strategy and 4, 5 and 6 field beams were investigated. With this model, we were able to estimate more accurately the effect of altered beams on NPs radiation dose enhancement. For both simulations using BEAMnrc and DOSXYZnrc the electron cut-off energy (ECUT) and photon cut-off energy (PCUT) was 0.521 MeV and 0.01 MeV respectively. The number of histories was chosen so that the statistical uncertainty along the CAX had an average value of 1% at 0 – 30 cm depth.

RESULTS AND CONCLUSION: The results showed that the use of electron moderators in generating x-ray beams for use in NPs seeded tumours can lead to a significant dose enhancement. Photon spectra obtained with water/tungsten or carbon/tungsten Bremsstrahlung targets combinations showed significant changes at various target thickness. There is a significant dependence of dose enhancement factors (DEF) on the mean energy of the x-ray beams as well as the target thickness. DEFs ranging from 0.05% to 7.5% were obtained at various Bremsstrahlung target combinations. Based on the results, carbon is more efficient at moderating the electron beam to generate photon beams for dose enhancement at lower thickness (approximately 1.4 cm) compared to water (approximately 2.5 cm), although water can just be as good at larger thickness. At these thicknesses the mean photon beam energy is approximately 0.4 MV. In summary, the results of this work indicate that the use of photon beams from low-Z Bremsstrahlung targets as electron slowing down medium could enable significant clinical dose enhancement during external beam radiotherapy for NPs seeded tumours. MC techniques showed to be valuable tools for dose calculations in both water and patient CT phantom.

Key words: **Monte Carlo • dose enhancement • nanoparticles • Bremsstrahlung target**

ABBREVIATIONS AND SYMMBOLS

3D	Three-dimensional
4F	Four-field
5F	Five-field
6F	Six-field
3DCRT	Three-dimensional conformal radiation therapy
AAPM	American Association of Physicists in Medicine
ACA	Adenocarcinoma
AP	Anterior-posterior
Au	Gold
AuNPs	Gold nanoparticles
BE	Binding energy
BEAMDP	BEAM Data Processor
BS	Bremsstrahlung splitting
C	Carbon
CAX	Central axis
CEMA	Converted energy per unit mass
CM	Component module
CPE	Charged particle equilibrium
CS	Compton scattering
CSDA	Continuous slowing-down approximation
CT	Computed tomography
D	Absorbed dose
DC	Direct current
DP	Dose profile
DBS	Directional Bremsstrahlung splitting

DEF	Dose enhancement factor
DICOM	Digital Imaging and Communications in Medicine
DNA	Deoxyribonucleic acid
DVH	Dose volume histogram
EBRT	External beam radiation therapy
ECUT	Global electron energy cut-off
EGS4	Electron Gamma Shower v4.0
EGSnrc	Electron Gamma Shower National Research Council of Canada
EGSnrcMP	Multi-platform environment for EGSnrc
EPR	Enhanced penetration and retention
ETAR	Equivalent tissue-air ratio
FF	Flattening Filter
FFF	Flattening Filter Free
FS	Field Size
Gd	Gadolinium
GEANT4	GEometry ANd Tracking 4
GUI	Graphical user interface
High-Z	High Atomic Number
I	Iodine
IAEA	International Atomic Energy Agency
ICRU	International Commission on Radiation Units and Measurements
IDL	Interactive Data Language
IMRT	Intensity modulated radiation therapy
IPEM	Institute of Physics and Engineering in Medicine
K_{col}	Collision kerma
KE	Kinetic energy

KERMA	Kinetic energy released per unit mass
LINAC	Linear accelerator
MC	Monte Carlo
MCNP	Monte Carlo N-Particle Transport Code
MLC	Multi-leaf collimator
MRI	Magnetic resonance imaging
MRT	Microbeam radiation therapy
MV	Megavoltage
N	Histories
NPs	Nanoparticles
NRC	National Research Council
OMEGA	Ottawa Madison Electron Gamma Algorithm
PA	Posterior-anterior
PCUT	Global photon energy cut-off
PDD	Percentage depth dose
PDFs	Probability distribution functions
PEA	Photoelectric absorption
PEGS4	Pre-processor for Electron Gamma Shower v4.0
PENELOPE	Penetration and ENErgy Loss of Positrons and Electrons
PP	Pair Production
PS	Phase space
Pt	Platinum
PTV	Planning target volume
RT	Radiotherapy
SAD	Source to Axis Distance
SSD	Source to Surface Distance

SLAC	Stanford Linear Accelerator Centre
SRS	Stereotactic radiation therapy
T	Simulation time
TCPE	Transient charged particle equilibrium
TNF	Tumour necrotic factor
TP	Treatment planning
TPS	Treatment planning system
TRS	Technical reports series
VEGF	Vascular endothelia growth factor
Voxel	Volume element
W	Tungsten
Z	Atomic number
Z_{max}	Depth of maximum dose

Dissertation Overview

Chapter 1 gives a general introduction to cancer disease and the use of radiation as a method of treatment. The issue of the combination low megavolt x-ray radiation and nanoparticles (NPs) to enhance the tumour treatment dose is raised. The applications of Monte Carlo (MC) simulations to evaluate NPs dose enhancement is introduced as well as the codes that are going to be used in this study. The aims of the study are also presented.

Chapter 2 provides information on the physics of photon interaction with matter, focusing mainly on x-rays and their production. It will explain the processes that take place during radiation interactions and their implications in radiation dosimetry. Some dosimetric quantities in radiation therapy will also be defined in this chapter.

Chapter 3 provides a discussion on the MC technique. It discusses the history and the motivation of using EGSnrc based MC codes to simulate radiation transport and provides detailed clinical applications of MC techniques in simulating NP dose enhancement in tumours.

Chapter 4 discusses the use of nanoparticles to enhance tumour dose during radiotherapy. It will provide the history of the usage of NPs and the progress made in the field of medicine. The chapter will explain the physics of tumour dose enhancement.

Chapter 5 provides information on the materials and methods used to carry out this study. The chapter will provide detailed information on how the EGSnrc MC codes, BEAMnrc, DOSXYZnrc and BEAMDP and other software packages and hardware tools where used to carry out the study. It explains the design of the patient CT phantom model and its manipulation to introduce a tumour seeded with nanoparticles. The modelling of the tumour with and without NPs is explained. All the dosimetric parameters to evaluate NPs dose enhance are defined and also how they will be implemented to analyze the results that will enable the discussion, conclusions and future developments of the study.

Chapter 6 provides a detailed summary of results and discussions.

Chapter 7 provides the conclusions of the study as well as future development to consider in NPs dose enhancement.

CONTENTS

LIST OF FIGURES

LIST OF TABLES

Chapter 1: INTRODUCTION

1.1 Introduction

Worldwide cancer is one of the leading causes of death and much effort is invested to come up with optimized treatment techniques. One such method is using x-ray photon irradiation of tumours injected with carbon nanoparticles (NPs) which contains high atomic (Z) number materials such as gold (Au) and platinum (Pt). This will increase interactions with an increased release of secondary electrons resulting in an enhancement of tumour dose.[1]. The DNA will be exposed to a higher flux of generated electrons, increasing in turn the probability of fatal damage. The interaction of photons with NPs can be considered important in terms of local dose enhancement. Therefore it is important to have an understanding of the characteristics of the x-rays generated in the Bremsstrahlung target. The most important characteristic will be the energy spectral distribution.

1.2. Cancer

Cancer can be defined broadly as the uncontrollable growth and spread of cells in an organism. Cells have a cycle of life and normally divide to generate new cells. Due to mutation or other biological factors cells can divide uncontrollably leading to uncontrollable growth. This will cause formation of a tumour which can be either benign or malignant. Benign tumours are not cancerous whereas malignant tumours are. To eradicate these tumours, several approaches can be used which include surgery, chemotherapy and the use of radiation.

1.3 Radiotherapy

Radiotherapy is one of the major clinical modalities used for cancer treatment radiation. This field emerged following the discovery of x-rays in 1895 and radioactivity in1896 [2]. Evolution of radiotherapy over the past century led to the development of sophisticated treatment techniques such as Intensity Modulated Radiotherapy (IMRT), Stereotactic Radiotherapy (SRS) and Microbeam Radiation Therapy (MRT) have been developed to enable highly localized dose delivery to the tumour [3-5]. Recently nanotechnology has become a field of interest to act as local dose enhancer since existing techniques cannot further deliver dose to

increase local tumour control since external beam radiation also involves irradiation of surrounding healthy tissue. Particle therapy is an option but is very expensive e.g. good tumour coverage by proton therapy. The ionizing radiation used in radiotherapy controls the abnormal growing cells by targeting the DNA which is the "heart" of the cell. When the DNA is damaged, the cell's ability to reproduce is altered [6,7]. Radiation may be delivered by applying external beams and internal sources.

In external beam radiotherapy, the source of radiation is outside of the patient and the beams are delivered over a distance and directed to the treatment target volume. The targeted region of the body is modelled and during treatment planning radiation beams are directed to this volume whilst adjacent organs are spared to avoid radiation damages to healthy tissue.

Brachytherapy uses sealed sources of radiation. These sources are placed inside the body or in direct contact with the tumour volume. These sources can be temporarily or permanently placed in a patient. The radioactive sources used are in different shapes and sizes and special loading procedures are followed to ensure radiation safety.

1.4. Nanoparticles

In the past two decades there has been an intensive research effort in nanotechnology to develop new approaches in cancer treatment, screening and diagnosis [8]. Nanotechnology is a field that concentrates on the use of different materials that are in the nanometer scale range. NPs used in cancer treatment focuses on carbon structures with high-Z metals attached to them. High-Z materials are known for their larger mass energy absorption coefficient due to their increased probability of photoelectric interactions that lies mostly in the kilovolt range below 500keV. The photoelectric effect varies approximately as $(Z/E)^{3}$, hence an increased deposit of energy (E) at the target volume for lower values of E [9]. In cancer therapy, nanotechnology research is an interdisciplinary field that incorporates chemistry, biology, engineering, medicine and physics.

Cancer cells have properties that are different from healthy tissues and can be exploited by NPs to be attached to cancer cells. NPs effectiveness in cancer treatment, has been

demonstrated in *in vitro* and *in vivo* studies [10]. Experimental and computational methods that include Monte Carlo (MC) simulations were also investigated [11-13].

1.5. Monte Carlo Simulation of Radiation Transport

Radiation transport modelling is a complex process. In radiotherapy, it is important to understand the transport of radiation as it traverses the patient. The differences between the actual and calculated dose distributions in patients may be clinically significant in many cases. Some of available analytical dose computational models for planning of radiation treatment are limited in their accuracy. This is prevalent at tissue interfaces and low Z materials such as lung. High accuracy is now practically available using MC simulations of radiation transport [14].

MC is a problem solving technique used to approximate the probability of certain outcomes by running multiple trial runs, histories, using random variables. This technique has found useful application in radiotherapy since radiation transport is complex to model with the objective to determine the fate of each particle as it moves through a medium. Energy deposition is also easy to model using MC simulation of radiation transport.

In this study the EGSnrc based BEAMnrc and DOSXYZnrc MC codes where used. BEAMnrc was used to model the treatment head of an Elekta Precise linac using various component modules (CM). These are designed to model specific components of a linac that are exposed to the x-ray beam and to track the beam as it passes through these components and finally irradiates the patient. The DOSXYZnrc code is used to provide a 3D dose distribution inside a patient [15-17].

1.6 Study Aims

The aim of the study is to simulate various Bremsstrahlung targets using the EGSnrc based BEAMnrc MC Code. Photon spectral changes for different targets will be used to evaluate dose enhancement in NPs.

Bremsstrahlung targets of different thicknesses and material will be simulated to obtain altered x-ray spectral distributions.

The altered spectral distributions obtained will be used as photon sources in MC simulations in an Anthropomorphic Rando phantom with target volumes seeded with and without NPs to determine dose enhancement factors.

References

1. Garnica-Garza HM, 2012. “Micro dosimetry of x-ray irradiated gold nano-particles,” Radiat. Prot. Dosim.648.

2. Mould RF, 1995. The discovery of X-rays and radioactivity. In: The invisible light: 100 years of medical radiology: eds Thomas AMK, Isherwood I and Wells PNT. 1st Edition, Wiley-Blackwell; 1-6.

3. Ghasemi M, Shamsaei M, Ghannadi M, Raisali G, 2009. Dosimetric studies of micro pencil X-ray beam interacting with labeled tissues by Au and Gd agents using Geant4. Radiat Prot Dosim; 133:97–104.

4. Phillips MH, Stelzer KJ, Griffin TW *et al.,* 1994. Radiosurgery: a review and comparison of methods. J Clin Oncol; 12:1085–1099.

5. Webb S, 2001. Intensity-modulated radiation therapy. Institute of Physics Publishing, Bristol.

6. Hainfeld JF, Slatkin DN, Smilowitz HM, 2004. The use of gold nanoparticles to enhance radiotherapy in mice. Phys Med Biol; 49:309–315.

7. Hainfeld JF, Dilmanian FA, Zhong Z *et al.*, 2010. Gold nanoparticles enhance the radiation therapy of a murine squamous cell carcinoma. Phys Med Biol; 55: 3045–3059.

8. Grodzinski P, Silver M, Molnar LK, 2006. Nanotechnology for cancer diagnostics: promises and challenges. Expert Rev Mol Diagn; 6: 307–318.

9. Hainfeld JF, Slatkin DN, Smilowitz HM, 2004. The use of gold nanoparticles to enhance radiotherapy in mice. Phys Med Biol; 49:309–315.

10. Chithrani DB, Jelveh S, Jalali F, *et al.,* 2010. Gold nanoparticles as radiation sensitizers in cancer therapy.Radiat Res; 173:719-28.

11. Agosteo S, Birattari C, Foglio Para A *et al.,* 2001. FLUKA simulations and measurements for a dump for a 250 GeV/c hadron beam, Math. Comput. Simul; 55: 3–14.

12. Nilsson HE, Dubaric E, Hjelm M, Englund U, 2003. Monte Carlo simulation of the transient response of single photon absorption in X-ray pixel detectors, Math. Comput. Simul; 62:471–478.

13. Lechtman E, Chattopadhyay N, Cai Z, *et al.*, 2011. Implications on clinical scenario of gold nanoparticle radiosensitization in regards to photon energy, nanoparticle size, concentration and location. Phys Med Biol; 56:4631-47.

14. Krieger T, Sauer OA, 2005. Monte Carlo-versus pencil-beam-/collapsed-cone-dose calculation in a heterogeneous multi-layer phantom. Phys Med Biol; 50(5):859-868.

15. Sheikh-Bagheri D, Rogers DW, Ross CK, Seuntjens JP, 2000. Comparison of measured and Monte Carlo calculated dose distributions from the NRC LINAC. Med Phys; 27(10):2256-2266.

16. Mora GM, Maio A, Rogers DW, 1999. Monte Carlo simulation of a typical ^{60}Co therapy source. Med Phys; 26(11):2494-2502.

17. Walters BR, Kawrakow I, Rogers DW, 2005. DOSXYZnrc Users Manual. NRC Report PIRS 794 (rev B)

Chapter 2: RADIATION PHYSICS

2.1 Introduction

Understanding the mechanism through which incident radiation interacts with the targeted material is the key to successful radiation therapy. It is important to know how radiation such as the x-ray beam, is produced as well as its quality and characteristics. This will provide relevant information that will explain the dose distribution at the tumour's site as well as clarifying the localized tumour dose enhancement due to the presence of NPs.

In radiotherapy, x-rays is the major form of radiation used to treat cancerous cells among other types such as electrons, protons and gamma rays. Radiation is classified into two main categories, ionizing and non-ionizing radiation whereas ionizing radiation is again classified into two categories, directly ionizing (protons, electrons, alpha particles etc.) and indirectly ionizing (x-rays and gamma rays). A number of factors are considered such as treatment technique, location of the tumour, type of cancer and the energy of the beam.

Low energies are used mostly for skin surface cancer whilst high energies are used for radiation of deep seated tumours. The x-rays for radiotherapy purpose are generated by a linear accelerator (linac) and are in the form of photons, which travel through space as waves and have energy (E) proportional to their frequency (f):

$$E = hf \tag{2-1}$$

where h is the Planck's constant.

2.2 Production of X-rays

X-rays involved in therapy for the purpose of treatment of diseases is usually 'bremsstrahlung' x-rays. In a conventional linear accelerator, an electron will be accelerated in vacuum and aimed at a high-Z target such as tungsten to produce Bremsstrahlung x-rays.

2.2.1 Bremsstrahlung

Bremsstrahlung is electromagnetic radiation produced when a charged particle, such as an electron, is accelerated in the Coulomb field of a nucleus, as a result, radiative interaction occurs between a high speed electron and the field of an atomic nucleus that will produce 'Bremsstrahlung' also termed braking radiation [1]. Therefore Bremsstrahlung x-rays are formed from electron-nucleus coulomb field interactions illustrated in figure 2.1 below:

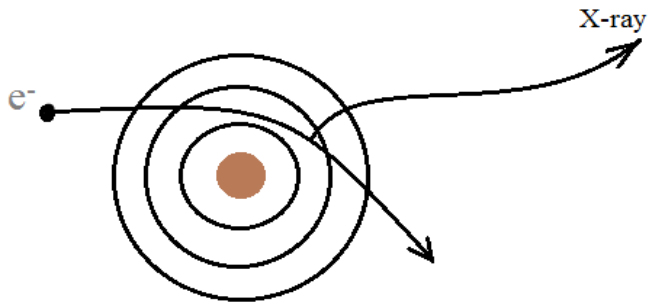

Figure 2.1: Bremsstrahlung x-ray mechanism.

The Bremsstrahlung process occurs when an electron of charge e^- and initial kinetic energy KE_o is decelerated during an encounter with a heavy nucleus of charge $+Z_e$, the electron interacts with the charged nucleus via the Coulomb field, transferring momentum to the nucleus. Hence electron is deflected producing a photon of energy E. The energy of the photon is the difference between the electrons' initial, KE_o and final kinetic energy KE_f.

$$E = KE_o - KE_f \qquad (2\text{-}2)$$

According to classical physics, since every change of direction involves an acceleration, it is probable that the deflected electron can have essentially an infinite number of kinetic

energies between 0 and E_o. Therefore the emitted x-rays photons are produced over an energy spectrum with the maximum beam energy dependent on the peak beam voltage, which implies that the Bremsstrahlung spectrum should be continuous. For the purpose of teletherapy, megavolt Bremsstrahlung x-rays are normally generated using commercially available linear accelerators (linac). In conventional x-ray tubes or linear accelerators, an electron will be accelerated in vacuum and aimed at a high Z target such as tungsten to produce Bremsstrahlung x-rays.

2.2.2 Characteristic X-ray Production

Unlike Bremsstrahlung production, characteristic x-rays are produced when there is interaction between electron and a targeted material. In this interaction, the electron will interact with the atom in the target material by ejecting an orbital electron and results into a transition in the orbital electron such as K, L and M. This transition from high to lower energy level will result in emission of characteristic x-rays. The characteristic radiations are emitted at discrete energies [1].

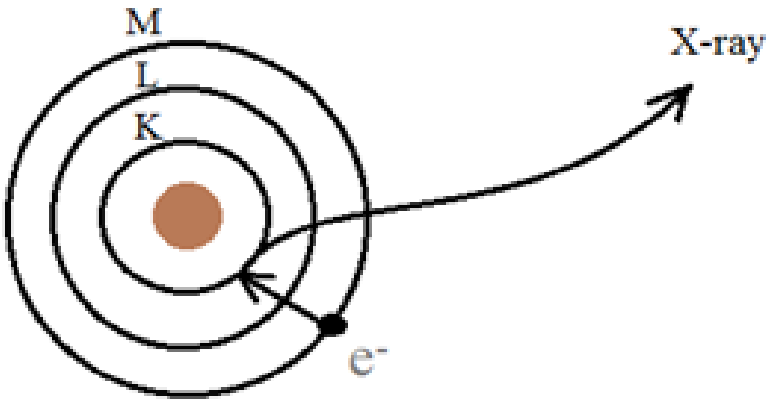

Figure 2.2: Characteristic x-ray mechanism whereby and an x-ray is formed due to M-K orbital transition.

2.3 The Medical Linear Accelerator

The medical linear accelerator is a machine that uses microwave technology to accelerate electrons in a part of the accelerator called the wave guide. Wave guide allows electrons to collide with a heavy metal target such as tungsten. As a result of these collisions, high energy x-rays (photons) are produced in the target. These high energy x-ray beams are shaped using different techniques as they exit the machine to conform to the shape of the patient's tumour. The beam is shaped either by high density material jaws in the head of the machine or by a multi leaf collimator that is incorporated into the head of the machine.

A linac consists of a number of components that begins with a power supply which provides direct current (DC) power to the modulator and microwave source as illustrated in figure 2.3 below. The modulator has a pulse forming network which stores electrical energy to provide flat topped DC pulses to the thyratron, then thyratron uses these pulses as a high-tech switch to deliver the pulses to the electron gun and simultaneously to the magnetron/klystron.

The electron gun produces a stream of electrons through thermionic emission that enter the proximal part of the wave guide with energy of about 50keV. Magnetron or klystron provides pulsed microwaves which are introduced into the wave guide by a hollow rectangular copper piping system.

The wave guide is a copper tube with the interior divided by copper discs or diaphragms where ejected electrons interact with the tuned microwave and so are accelerated and finally exit the thin ceramic window at the end of the wave guide in the form of a 3 mm diameter pencil beam.

If the waveguide is long, bending magnets are introduced to bend the electron beam that exits from the wave guide towards the tungsten target for the purpose of producing Bremsstrahlung x-rays in the forward direction.

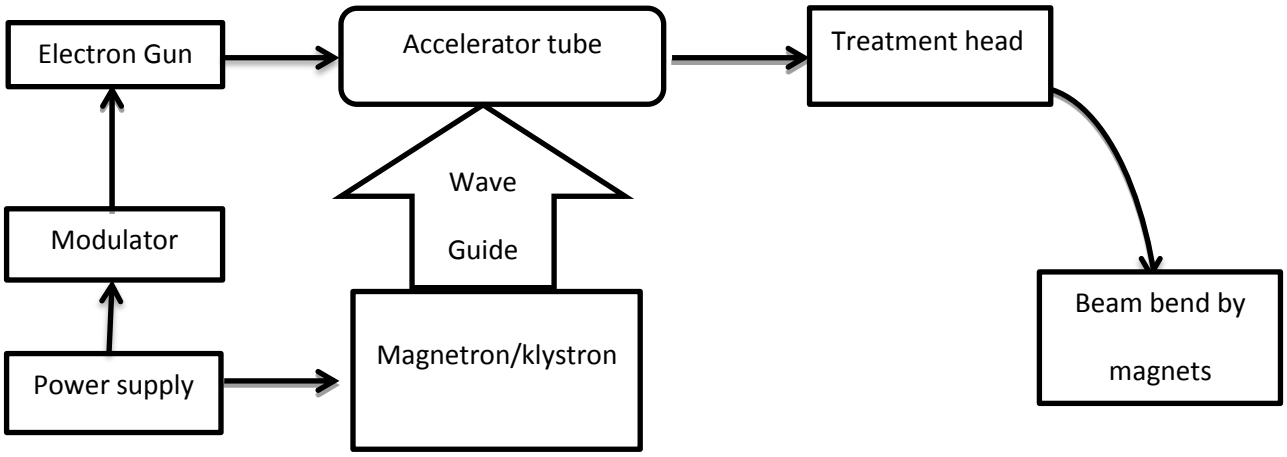

Figure 2.3: Medical Linear accelerator head components. (Adapted from Khan F, 2010. The Physics of Radiation Therapy Lippincott. Williams & Wilkin.

2.4 Photon-matter interaction

Photons interact indirectly in several modes with matter and ionization occurs after the photon has deposited its energy. Therefore in order to understand and predict the effects of adding NPs to a tumour for the purpose of dose enhancement, it is first necessary to review the mechanisms by which ionizing radiation interacts with matter that results in energy deposition to tissue.

Photon beams with energy levels relevant to therapeutic applications can interact with human tissue in one of three main ways, although other modes of interaction are possible. The three major modes photons interact and lose their energy are:

- Photo-Electric Effect
- Compton Scattering
- Pair Production

2.4.1 Photoelectric Effect

Photoelectric effect is an interaction between a photon and a tightly bound electron whose binding energy (E_b) is equal to or less than the energy of the photon .The photon is absorbed by the electron hence electron is ejected due to the absorbed energy considering that the photon energy is higher or equal to the E_b. The ejected electrons will further deposit their energy to the nearby surroundings and they will be liberated with energy determined by:

$$E_e = h\nu - E_b \quad (2\text{-}3)$$

where $h\nu$ is the energy of incident photon and E_b is the electron binding energy.

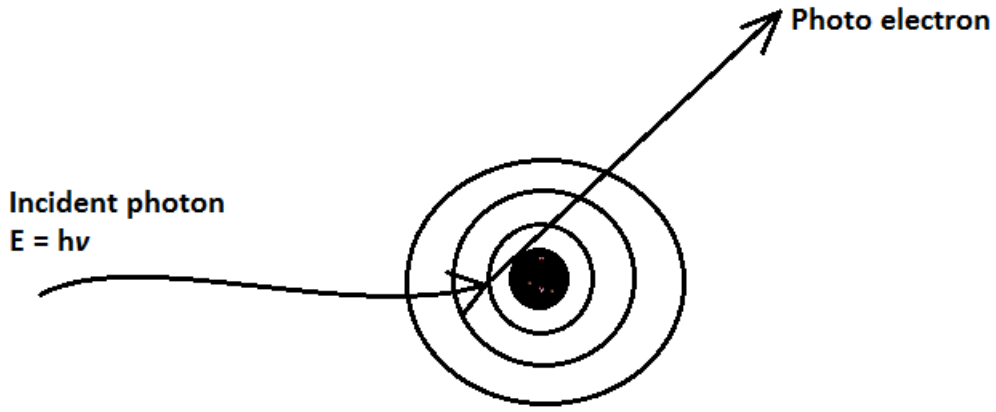

Figure 2.4: Diagram to illustrate photoelectric effect mechanism.

An incoming x-ray photon beam interacts with an orbital electron of a target atom. The targeted electron is excited then ejected and an outer shell electron drops down to fill the vacancy. This process is accompanied by the emission of soft x-rays that are deposited in the immediate region of the interaction. Secondary emission occurs when the excited electrons returns to their ground state by emitting x-rays and Auger electrons. Therefore ionization occurs due to the initially ejected electron as well as the subsequent Auger electrons.

Photoelectric effect occurrence depends on the incident photon energy and the atomic number of the target material. The interaction probability of photoelectric absorption (τ) is approximately determined by:

$$\tau = \frac{Z^n}{(h\nu)^3} \qquad (2\text{-}4)$$

where Z is the atomic number of the absorbing material and hν is the incident photon energy.

Therefore, low energy photon beams targeting high-Z materials produce significant localized dose due to the photoelectric effect. By comparing high-Z material such as gold (Z = 79) and normal tissue (Z = 7.5), the photoelectric effect may have a profound impact on the localized effects of applied radiation.

2.4.2 Compton Scattering

Compton scattering (CS) occurs when a photon interacts with a loosely bound outer-shell electron. The electron will absorb part of the incident photon energy hence scattered photon of lower energy and electron are generated.

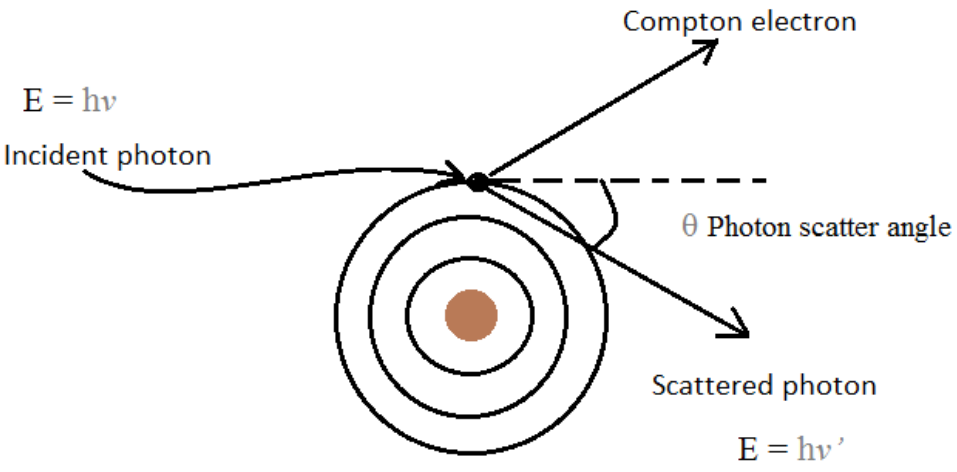

Figure 2.5: Diagram to illustrate compton scattering mechanism

Contrary to the photoelectric effect in which all the photon energy is completely absorbed by the target electron, CS involves the scattering of both the target electron and incident photon. The scattered electron may cause localized ionization while the scattered photon can possibly undergo further interactions in the target material depending on the amount of energy it carries. The interaction probability of CS, σ is proportional to the ratio of the Z of a material to its mass number.

The energy of the scattered photon hν' is given by:

$$h\nu' = h\nu \frac{1}{1+\alpha(1-cos\theta)} \tag{2-5}$$

The energy of the scattered electron E_c is given by:

$$E_c = h\nu \frac{\alpha(1-cos\theta)}{1+\alpha(1-cos\theta)} \tag{2-6}$$

and α is given by

$$\alpha = \frac{h\nu}{m_0 c^2} \tag{2-7}$$

where $m_0 c^2$ is the rest energy of an electron (0.511 MeV) and $h\nu$ is the energy of the incident photon.

The Compton Scattering (CS) interactions dominate in the photon energy range most prevalent in radiation therapy applications. X-ray beams basically used in radiotherapy applications have an energy range of 1-20 MeV, that corresponds to CS cross sections that dominate calculations of total absorption cross sections in that energy range.

2.4.3 Pair Production

For a pair production to occur, the photon energy must exceed 1.02 MeV corresponding to the rest mass of two electrons. The photon will completely disappear as it approaches the nucleus of an atom. The energy absorbed is then expressed by the emission of an electron-positron pair

as illustrated in figure 2.6 below. The remaining energy will be distributed between the two particles as kinetic energy.

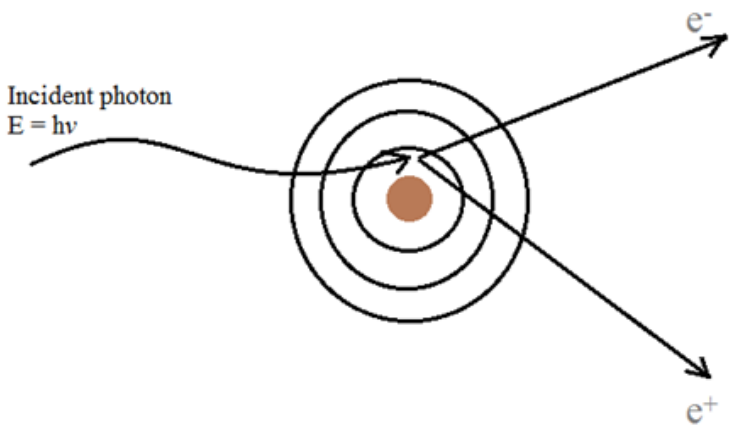

Figure 2.6: Diagram to illustrate pair production mechanism.

This electron and positron pair particles ejected as a result of this collision will cause ionization in the surrounding tissue. Since a positron is an antimatter particle, it cannot exist freely and collision with a free electron causes annihilation and two photons are produced that scatter in opposite directions. The kinetic energy of the electron (E_{e^-}) and the positron (E_{e^+}) generated will be equal to the difference of the energy of incident photon and the total rest mass of the electron and the positron (1.022MeV):

$$E_{e^+} + E_{e^-} = \mathrm{h}\nu - 2m_e c^2 \qquad (2\text{-}8)$$

The interaction probability of pair production (κ) increases with atomic number of material. Due to the creation of the electron-positron pair, this process is not possible for an incident photon with lower energy levels. The energy of the electron-positron pair generated depends on the energy of the incident photon as its energy is imparted to the ion pair produced. These photons may then undergo further interactions in the target material based on their energy levels that can lead to energy deposit.

2.4.4 Auger Electron Generation

Auger electrons are of interest to high-Z NPs dose enhancement research in radiotherapy as well as understanding further the mechanism of photoelectric effect. After a tightly bound electron in atom absorbs a photon via the photoelectric effect or Compton interaction, the electron is ejected and the vacancy within the high-binding energy orbital is filled by an electron from one of the lower-binding energy orbitals. As a result a photon is emitted by the electron as it changes energy potentials known as the characteristic x-ray. The characteristic x-ray may be absorbed by other electrons in the same atom that will eject another electron which will be known as an Auger electron. Auger electrons can be clinically significant for NPs localised dose deposit in radiotherapy, since they have very low kinetic energy that will make them deposit all of their energy basically at the Auger formation site. For this reason, Auger electron becomes a major factor in high-Z NPs dose enhancement research.

2.5 Relative Predominance of the Three Major Modes of Photon Matter Interactions

The chance for a photon to undergo any one of the three modes of interaction phenomena with matter depends on the energy of the photon E and on the atomic number Z of particular material. As illustrated in figure 2.7 below, generally the photoelectric effect which is major contributor to dose deposit in tumour predominates at low photon energies followed by the Compton Effect at intermediate energies and pair production at high photon energies [2].

The two curves in figure 2.7 below delineate the regions of predominance of photoelectric effects, Compton Effect and pair production at various photon beam energies (hv) and atomic numbers (Z) of the respective material of interaction.

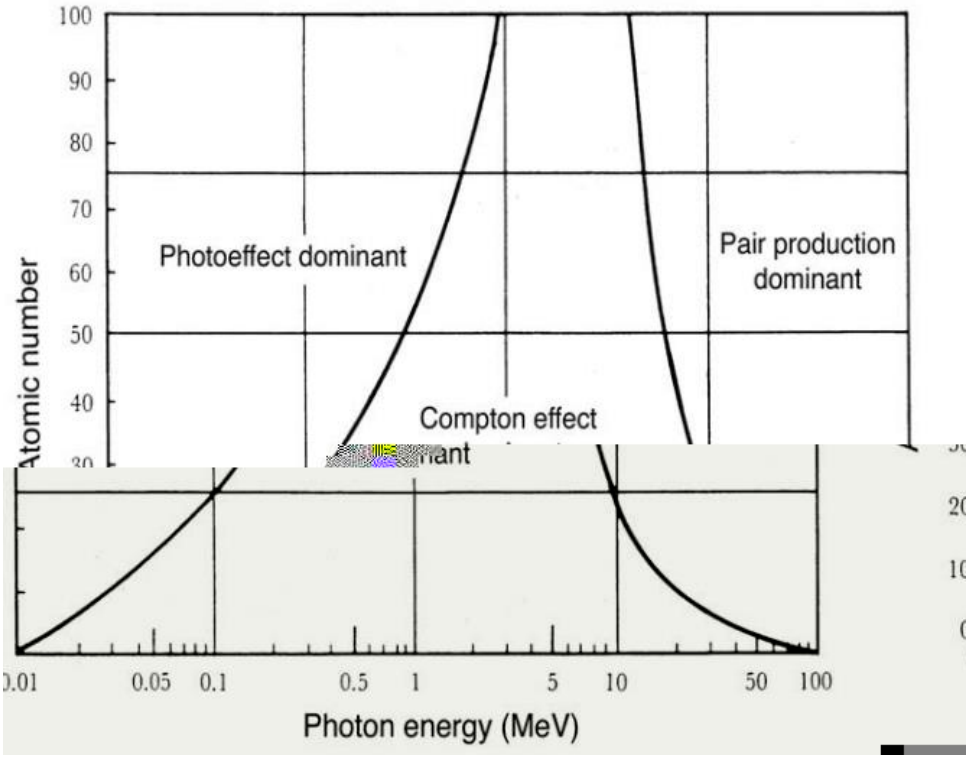

Figure 2.7: Regions of relative predominance of the three major photon–matter interactions, photoelectric effect, compton effect and pair production. (Adapted from Podgorsak EB, 2005. Radiation Oncology Physics P37: A handbook for teachers and students)

The photoelectric effect is predominant at low energies well below 1 MeV and Compton effect at intermediate energies whilst pair production at high energies of at least 1.02 MeV. For example, a 100 keV photon will interact with Au (Z = 74) predominantly through the photoelectric effect whilst higher energies such as 10 MeV photon beams will interact with Au predominantly through pair production and with tissue (Z=7.5) predominantly through the Compton effect.

2.6 Dosimetry Terminology

The calculation and assessment of the radiation dose received by the human body is a major aspect in the use of ionizing radiation to evaluate its impact. The calculation and assessment can be achieved through dosimetry. Dosimetry is the determination of the delivery of radiation energy to matter. Radiation dosimetry deals with methods for a quantitative determination

of energy deposited in a given medium by directly or indirectly ionizing radiations and to achieve this, various dosimetric quantities were devised to provide a physical measure to correlate with actual or potential effects.

Radiative energy transfer and impartation in matter depends on various specifications of the radiation field at the point of interest as well as on the interactions between radiation and matter. The importance of dosimetry in the use of radiation to treat diseases was recognized quite early as illustrated by the foundation of the International Commission on Radiation Units and Measurements (ICRU) in 1925. Its purpose is the development of internationally acceptable recommendations in radiation dosimetry which was published in the form of ICRU Reports of which is Report 60 [3]. The most commonly used dosimetric quantities and their units which describe the radiation beam are defined below.

2.6.1 Exposure

Exposure was one of the first quantities used for the measurements of radiation which was based on the ionization of x-rays and gamma rays in air. This was the start of the use of the unit röntgen which was defined in 1937 as a unit of quantity of dose [4]. Later in 1962 the ICRU separated exposure and dose as two different quantities, and röntgen, with the symbol R, became the unit of the quantity exposure [5]. Nowadays exposure as a quantity has lost its previous importance. The exposure (X) is the quotient of dQ by dm where dQ is the absolute value of the total charge of the ions of one sign produced in air when all the electrons liberated by photons in air of mass dm are completely stopped in air:

$$X=\frac{dQ}{dm} \tag{2-9}$$

The SI unit of exposure is C kg^{-1}.

2.6.2 Absorbed Dose

Absorbed dose (D) is a non-stochastic quantity applicable to both indirectly and directly ionizing radiations and is defined as the mean energy E imparted by ionizing radiation to matter of mass m in a finite volume V: [3]

$$D = \frac{dE}{dm} \quad (2\text{-}10)$$

The energy imparted E is the difference of the sum of all the energy leaving the volume of interest from all the energy entering the volume, taking into account any mass–energy conversion within the volume.

The SI-unit of absorbed dose is joule per kilogram (J kg $^{-1}$) and the special name for the absorbed dose unit is gray (Gy).

2.6.3. KERMA

KERMA (K) is a non-stochastic quantity applicable to indirectly ionizing radiations such as photons. The word KERMA is an acronym for kinetic energy released per unit mass. KERMA quantifies the average amount of energy E_{tr} transferred from indirectly ionizing radiation to directly ionizing radiation per unit mass m of matter, such as from photons to electrons. Therefore K is the quotient of dE_{tr} by dm, where dE_{tr} is the sum of initial kinetic energies of all charged particles including the kinetic energy of Auger electrons in a mass dm of material: [3]

$$K = \frac{\mathrm{dEt}}{\mathrm{dm}} \quad (2\text{-}11)$$

The SI-unit for KERMA is J kg $^{-1}$ and its special name is gray (Gy). For direct ionizing radiation a similar quantity called CEMA is defined [3,6].

2.6.4. CEMA

CEMA(C) is a non-stochastic quantity applicable to directly ionizing radiations such as electrons. CEMA is the acronym for converted energy per unit mass , whereby C is the quotient of dE by dm, where dE is the energy lost by charged particles, excluding secondary electrons, in collisions in a mass dm of a material:

$$C = \frac{\mathrm{dE}}{dm} \quad (2\text{-}12)$$

The SI-unit for kerma is J kg $^{-1}$ and its special name is gray (Gy).

2.6.5. Particle Fluence and Energy Fluence

Particle fluence and energy fluence are quantities usually used to describe mono-energetic photon beams and may also be used in describing charged particle beams.

- The particle fluence F is the quotient dN by dA, where dN is the number of particles incident on a sphere of cross-sectional area dA:

$$F = \frac{dN}{dA} \tag{2-13}$$

The unit of particle fluence is m^{-2}.

- The energy fluence Ψ is the quotient of dE by dA, where dE is the radiant energy incident on a sphere of cross-sectional area dA:

$$\Psi = \frac{dE}{dA} \tag{2-14}$$

The unit of energy fluence is Jm^{-2}.

2.6.6 Stopping Power

Stopping powers namely, linear stopping power and mass stopping power, although they are used in radiation dosimetry they are rarely measured and are calculated from theory.

- The linear stopping power is defined as the expectation value of the rate of energy loss per unit path length of the charged particle. The unit for linear stopping power is MeV/cm [7].
- The mass stopping power is defined as the linear stopping power divided by the density of the absorbing medium. The unit for mass stopping power is $MeV \cdot cm^2/g$.

2.6.7 Charged Particle Equilibrium

The concept of charged particle equilibrium (CPE) is useful in radiological physics for photon radiation dosimetry as a means to relate certain basic quantities. In general CPE exists with respect to volume (V) if for each charged particle of a given type, energy and direction leaving V, there is an identical particle entering V [8].

One important aspect of the CPE conditions is to establish the equivalence of the absorbed dose (D) and the kerma (K) which are described by the equations 2-10 and 2-11 respectively. In general, due to finite range of secondary electrons released through photon interactions, the transfer of energy (kerma) from the photon beam to charged particles at a particular location does not lead to the absorption of energy by the medium (absorbed dose) at the same location. Since radiative photons mostly escape from the volume of interest, it is possible to establish a relation between both quantities when it electronic equilibrium exists at the point of calculation. Therefor one relates absorbed dose usually to collision kerma (K_{col}). The ratio of dose and collision kerma is usually given as:

$$\beta = \frac{D}{K_{col}} \tag{2-15}$$

It is assumed that, $\beta = 1$ if radiative photons escape the volume of interest.

In realistic situations as illustrated in figure 2.8 below such as in the build-up region of a beam where the dose increases before decreasing exponentially and near the edges of a finite beam at distances between the beam edge and the point under consideration larger than the maximum secondary electron range (penumbra region), CPE is not usually achieved.

Figure 2.8 demonstrates the relation between absorbed dose (D) and collision kerma (K_{col}) for a megavoltage photon beam as function of depth in a phantom of a given medium under build-up conditions; under conditions of charged particle equilibrium (CPE) in part (a) and under conditions of transient charged particle equilibrium (TCPE) in part (b).

As illustrated by part (a) under CPE conditions, at or near the entrance surface of the medium the absorbed dose is smaller than the kerma. The collision kerma is maximal at the surface of the irradiated material because photon fluence is greatest at the surface. The absorbed dose increases as a function of depth as the photon beam penetrates the medium until the depth of maximum dose (z_{max}) is attained. Beyond z_{max} if there were no photon attenuation or scattering in the medium, but yet production of electrons, a dose build-up region occurs where $\beta < 1$ followed by a region of complete CPE where $\beta = 1$. The dose build up region results from the relatively long range of energetic secondary charged particles that first are released in the patient by photon interactions and then deposit their kinetic energy in the medium.

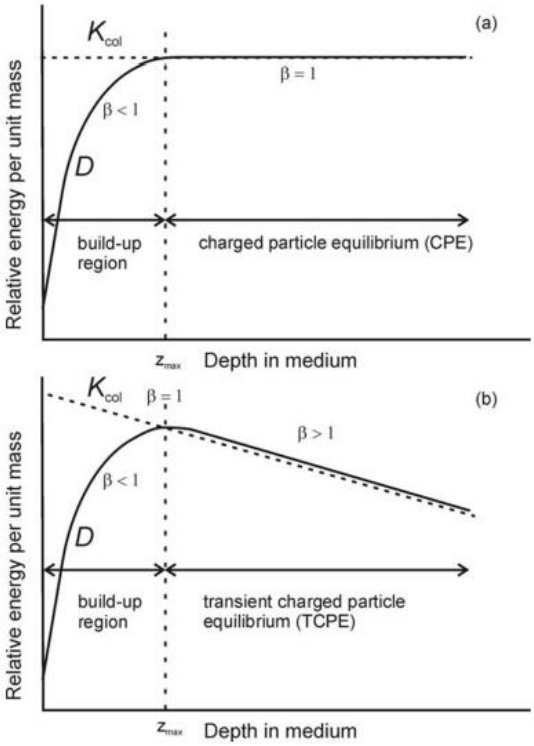

Figure 2.8: Relation between absorbed dose and collision kerma as a function of depth in a medium irradiated by a high energy photon beam. (a) Charged particle equilibrium. (b) Transient charged particle equilibrium. (Adapted from Podgorsak EB, 2005. Radiation Oncology Physics. P59: A handbook for teachers and students.)

Under TCPE as shown by part (b) in a more realistic situation, however, to satisfy the condition of uniform charged particle fluence along the depth is impossible due to photon divergence and attenuation. Therefore, beyond z_{max} both the dose and collision kerma decrease because of the photon attenuation in the medium, resulting in a transient rather than an actual CPE, but a constant relation between both quantities is maintained.

2.7 Monte Carlo Application to Photon Radiation Dosimetry

All the above dosimetric quantities can be used for dose calculation in simple geometry and for reference dosimetry where cavity theory is applied to calculate the dose in, say, water under CPE conditions. The patient geometries are so complex that the MC technique would suffice

here since all sophisticated dose calculation algorithms would break down at tissue interfaces between tissues and bone and tissue and lung. Radical radiotherapy requires an accuracy of 5% in the delivery of absorbed dose and the demand is extremely challenging when heterogeneous tissue are involved [9-11].

Some commonly used dose calculation algorithms such as equivalent tissue-air ratio (ETAR) and Batho have limitations in their accuracy. In ETAR method the changes in lateral transport of electrons are not modelled [12]. The Batho method has high correction accuracy in homogeneous tissue, but has lower correction accuracy in cavum and the interface between different tissues thus result in an overestimation or underestimation of dose [13]. Therefore MC method is the most appropriate dose calculation method and is considered to be the most accurate algorithm, thus it has always been used to generate benchmarking dose distribution with which to compare the results of other dose calculation methods [14].

References

1. Khan F, 2010. The Physics of Radiation Therapy. Lippincott Williams &Wilkin.

2. Podgorsak EB, 2005. Radiation Oncology Physics: A handbook for teachers and students

3. ICRU. (International Commission on Radiation Units and Measurements),1998. Fundamental Quantities and Units for Ionizing Radiation, ICRU-Report 60, Bethesda, MD.

4. Greening JR, 1986. Fundamentals of Radiation Dosimetry, 2 rd ed. Bristol, IoP.

5. ICRU. (International Commission on Radiation Units and Measurements), 1962.Radiation Quantities and Units, ICRU-Report 10a, Government Printing Office, Washington D.C.

6. Kellerer AM, Hahn K and Rossi HH, 1992. Radiat. Res; 130:15-25 .

7. ICRU (International Commission on Radiation Units and Measurements), 1984. Stopping powers for Electrons and Positrons, ICRU-Report 37, Bethesda, MD.

8. Attix FH, 1983. Energy imparted, energy transferred and net energy transferred. Phys. Med. Biol; 28:1385–1390.

9. Brahme A, 1984. Dosimetric precision requirements in radiation therapy. Acta Radiol Oncol; 23(5):379-391.

10. International Commission on Radiation Units and Measurements (ICRU), 1976. Determination of absorbed dose in a patient irradiated by beams of X or gamma rays in radiotherapy procedures. ICRU Report 24. Washington(DC):ICRU.67p.

11. Metcalfe PE, Wong TP, Hoban PW, 1993. Radiotherapy X-ray beam inhomogeneity corrections: the problem of lateral electronic disequilibrium in lung. Australas Phys Eng Sci Med; 16(4):155-167

12. Sontag MR, Cunningham JR, 1978. The equivalent tissue-air ratio method for making absorbed dose calculations in a heterogeneous medium. Radiology; 129:787–794.

13. Webb S, Fox RA, 1980. Verification by Monte Carlo methods of a power law tissue-air ratio algorithm for inhomogeneity corrections in photon beam dose calculations. Phys Med Biol; 25:225–240.

14. Metcalfe P, Kron T, Hoban P, 2007. The physics of radiotherapy x-rays and electrons. Madison, WI: Medical Physics Publishing.

Chapter 3 MONTE CARLO SIMULATIONS

3.1 Introduction

Monte Carlo (MC) is a numerical method for simulating the behaviour of various physical and mathematical systems to find solutions on stochastic events. It is a computational tool that samples from known probability distributions to determine the average behaviour of a system. The name MC originates from the gambling aspect that relies on probabilities for certain events to occur, and was coined by von Newmann and Ulam in 1947 which refers to a casino in Monaco [1, 2]. The bases of the Monte Carlo technique is simulations achieved by building a model that represent the real system of interest.

Bielajew *et al.* (2001) demonstrated that MC provides a solution to a problem that model objects interacting with other objects or with their environment. It is based on simple relationships whereby interaction probabilities must be well defined by probability distribution functions (PDFs). As the number of individual events or histories is increased, the quality of the reported average behaviour of the system improves, meaning that the statistical uncertainty error decreases. With MC, almost any complex system can in principle be modelled, hence this has resulted in its application to simulate the production, transport and the ultimate fate of radiation as it transverse through a medium of any complexity.

MC technique has become one of the most popular tools to investigate radiation dosimetry in different areas of medicine following the development and subsequent implementation of powerful computing systems for clinical use [3]. It can be applied in almost all the aspects of medical physics including radiation protection, diagnostic radiology, radiotherapy and nuclear medicine. The goal of this chapter is to introduce the basic theoretical framework behind the MC technique and to provide demonstrations on the use of this powerful technique to evaluate NP dose enhancement using various Bremsstrahlung x-ray targets in radiation therapy.

A number of MC codes have been developed over the years. The first available MC code for treatment planning, EGS4, was developed as part of the OMEGA project, [4] which started in

the early 90s by the National Research Council of Canada and the University of Wisconsin in Madison. The EGS4 code modelled the transport of photons and electrons. The EGS4 based BEAM system which has been replaced nowadays by EGSnrc and BEAMnrc is used for modelling of radiotherapy sources.

3.2 Selection of Monte Carlo Code

A series of MC software packages were developed. The ETRAN code, developed by Berger and Seltzer can be considered as one of the first MC codes system for electron and photon simulation through extended media [5]. The PENELOPE (Penetration and ENErgy LOss of Positrons and Electrons) code package has a detailed treatment of cross sections for low-energy x-ray and electron transport and a flexible geometry package which allows simulation of accelerator beams [6]. The GEANT4 code is a general purpose code developed for particle physics transport simulations of particle types such as neutrons, protons, and pions.GEANT4 has been used for various applications in radiotherapy physics and is the basis of the GATE simulation toolkit for nuclear medicine applications in PET and SPECT [7,8].

MANTIS is a MC x-ray electron optical imaging simulation code package that describes the coupled transport of x-rays and light produced in a scintillation material. It is based on PENELOPE [9].

Finally, the EGS4 (Electron Gamma Shower) is a software tool from the National Research Council, Canada. It is a MC code that simulates radiation of energy ranging from 1 keV to 10 GeV. The EGSnrc code system preceded the EGS4. EGSnrc software package released by Rogers *et al.* (2001) is an extended and improved version of the EGS4 package originally developed at Stanford Linear Accelerator Centre (SLAC). The EGSnrc software is more user friendly and easy to understand. Its Graphical User Interface allows users to edit the required MORTRAN code without having to master the syntax of the language, to suit different models. This user interface also allows easy modelling of, in particular, radiotherapy linear accelerators. Rogers *et al.* (2003) came up with EGSnrc package that consist of BEAMnrc, DOSXYZnrc, DOSRZnrc, FLURZnrc, CAVRZnrc, SPRRZnrc and other simulation codes that come as a package under

license to the National Research Council (NRC). All MC simulations reported in this study were performed with the EGSnrc–based BEAMnrc and DOSXYZnrc packages.

Of particular interest to this study, the EGSnrc package has been used in evaluating nanoparticles dose enhancement in previous studies [10, 11].

3.3 The EGSnrc Code System

The early versions of the Electron-Gamma-Shower (EGS) system were developed in the 1970s at the Stanford Linear Accelerator Center by Rogers and co-workers [4]. It was followed by EGS4 system which was released in the 1980s, which was subsequently used in Medical Physics applications. EGS4 was used as basis for the BEAM system by Rogers *et al.* (1995). The most recent version of EGS4 developed at the National Research Council of Canada (NRC) is EGSnrc that incorporates many improvements considering the implemented transport physics as demonstrated by Kawrakow (2000).

The EGSnrc system provides subroutines and functions for sampling from various photon and electron interactions. The quantities of interest are available to the user during runtime. These quantities must be processed for calculating and reporting of the final result. A set of readily implemented user codes and programs is available such as SPRRZnrc code, FLURZnrc code, DOSRZnrc code, BEAM code and the DOSXYZnrc code which allows the definition of geometry, set-up of various particle sources and the scoring of quantities sufficient for most problems.

3.3.1 BEAMnrc

BEAMnrc MC code allows for the simulation of radiation therapy treatment units and produces data that can be matched close to realistic clinical beams. It was developed as part of the OMEGA project which was collaboration between the National Research Council of Canada (NRC) and a research group at the University of Wisconsin (USA). BEAMnrc is a general purpose Monte Carlo simulation system for modelling radiotherapy sources and is based on the EGSnrc code system [12].

The BEAMnrc code has been designed to simulate both photon and electron beams from a variety of radiotherapy radiation source units including low energy x-rays and Co–60 units.

BEAMnrc/EGSnrc MC code has been extensively benchmarked against measured dose distributions for a variety of accelerators in previous studies and good agreement was obtained for central-axis percentage depth-dose. The BEAMnrc/EGSnrc MC code is considered as a standard in the field of medical physics for modelling electron and photon transport [13,14]. It consist of a component modules (CM) that allows the modelling of individual components in the linac head such as the target, primary collimator, flattening filter, multi leaf collimator and jaws. Rogers *et al.* described CM as a block with a 'front' and a 'back' surface [13].

BEAMnrc MC simulations generate a Phase Space (PS) file on each scoring plane directly below any CM if so specified by the user. The generated PS file contains all the information relating to the beam at a specified scoring plane such as particle type, energy, position, charge and direction. The PS file can be used as input source in subsequent simulations.

3.3.2 BEAMDP

BEAMDP (Beam data processor) is a computer program that was originally developed for the OMEGA project by Ma and Rogers (1995), to analyze the PS data and to derive spectral and planar fluence distributions for use by beam characterization model. BEAMDP analyze the parameters of the PS file from simulation of clinical beams generated by BEAMnrc [4]. BEAMDP can also be used as a multi-purpose program to derive the data required by multiple-source models for use in MC RT treatment planning. It can also be used to derive energy distribution/fluence plots, angular distributions, scatter plots and also to combine PS files.

3.3.3 DOSXYZnrc

DOSXYZnrc is an EGSnrc-based MC simulation user-code used to calculate the three dimensional (3D) absorbed radiation dose distributions in a rectangular cartesian voxel based phantom. According to Walters *et al. (*2005), DOSXYZnrc simulates particle transport in a rectilinear geometry and scores the energy deposition in the designated volume elements (voxels). The voxel dimensions are variable in all three directions and each voxel can have different materials with varying densities for use with CT data.

DOSXYZnrc can use the PS data file generated by BEAMnrc as input sources as demonstrated by Lin *et al. (*2002) and its output is a file that stores the calculated 3D dose distribution data and the corresponding dose uncertainties. The 3D dose file produced can be analysed to extract PDD and dose profiles. The code allows a wide variety of source configurations and can accurately predict detailed dose distributions inside a phantom through simulation where experimental measurements are difficult or impossible to perform.

3.4 Monte Carlo Particle and Photon Transport Simulation

Photons and particles such as protons and electrons undergo different types of interactions as they move through matter. Understanding these interactions is essential in radiation therapy. Particles tracks as they traverse through media may be interpreted as a Markov- process, where future values of an interaction event are statistically determined by present events which depend only on the event immediately preceding. Thus according to Bielajew (2001) the macroscopic solution of complete Boltzmann transport equation is broken down to single microscopic events even for complex geometries.

The simulation of particle transport generally consists of four steps which are repeated until particles have left the defined simulation geometry or if their energy falls below a specified energy (in the EGSnrc code system these energies are referred to as ECUT (0.521MeV) and PCUT (0.01MeV)) which is the energy where particles are assumed to be stopped and absorbed in the medium.

Charged particles may undergo thousands of interactions per cm in a medium giving rise to complex transport kinematics. Fortunately with improvement in computer technology, computers today are capable of handling such complexity. In most Monte Carlo codes, particle transport is modelled by divide the path of a charged particle into a series of small steps. The transport of these particles is governed by processes such as stopping collision, coulomb scattering and nuclear interactions.

In photon transport the interactions are governed with photon cross sections of the medium. The major photon interactions with matter include the photoelectric effect, Compton

scattering, pair-production, and photonuclear interactions. The cross sections refer to the various kinds of attenuation coefficients which are important in particle transport simulations. The probability of occurrence of an interaction can be expressed in terms of the linear attenuation coefficient μ, which indicates the fraction of incident photons that will interact per unit thickness of the attenuating medium.

3.5 Monte Carlo Technique in Radiotherapy

In radiotherapy, the dose delivered needs to be calculated as accurate as possible to ensure little or no damage to critical tissues and high tumour control probability. Therefore, it is important to have an accurate technique for predicting the dose distribution. Therefore MC technique will be more suitable to predict dose distribution since it is currently the most available computational tool to compute dose distribution in medium [3,12].

Whereas in radiotherapy, the necessity of a very accurate dosimetry of 5% or even higher in certain situations is needed [15]. Therefore MC simulations have proven helpful in modelling linac treatment head in radiotherapy by providing very accurate results on the characteristics of realistic radiotherapy beams [16].

In recent years, owing to the computing power available and new mathematical approaches to accurate dose calculation and optimization , MC methods have been considered as an alternative to analytical methods for treatment planning in cancer radiotherapy to give the most accurate solution [17,18]. MC algorithms form an integral part of the clinical implementation of a dose calculation and verification as experimental verifications. Therefore MC algorithms will benefit from similar experimental verification procedures as conventional systems, and as such should follow the commissioning procedures detailed in the AAPM TG-53 report and other relevant publications [19-21]. In particular, it simulates processes involving random behaviour and to quantify physical parameters that are difficult or even impossible to calculate analytically or to determine by experimental measurements such as the transport of photon and electron by recording the interactions of each particle until it reaches the present minimum energy.

3.6 Variance Reduction Techniques

To increase efficiency (ε) in MC simulations, variance reduction techniques are employed. The efficiency of a MC code takes into account both the CPU simulation time (T) for N histories and the statistical uncertainty (σ). Efficiency (ε) can be defined as:

$$\varepsilon = \frac{1}{\sigma^2 T} \tag{3-1}$$

where σ^2 is the variance of simulation result. The time, T needed to reach the variance is directly proportional to N, while the variance is proportional to 1/N. Thus, the efficiency is not dependent on the number of histories.

The efficiency of a given calculation can be improved by either decreasing σ for a given T or decreasing T for a given N without changing the variance. Calculation time depends on the power of computers and better programming techniques. However variance is lowered using variance reduction techniques. The goal is to reduce sample variance so that the relative error decreases. Variance reduction (biasing) techniques for MC simulations can also reduce the amount of computer time required for obtaining results of sufficient precision. Many of the variance reduction techniques produce and/or destroy particles during the simulation per history to produce outcomes as close as possible to the solution. Variance reduction algorithms can be classified into four major categories.

- Truncation methods whereby some aspects of the simulation that contribute little to the outcomes are truncated to speed up calculations. These are the simplest variance reduction methods that include geometry truncation in which unimportant parts of the geometry are simply not modelled and employing energy cut-offs. In BEAMnrc, an example is the range rejection method that allows the user to terminate the history of an electron when its residual CSDA range is such that it cannot possibly reach some region of interest and deposit its energy there [13].

- Population control methods, such as particle splitting and Russian roulette which controls the quantities of the particles to be sampled based on their levels of importance. Population control methods artificially increase the number of particles in spatial or energy regions that are important or decrease this number in the case it doesn't contribute to the score tally.
- The modified sampling methods, which modifies the sampling distributions to improve the statistics. The modified sampling methods artificially increase the likelihood of certain events, increasing the particle of interest probability to reach the tally region.
- Lastly, the partially deterministic methods which incorporate some deterministic features in the sampling, which may alter the random number sequence. These are the most complicated class of variance reduction methods. They use deterministic-like techniques, such as next event estimators or by controlling the random number sequence to circumvent the normal random walk process.

References

1. Metropolis N, 1987. The beginning of the Monte Carlo method, Los Alamos Science (Special Issue dedicated to Stanislaw Ulam); 125 - 130.

2. Bielajew AF, 2001. Fundamentals of the Monte Carlo method for neutral and charged particle transport (The University of Michigan).

3. Andreo P, 1991. Monte Carlo techniques in medical radiation physics, Phys. Med. Biol; 36:861–920.

4. Rogers DWO, Kawrakow I, Seuntjens JP, Walters BRB and Mainegra-Hing E, 2003. NRC User Codes for EGSnrc, National Research Council of Canada Report PIRS-702, rev B, Ottawa, NRC.

5. Berger MJ and Seltzer SM, 1968. "Electron and Photon Transport Programs.I. Introduction and Notes on Program DTAPAC 4; II. Notes on Program ETRAN-15", Rep. NBS 9836 and 9837, Gaithesburg: NBS.

6. Salvat F ,Fernández-Varea JM and Sempau J, 2006. "PENELOPE, A Code System for Monte Carlo Simulation of Electron and Photon Transport (3rd edition)", OECD-NEA, Issy-les-Moulineaux, France.

7. Zaidi H,1999. "Relevance of accurate Monte Carlo modeling in nuclear medical imaging," Med. Phys. Vol; 26:574-608.

8. Agostinelli S*. et al.*, 2006. "GEANT4-a simulation toolkit", Nucl. Instrum. Methods A.,Vol; 506:250-303.

9. Badano A and Sempa J, 2006. "MANTIS: combined x-ray, electron and optical Monte Carlo simulations of indirect radiation imaging systems" Phys. Med. Biol; Vol 51:1545-1561.

10. Nilsson HE, Dubaric E, Hjelm M, Englund U, 2003. Monte Carlo simulation of the transient response of single photon absorption in X-ray pixel detectors, Math. Comput. Simul; 62:471–478.

11. Lechtman E, Chattopadhyay N, Cai Z, *et al*., 2011. Implications on clinical scenario of gold nanoparticle radiosensitization in regards to photon energy, nanoparticle size, concentration and location. Phys Med Biol; 56:4631-47

12. Kawrakow I, Mainegra-Hing E and Rogers DWO, 2011. The EGSnrc Code System: Monte Carlo Simulation of Electron and Photon Transport, National Research Council of Canada, Report PIRS-701, Ottawa, NRC.

13. Rogers DWO, Walters B and Kawrakow I, 2007. BEAMnrc User's Manual, National Research Council of Canada, Report PIRS-0509 (A) rev K, Ottawa, NRC.

14. Rogers DWO, Faddegon BA, Ding GX, Ma CM, We J and Mackie TR, 1995. BEAM: a Monte Carlo code to simulate radiotherapy treatment units, Med. Phys; 22:503–524.

15. Mijnheer BJ, Battermann JJ, Wambersie A, 1989. Reply to precision and accuracy in radiotherapy, Radiother. Oncol. 14 163–167.

16. Ma C, Faddegon B, Curran B, 2005. Monte Carlo for Radiotherapy I: Source Modelling and Beam Commissioning for Monte Carlo Treatment Planning, AAPM, Continuing Education Course.

17. Verhaegen F and V. Seuntjens V, 2003. Monte Carlo modelling of external radiotherapy photons beams Phys. Med Biol; 48:R107-R164.

18. Reynaert N, van der Marck S and Schaart D, 2006. Monte Carlo Treatment Planning: An Introduction Report 16 of the Netherlands Commission on Radiation Dosimetry (NCS) June 2006 NCS, Delft, The Netherlands ISBN 90-78522-01-1.

19. Fraass B, Doppke K, Hunt M*, et al.*, 1998. American Association of Physicists in Medicine RadiationTherapy Committee Task Group 53: Quality assurance for clinical radio-therapy treatment planning Med. Phys. 25, 1773–1829 1998 .

20. Van Dyk J, R. B. Barnett RB, Cygler JE, and Shragge PC, 1993. Commissioning and quality assurance of treatment planning computers, Int. J. Radiat.Oncol. Biol. Phys. 26, 261–273 .

Chapter 4: NANOPARTICLES IN RADIOTHERAPY

4.1 Introduction

Radiation therapy procedures are ultimately designed to destroy tumour cells while protecting healthy cells. In most of these procedures, conventional beam doses are limited by the sensitivity of adjacent healthy tissue that can receive substantial radiation doses during some high dose treatments. Usually multiple beams from different directions are used to conform the absorbed dose at the tumour site. Owing to this, the use of high-Z nanoparticles (NPs) during radiation therapy which is the new era in cancer treatment and it is currently under intense investigation to find ways that enhance the ratio of dose given to the target cells compared with the healthy cells.

NPs in radiation dose enhancement are defined as structures with a size range of 1–100 nm in at least one dimension and are typically smaller compared to biological molecules such as enzymes, receptors, and antibodies. NPs demonstrate unique capabilities which make them useful in cancer treatment based on intrinsic properties such as shape and size as well as functional properties conferred through surface modifications.

The use of NPs in therapeutic cancer applications is becoming increasingly investigated. These biologically compatible particles can be easily synthesized and manufactured to different sizes that can be useful in radiation dose enhancement. NPs can be a key to successful radiotherapy by optimizing localized tumour dose and ensuring the critical tissues are well protected. Recent studies have shown that tumour dose can possibly be enhanced using metal complexes attached to carbon nanoparticles.

Therefore, the aim of this study was the development of suitable targets for a megavolt X-ray therapy machine to enhance the dose delivered to the tumour by using nanoparticles. The study was done in phantom and simulated patient studies by using the EGSnrc based Monte Carlo codes. This chapter presents a review of the radiation dose enhancement produced by high-Z materials in general and gold nanoparticles (AuNPs) in particular.

4.2 Dose Enhancement by High-Z Materials

The existence of radiation dose enhancement caused by high-Z materials in the target were earlier investigated by Spiers *et al.* (1949) and reported in several publications [1-3]. The high-Z materials that have been studied before include gold and gadolinium. The dose enhancement due to increased photoelectron production caused by interaction between x-rays and high-Z materials, was investigated by many other scientists [4,5]. Dose enhancements due to the scattered electrons only in the vicinity of the tumour volume seeded with high-Z material have been previously reported [5,6]. The effects of the increased number of photoelectrons and scattered electrons on biological materials have also been investigated. Experiments verified that monolayers of cells exposed to kilovoltage x-rays adjacent to high-Z materials showed an increase in the number of cells killed [7-9]. Basically dose enhancement is due to the production of additional particles such as Auger electrons when x-rays interact with high-Z number material as illustrated on figure 4.1 below.

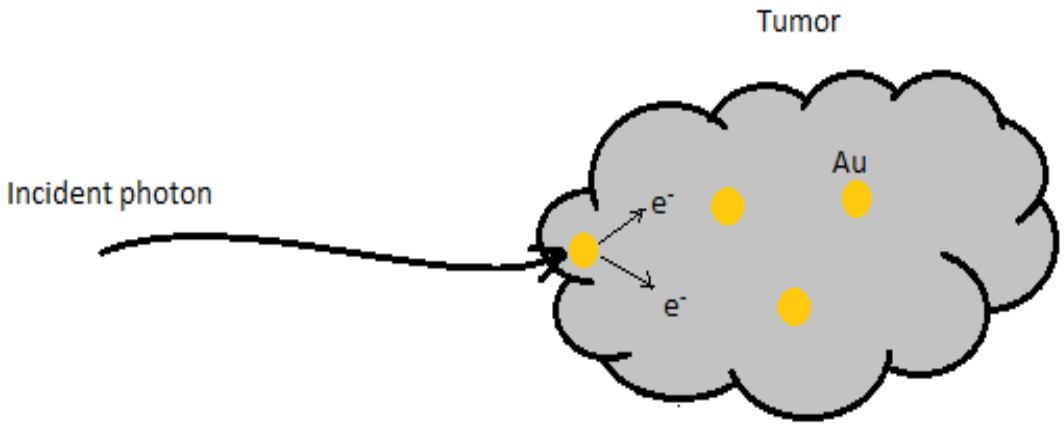

Figure 4.1: Dose enhancement mechanism showing production of Auger electrons due to photon-gold interaction.

The increase in dose effects were also realised in radiographic imaging procedures that used high-Z contrast agent such as iodine. Adams *et al.* (1977) estimated the effects of radiation in combination with contrast media by measuring chromosome aberrations in peripheral blood

lymphocytes and the study showed an increase in absorption of x-rays and breakage of chromosomes indicating the danger of iodine/radiation interaction to the cells [10]. Several studies also showed increasing damage to cells due to diagnostic x-rays [11,12].

Nevertheless, these undesirable effects in diagnostic radiology were found to be useful for radiotherapy where by these effects can be applied directly to tumours by loading the tumours with high-Z materials that will subsequently increase the radiation dose with much less damage done to the surrounding healthy tissue. *In vitro* study showed reduction of cells survival for cells irradiated with low energy x-ray (kilovolt) beams from clinical x-ray tubes in the presence of contrast media such as iodine [13-15]. Some studies investigated dose enhancement caused at high photon energies (megavoltage) and found it to be negligible compared to the kilovoltage range of energies. Studies with animals also showed tumours growth regression during use of kilovoltage beams [15]. Computational investigation using MC technique of modified linacs to alter the photon spectral confirms that dose enhancement is achieved more at lower energies compared to high energies [16,17]. Robar *et al.* (2002) studied modified x-rays beams (energy ranges from 6 to 24 MV) from Linacs and achieved dose enhancements up to 23% [18]. Therefore, treatment using conventional therapy machines, such as linacs that deliver megavolt range of energies will be a challenge to implement high-Z NPs localised dose enhancement since maximum dose enhancement occurs at low photon energy.

4.3 Gold Nanoparticles Dose Enhancement

Several *in vitro* and *in vivo* studies have established biocompatibility and safety of gold (Au) [19-23]. AuNPs can be easily produced in uniform sizes and shapes, including nanospheres, nanorods, shells, and cages [24]. Au possesses easily controllable surface chemistry allowing functionalization with various biologically useful molecules to help evade immune detection, tumour-targeting and crossing of biophysical barriers such as the blood-brain barrier [25,26]. Its high atomic number (Au,79) and a density of 19.3 $g.cm^{-3}$ gold exhibits a significantly increased photoelectric absorption cross-section compared to biological tissue especially around the k-edge of gold (80.7 keV) and at lower energies approximately 20 keV, therefore

allowing radiation dose enhancement [27]. Several methods can be employed to the synthesis of AuNPs to modify their functionality and delivery [28,29].

Regulla *et al.* (1998) demonstrated first the effects of Au on the radiation dose enhancement using gold sheet to measure the dose enhancement effects on cells with x-rays of energy ranging from 40 to 120 kVp. Later, Herold *et al.* (2000) measured radiosensitisation by Au nanoparticles using 1.5 to 3.0 μm gold microspheres injected directly in the tumours [30]. Since then, several studies have been carried out to test feasibilities of AuNPs for radiotherapy applications. Monte Carlo simulations have also been used to evaluate effects of AuNPs during radiation therapy [31,32].

Targeted delivery of AuNPs to tumour tissue can be accomplished in several ways that include direct routes of intratumoural injection and intraperitoneal administration [33]. Through enhanced permeability and retention (EPR) effect, intravenously (IV) administered bare Au exhibited selective accumulation in tumour tissue due to the tumour's characteristic leaky fenestrated vasculature and impaired lymphatic clearance [34,35.] EPR effect was demonstrated by Hainfeld *et al.* (2004) using a mice model and they found that a one-time injection of 2.7 g Au/kg body weight of 1.9 nm AuNPs led to accumulation within tumours of up 7 mg Au/g tumour [36]. The AuNPs also were found to be non-toxic to the mice and were cleared later from the body through the renal system.

4.4 Enhanced Permeation and Retention

Enhanced Permeation and Retention (EPR) effect is one of the major properties of tumours that is exploited by nanoparticles that has been used in various different drug delivery systems and is assumed to be the bases of NPs tumour targeting mechanism. Most of the tumours are composed of rapidly proliferating cells with little or no cell cycle regulation. This rapid and unregulated growth of cells requires a significant increase in blood supply within the tumour, as a result, tumour cells over-express certain growth factors, such as Vascular Endothelial Growth Factor (VEGF) and Tumour Necrotic Factor (TNF) thereby recruiting additional blood vessels to the tumour site [36].

The development of additional blood vessels around the tumour results in a lack of proper alignment of the endothelial cells in the vessels which will results in the development of wide gaps in the vessels. This gives rise to the characteristic leaky vessel phenomenon associated with tumour masses. Any particle circulating in the blood supply that is smaller than the gaps will then escape the leaky vessels at the tumour site thus allowing nanoparticles to pass through and accumulate at the tumour site [38]. Nanoparticles will stay at the tumour site since they are too large to re-enter the vessel through the normal endothelial gap junctions.

Several studies have investigated particles ranging between 10nm to 100nm since leaky vessels can be as large as several hundred nanometers [39,40]. NPs are stable in circulation hence remain in circulation for an extended period of time and eventually accumulate at the tumour site through this EPR effect [41].

4.5 Monte Carlo Simulations of High-Z Materials

In order to quantitatively determine NPs dose enhancement, computational algorithms, e.g. MC simulations are the most useful tools other than to measure directly using tools such as dosimeters which have technical limitations such as physical size or energy dependence. Monte Carlo simulations are designed to model the interactions between photons and charged particles with ease as they traverse matter.

A series of Monte Carlo simulation studies using various MC codes and radiation source models have been carried out to examine the effect of adding high-Z material to water or tissue-equivalent material in order to evaluate the localised enhancement of dose within the target volume. Landau and Binder (2005) demonstrated that MC simulations can be used to model the expected ionisation events and dose distributions under differing geometries, materials and external beam parameters [42].

Robar *et al.* (2002) are some of the early researchers that used MC simulations to investigate the possibility of dose enhancement using gadolinium (Gd) and iodine (I) contrast agents. Dose enhancement of up to 70% was seen with tumour contrast media concentration of 1g/ml,

although such concentrations are not clinically feasible. Dose enhancement of up to 15.8% and 23.1% was seen for iodine and gadolinium respectively using a 2 MeV photon beam at a clinically feasible concentration of 30 mg/ml. For high clinical MeV beams above 10 MeV smaller dose enhancement of 3.9% and 4.4% respectively were observed.

Another investigation on using gadolinium to enhance tumour dose was carried by Garnica-Garza (2011) using the electron-photon coupled transport MC code PENELOPE with an optimization algorithm and obtained a dose enhancement of 38% for a prostate cancer model [43]. This study focused more on modelling clinical physiologically accurate simulation geometry and measure doses delivered to non-tumour volumes as it explored contrast agent leakage, and non-uniform loading of the tumour.

A study by Cho (2005) investigated teletherapy and brachytherapy applications of high-Z material using MC simulations. For teletherapy photon energies of 4 MeV and 6 MeV dose enhancement of 3.2% and 7.4% respectively was achieved at a maximum Au concentrations of 30 mg/g. Dose enhancement of between 200% and 550% was obtained for a 140 kVp photon beam for 7 mg/g and 30 mg/g gold concentrations respectively although such significant dose enhancement has not been replicated in subsequent models . For the brachytherapy model a maximum dose enhancement of 30% was obtained. Cho *et al.* (2009) later undertook another study of AuNPs in brachytherapy models to more precisely define their effects.

References

1. Spiers FW, 1949. The Influence Of Energy Absorption and Electron Range on Dosage in Irradiated Bone.Br. J. Radiol; 22:521-533.

2. Spiers FW, 1951. II. Dosage in Irradiated Soft Tissue and Bone Radiotherapeutic Physics-//. Br. J. Radiol; 24:365-370.

3. Spiers FW, 1966. A Review of The Theoretical and Experimental Methods of Determining Radiation Dose in Bone.Br. J. Radiol; 39:216-221.

4. Alm-Carlsson G, 1973. Dosimetry of interfaces. Theoretical Analysis and Measurements by Means of Thermoluminescent LiF. ActaRadiologica. Suppl; 332.

5. Das IJ, Chopra KL, 1995. Backscatter Dose Perturbation in Kilovoltage Photon Beams at High Atomic Number Interfaces. Medical Physics; 22:767–773.

6. Johns HE, Hunt JW, Fedoruk SO, 1954. Surface Back-Scatter in The 100 kV to 400 kV Range. Br. J. Radiol; 27:443–448.

7. Rosengren B, Wulff L, Carlsson E, Carlsson J *et al.*, 1993. Backscatter radiation at tissue-titanium interface, biological effects from diagnostic 65 kVp x-rays. ActaOncologica; 32:73–77.

8. Regulla DF, Hieber LB, Seidenbusch M, 1998. Physical and biological interface dose effects in tissue due to x-ray induced release of secondary radiation frommetallic gold surfaces. Radiation Research; 150:92–100.

9. Zellmer DL, Chapman JD, Stobbe CC *et al.,* 1998. Radiation fields backscattered from material interfaces: I. Biological effectiveness. . Radiation Research; 50:406–415.

10. Adams FA, Norman A, Mello RS, Bass D, 1977. Effects of radiation and contrast media on chromosomes Radiology; 124:823-826.

11. Callisen HH, Norman A, Adams FH, 1979. Absorbed dose in the presence of contrast agents during pediatric cardiac cathetherization Med. Phys; 6(6):504-509.

12. Cochran ST, Koudadoust A, Norman A, 1980. Cytogenetic effects of contrast material inpatients undergoing excretory urography. Radiology; 136:43-46.222

13. Dawson P, Penhaligon M, Smith E, Saunders j, 1987. Iodinated contrast agents as radiosensitisers. Br. J. Radiol; 60:201-203.

14. Matsubara S, Katoh T, Kubota N *et al.,* 1994. The effects of x-ray energy and an iodine-based contrast agent on chromosome aberrations Radiation Research; 137:231-237.

15. Mello RS, Callisen H, Winter J *et al.,* 1983. Radiation dose enhancement in tumours with iodine Med. Phys; 10:75-78.

16. Solberg TD, Iwamoto KS, Norman A, 1992. Calculation of radiation dose enhancement factors for dose enhancement therapy of brain tumours. Phys. Med. Biol; 37:439-443.

17. Mesa AV, Norman A, Solberg TD *et al.*, 1999. Dose Distributions using kilovoltage x-rays and dose enhancement from iodine contrast agents,.Phys. Med. Biol; 44:1955-1968.

18. Robar JL, Riccio SA, Martin MA, 2002. Tumour dose enhancement using modified megavoltage photon beams and contrast media.Phys. Med. Biol; 47:2433-2449.

19. Khlebtsov N, Dykman L, 2011. Biodistribution and toxicity of engineered gold nanoparticles: a review of in vitro and in vivo studies. ChemSoc Rev; 40:1647-1671.

20. Connor EE, Mwamuka J, Gole A, *et al.,* 2005. Gold nanoparticles are taken up by human cells but do not cause acute cytotoxicity. Small; 1:325-327.

21. Lasagna-Reeves C, Gonzalez-Romero D, Barria MA *et al*., 2010. Bioaccumulation and toxicity of gold nanoparticles after repeated administration in mice. BiochemBiophys Res Commun; 393:649-655.

22. Coulter JA, Jain S, Butterworth KT, *et al.,* 2012 Cell type-dependent uptake, localization, and cytotoxicity of 1.9 nm gold nanoparticles. Int J Nanomedicine; 7:2673-2685.

23. Shukla R, Bansal V, Chaudhary M, *et al.*, 2005. Biocompatibility of gold nanoparticles and their endocytotic fate inside the cellular compartment: a microscopic overview. Langmuir; 21:10644-654.

24. Cai W, Gao T, Hong H, *et al.,* 2008. Applications of gold nanoparticles in cancer nanotechnology. NanotechnolSciAppl:17-32.

25. Jain S, Hirst DG, O'Sullivan JM, 2012. Gold nanoparticles as novel agents for cancer therapy. Br J Radiol; 85:101-113.

26. Praetorius NP, Mandal TK, 2007. Engineered nanoparticles in cancer therapy. Recent Pat Drug DelivFormul; 1:37-51.

27. Hainfeld J, Dilmanian F, Slatkin D and Smilowitz H, 2008. Radiotherapy enhancement with gold nanoparticles Journal of Pharmacy and Pharmacology; 60:977–985

28. Turkevich J, Stevenson PC, Hillier J, 1951. A study of the nucleation and growth processes in the synthesis of colloidal gold. Discuss Faraday Soc; 11:55-75.

29. Brust M, Walker M, Bethell D, *et al.,* 1994. Synthesis of thiol-derivatised gold nanoparticles in a two-phase liquid-liquid system. J ChemSocChemCommun; 7:801-802.

30. Herold DM, Das IJ, Stobbe CC, *et al.,* 2000. Gold microspheres: a selective technique for producing biologically effective dose enhancement Int. J. Radiat. Biol. 76 1357–64.

31. Cho SH, 2005. Estimation of tumour dose enhancement due to gold nanoparticles during typical radiation treatments: a preliminary monte carlo study. Phys.Med.Biol; 50:163-173.

32. Cho SH, Jones BL, Krisnan S, 2009. The dosimetric feasibility of gold nanoparticle-aided radiation therapy (GNRT) via brachytherapy using low-energy gamma-/x-ray sources. Phys. Med. Biol; 54:4889-4905.

33. Wang H, Zheng L, Peng C, *et al.,* 2011. Computed tomography imaging of cancer cells using acetylated dendrimer-entrapped gold nanoparticles. Biomaterials; 32:2979-2988.

34. Iyer AK, Khaled G, Fang J, *et al.*, 2006. Exploiting the enhanced permeability and retention effect for tumour targeting. Drug Discov Today; 11:812-818.

35. Fang J, Sawa T, Maeda H, 2003. Factors and mechanism of "EPR" effect and the enhanced antitumour effects of macromolecular drugs including SMANCS. AdvExp Med Biol; 519:29-49.

36. Hainfeld JF, Slatkin DN, Smilowitz HM, 2004. The use of gold nanoparticles to enhance radiotherapy in mice.Phys Med Biol; 49:N309-315.

37. Ferrara N, Houck K, Jakeman L. *et al.,* 1992. Molecular and biological properties of the vascular endothelial growth factor family of proteins. Endocr Rev; 13:18–32.

38. Torchilin VP, 2007. Targeted pharmaceutical nanocarriers for cancer therapy and Imaging.Aaps Journal; 9(2):E128-E147.

39. Maeda H, 2001. SMANCS and polymer-conjugated macromolecular drugs: advantages in cancer chemotherapy. Advanced Drug Delivery Reviews; 46(1-3):169-185.

40. Arap W, Pasqualini R, and Ruoslahti E, 1998. Cancer treatment by targeted drug delivery to tumour vasculature in a mouse model. Science; 279(5349):377-380.

41. Duncan R and Sat YN, 1998. Tumour targeting by enhanced permeability and retention (EPR) effect. Annals of Oncology; 9:149.

42. Landau, D. P. and K. Binder (2005). A guide to Monte Carlo simulations in statistical physics. Cambridge, UK, Cambridge University Press.

43. Garnica-Garza HM, 2011. Treatment planning considerations in contrast-enhanced radiotherapy: energy and beam aperture optimization. Physics in Medicine and Biology; 56(2):341-355.

Chapter 5: MATERIALS AND METHODS

5.1 Introduction

This study was done using computer simulations on a Linux platform. Hardware and a variety of software codes were used namely: BEAMnrc, BEAMDP, DOSXYZnrc, MCSHOW and XMgrace as well as FORTRAN, IDL and Excel. It was used to model the 6 MV flattening filter free (FFF) Elekta precise linac and the determination of the dose deposited within the tumour that contained nanoparticles (NPs) using DOSXYZnrc. Dose enhancements were evaluated for x-rays produced in different Bremsstrahlung targets.

5.2 Parameters Investigated

The parameters studied included the photon energy spectral distribution and mean energies obtained from three categories of external beam sources based on altered Bremsstrahlung x-ray targets. The three categories of targets simulated consisted of a conventional 0.3cm thickness tungsten target, followed by other target models that contained carbon and water layers (ranging from 0.1 cm to 4cm thickness) combined with tungsten target (ranging from 0.07cm to 0.2cm thickness), using a 6 MV FFF Elekta precise linac. The FFF linac option was chosen to avoid beam filtering. The subsequent dose enhancement was evaluated using atoms of gold attached to NPs (0.5nm).The AuNPs concentration was expressed in milligrams per gram of tumour with a concentration of typically 7mg/1000mg. For dose calculations and beam characterisation, PDDs and planar dose profiles were calculated. The dose calculations in a constructed patient CT phantom were evaluated based on three dimensional conformal radiotherapy (3DCRT) for 4, 5 and 6 fields. All simulations were carried using EGSnrc based MC codes.

5.3 Monte Carlo Simulation

The EGSnrc based BEAMnrc MC code was used to simulate the linac head components. The DOSXYZnrc code was used to simulate the transport of photons, electrons and positrons through a 3-dimensional water and a CT based patient phantom. BEAMDP was used to extract photon energy spectra, electron spectra and combining phase space files from the results of

BEAMnrc simulations. MCSHOW program by Ma *et al.* (2002) was used to display dose distribution on the phantom image to extract, PDDs and planar dose profiles, to evaluate altered Bremsstrahlung target dose enhancement using AuNPs.

5.3.1 BEAMnrc Simulations

The FFF 6MeV Elekta Precise linear accelerator head geometry was modelled using BEAMnrc Only head components exposed to the beam from the exit window were modelled using component modules (CMs). The code was running under the open Suse version 10.3 Linux operating system installed on an intel(R) Xeon(R) CPU, with 16 processors with a speed of 2.40 MHz each and a RAM size of 16 GB. All simulations were compiled and run using BEAMnrc graphical user interface.

The model was built using information regarding the geometry in appendix A. The material compositions of different components were provided by the manufacturer. See appendix B for an example on an input file.

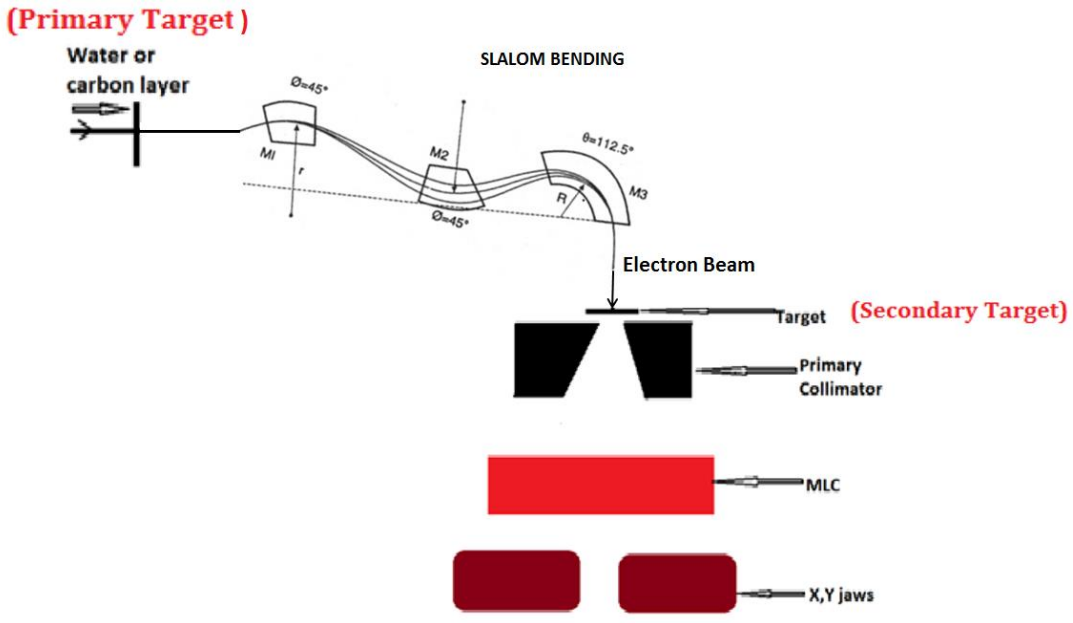

Figure 5.1: Schematic diagram showing a proposed modified FFF 6 MeV Elekta Precise Linac model with a 112.5^0 (slalom) bended beam. (Adapted from Podgorsak EB, 2006. IAEA publication. Radiation Oncology Physics: A Handbook for Teachers and Students)

The study assumes that a primary target or a moderator set at the end of the wave guide slows down electrons before being bent to fall in on the secondary target that contains tungsten only. By adjusting the thickness of the primary target layer the electron energy can be reduced before being bent and falling in on the secondary tungsten target. The bending magnet was deliberately ignored in this model.

The original incident beam is a 6 MeV mono-energetic electron beam of radius 0.1 cm directed at the water or carbon layer designed to slow down electrons. The layers where simulated using the SLABS CM. At the back of this CM a phase space file was scored and BEAMDP was used to extract the energy spectra and angular distribution of the slowed down electrons. This was used as the electron source that would fall in on the secondary target.

The second part of the linac model consisted of the secondary Bremsstrahlung x-ray target, primary collimator, MLCs and the X/Y jaws. The Bremsstrahlung tungsten x-ray target was modelled using the SLABS CM. The primary collimator was modelled using the FLATFILT CM made from heavy metal alloy (HMA). HMA is mixture of W, Ni, and Cu. A linac model that consisted of a conventional tungsten target of 0.3 cm thick was also modelled for comparison purpose.

The secondary collimation consisted of MLCs and X/Y jaws. The HMA MLC was modelled using the MLCQ CM. It consists of two banks of 40 independent leaves each, with thickness of 7.5cm.The XY-jaws were modelled using the JAWS CM made from HMA. The bottom surface of the MLC and the jaws was positioned at 37.3 cm and 50.9 cm respectively from the photon source. The PS file was scored at the bottom surface of the jaws and it was used as an input source in subsequent simulations and calculations in DOSXYZnrc.

The transport parameters set for the BEAMnrc code (Kawrakow, 2000) included the electron energy cut-off (ECUT) of 0.521 MeV and photon energy cut-off (PCUT) of 0.01 MeV. These cut off energies were set in order not to bias the high energy transport and to reduce the effect of very low dominant energy transport during tracking. The simulation time is strongly dependent on the ECUT value and thus it is important to use a value as high as possible. Similarly, PCUT is

the photon equivalent of ECUT but the value of PCUT is not critical since low PCUT values do not lead to a longer simulation time. The boundary crossing algorithm was EXACT and the electron step algorithm was PRESTA-II. The user adjustable values for other parameters such as ESTEPE were set to be 0 so that the PRESTA defaults are used. ICRU-700 compositions and stopping power values as illustrated in ICRU 1984 were used for the materials used in the linac model and DOSXYZnrc phantoms. Simulations were run using $3x10^8$ histories to obtain PS files with no more than 1% variance.

5.3.2 Phase-space Files

In the first model, a phase space file was scored at the back of either the water or carbon layer inserted in the path of electron beam as shown in figure 5.1. BEAMDP was used to extract the altered electron spectrum. The electron spectrum file obtained was used as an input source to the secondary tungsten target to generate the Bremsstrahlung x-rays. At the bottom of the jaws a second PS file was obtained containing the information of the photon beam generated from the Elekta precise linac head. These PS files were analysed by BEAMDP to extract parameters including photon energy spectral distributions. The PS files were also used in DOSXYZnrc simulations for water phantom simulations as well as patient CT phantom simulations.

5.3.3 BEAMDP

BEAMDP is a computer program developed to analyse the parameters of the PS files generated by BEAMnrc such as spectral, directional, fluence and energy fluence.

5.3.4 DOSXYZnrc Simulation

Once the linac was simulated the DOSXYZnrc/EGSnrc based MC code was used to calculate the dose scored in a cubic water phantom and CT patient phantom by using the PS files scored at the back of the secondary target as its beam source input. Several simulations were done with different spectral data characterizing the photon source.

DOSXYZnrc is a general-purpose EGSnrc code for 3-dimensional absorbed dose calculations that simulates the transport of photons and electrons in a rectilinear geometry and scores the

energy deposition in the designated volume elements. The results of the DOSXYZnrc simulations is a set of 3D dose files, linked to each photon beam.

Each PS file generated from the second part of the linac head, just below the jaws at 50.9cm from the x-ray source, was used as an input source for DOSXYZnrc. Water phantom simulations where carried out for the purpose of characterizing the photon beams generated from BEAMnrc simulations and the CT based patient phantom was used to simulate dose enhancement of high-Z NPs seeded in a tumour. All simulations to calculate dose was compiled and run using the DOSXYZnrc Graphical user interface. The STATDOSE code was used to extract PDD's and cross beam profiles. All DOSXYZnrc simulations were run using approximately $3x10^9$ histories reducing statistical uncertainty to less than 1%. The ECUT and PCUT values were 0.521 and 0.01 MeV respectively in both water and the patient CT phantom. Although low energy interactions were of greater importance to this work, the PCUT value used was appropriate as the photoelectric effect which is the main contributor to NPs dose enhancement is dominant at energies ranging between 0.01 to 1 MeV (See figure 2.7).

5.3.4.1 Water Phantom Simulations

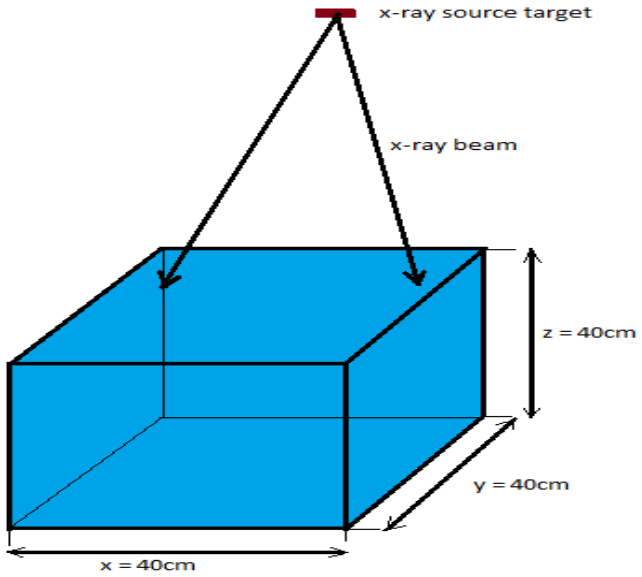

Figure 5.2: Schematic diagram of DOSXYZnrc 3-dimensional water phantom model. The x-ray source target was the particles scored in PS files behind the secondary target.

The first stage was to characterize the photon beams generated after electrons were slowed down by low-Z primary targets using PS files generated in BEAMnrc as input sources to DOSXYZnrc. To compute photon beam data, a 40 × 40 × 40 cm^3 cubic water phantom with a source-to-surface distance of 100 cm was simulated.

The water phantom had 200 dose scoring voxels set at 0.2 cm size each in all the three directions x, y and z. The SSD was set by shifting the DOSXYZnrc phantom isocentre distance 49.1 cm downstream from the 50.9 cm distance from the target to the bottom end of the jaws. The water phantom geometry is shown on figure 5.2 above. Depth dose and dose profile curves were calculated for open fields of 5 × 5 cm^2, 10 × 10 cm^2 and 20 x 20 cm^2. Dose profile data for all beams were calculated at 5cm and 10cm depth respectively. For these simulations, ECUT and PCUT were set to 0.521 and 0.01 MeV, respectively.

5.3.4.2 Patient CT Phantom Simulation

Once the linac and beams were characterized, the DOSXYZnrc code was used to calculate the dose scored in a realistic patient CT phantom by using PS files from BEAMnrc to evaluate NPs dose enhancement. The CT patient phantom contained the prostate as the planning treatment volume (PTV) as defined by contouring. The PTV was a mixture AuNPs and the prostate tumour.

Several simulations were done with each simulation using different spectral data characterizing the photon source. Three treatment plans (4, 5 and 6 fields treatment plans) were simulated using 3DCRT. The beam angles and the jaws and collimator aperture values were constructed with the aid of XiO Treatment Planning System (TPS) before being incorporated into BEAMnrc and DOSXYZnrc.

5.4 Introducing High-Z Nanoparticles into the Tumour

Generating a realistic patient CT phantom with prostate tumour seeded with NPs was achieved with the manual contouring of prostate on the patient CT data set using the MCSHOW program by Ma *et al.* (2002) as shown on fig 3 below. The MCSHOW GUI was used to do slice-by-slice delineation of prostate tumour and displaying of isodose distributions on patient CT datasets.

The CT data was generated using ctcreate which is a FORTRAN program that converts CT data into a form that is readable by DOSXYZnrc.

After contouring all the CT data, an in-house code based on IDL (Appendix C) was used to convert the prostate tissue contained in the drawn volume into tissue that contains the NPs. The resulting phantom was saved in the egs4phant format that is readable by DOSXYZnrc.

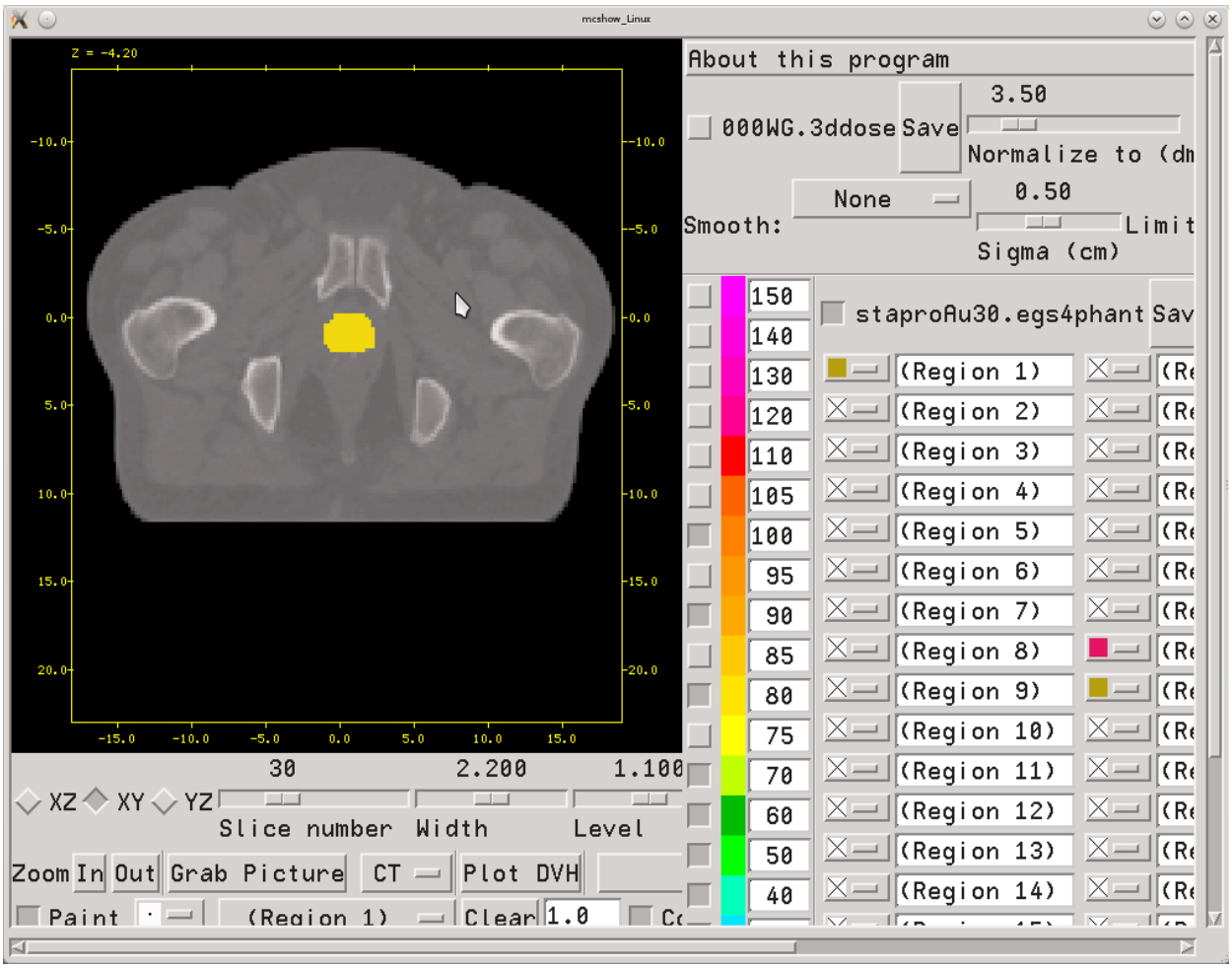

Figure 5.3: MCSHOW GUI showing a slice delineation of the prostate (shown as a yellow region of interest).

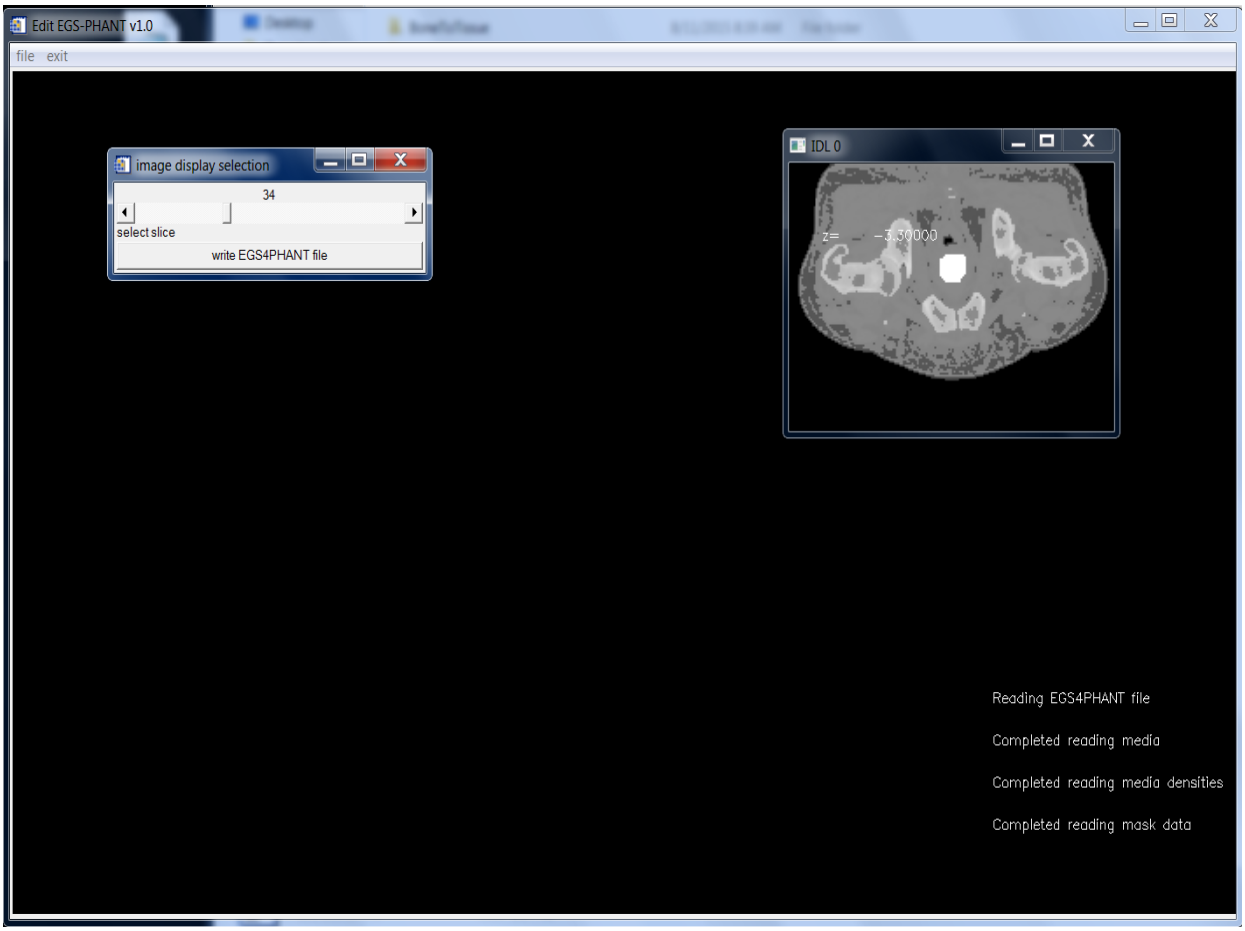

Figure 5.4: IDL code display window showing the output of a new egs4phant file that contains tumour/NPs mixture in the CT image (shown as a white region of interest).

The tumour/NPs mixture consisted of atoms of Gold (0.28 nm) and adenocarcinoma (ACA) type of prostate cancer. The chemical and elemental compositions of ACA were defined by the International Commission on Radiation Units and Measurements (ICRU) [1]. The Au atoms were assumed to be uniformly distributed throughout the tumour at a concentration of 7mg/1000mg of tumour, based on the previous studies [2]. The mixture of nanoparticles and tumour was generated using the EGSnrcMP and the concentration of AuNPs was kept constant throughout the simulations.

Table 5.1 below shows the elementary composition by weight and respective densities for ACA tumour and ACA/Au mixture. These chemical compositions were included since there are required for generating PEGS data needed during MC simulations to enable calculation of dose

deposition in the medium. The first row in the table is showing all the elements that are found in either ACA or ACA/Au mixture. The second row represents elementary composition of ACA as a percentage followed by the percentage composition for ACA/Au mixture. The third row shows the densities of individual elements in both ACA and ACA/Au mixture followed by their density as a fraction of the entire mixture.

Table 5.1: Elementary composition by weight and respective densities for ACA and ACA/Au mixture.

Element	H	C	N	O	Na	P	S	Cl	K	Au
ACA %	9.900	26.90	4.500	56.900	0.198	0.396	0.504	0.306	0.396	0.000
ACA/Au mix %	9.831	26.713	4.469	56.504	0.197	0.393	0.500	0.304	0.393	0.695
Density	0.090	2.260	1.251	1.429	0.970	1.820	2.070	3.214	0.86	19.32
Fractional density	0.0088	0.6037	0.0156	0.8074	0.0019	0.0071	0.010	0.009	0.003	0.134

5.4.1 PEGS4

The PEGS4 data which will be read by the DOSXYZnrc code during patient CT phantom simulation for this Au/Tumour mixture was generated using the EGSnrcMP GUI, using information in table 5.1 above. A tumour without NPs was also generated. The EGSnrcMP PEGS Data user inputs include the percentage compositions by weight of each of the elements that comprise the Au/Tumour composition (H, O, N, C, Na, S, Cl, K, and Au), the mass density of the material (1.6025 gcm^{-3}), the medium type (mixture) as well as the electron and photon energy cut-offs of 0.521 and 0.01 MeV respectively. The outlay of the PEGS Data GUI is shown in figure 5.5.

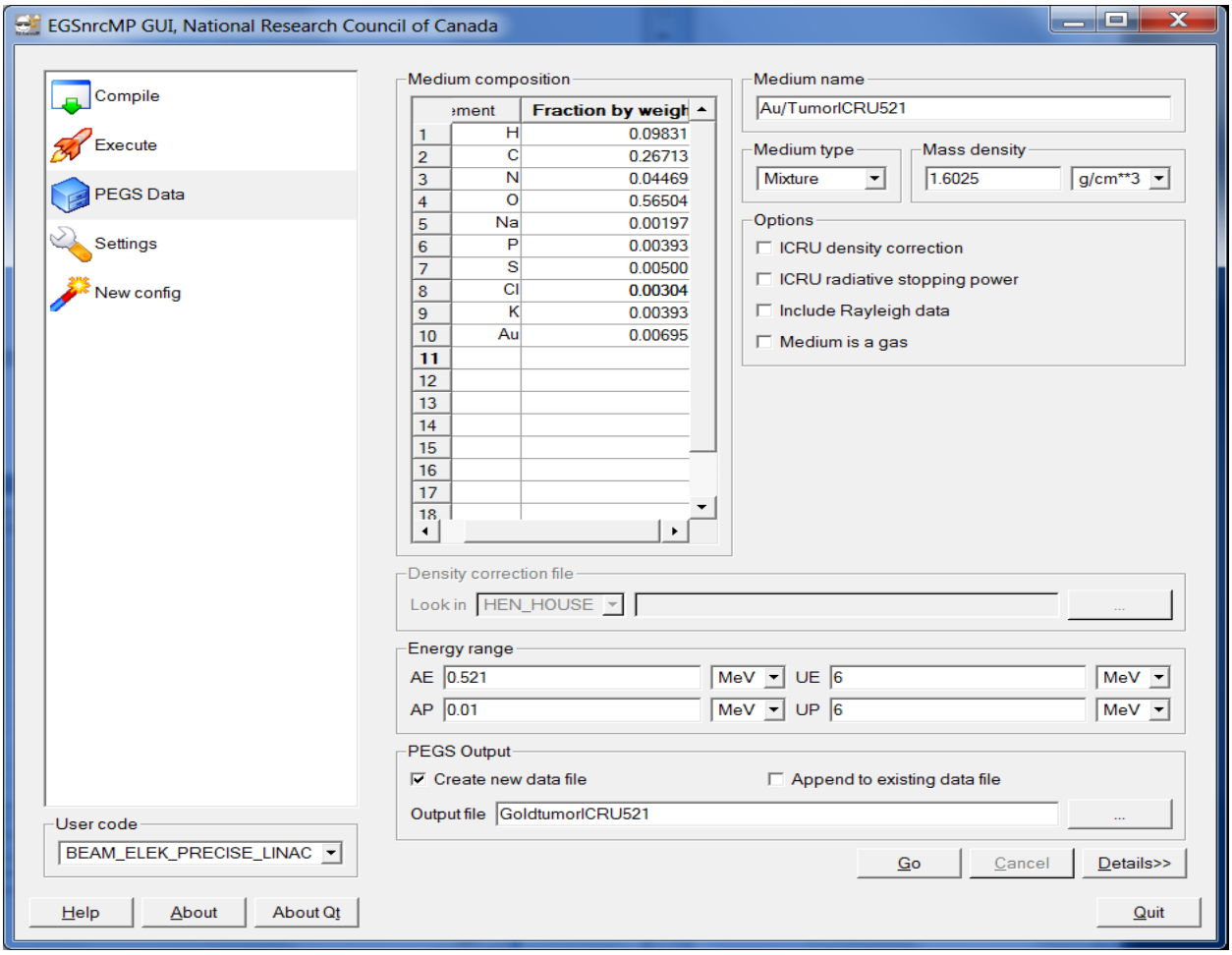

Figure 5.5: EGSnrcMP GUI showing input parameters for generating PEGS4 data for Au/Tumour mixture.

5.5 Treatment Planning Model for CT Based Patient Dose

Three treatment plans were constructed with the aid of our XiO Treatment Planning System (TPS) before being incorporated into DOSXYZnrc. The treatment plan parameters were obtained using XiO plan data for a 3DCRT treatment of the prostate tumour using pre-determined MLC and jaw settings. The isocentre of the gantry was located at the centre of the planning target volume (PTV) at 100 cm source-to-axis distance (SAD).

All plans simulated ensured 100% of the PTV was covered with 1 cm margin around the prostate and they were all generated on the same patient's anatomy from a planning CT scan. The gantry angles used are 0°and 180° for AP/PA beams, 90° and 270° for lateral beams

passing through the pelvis and 45°, 135°, 225°and 315° for opposite pairs of oblique angle beams, all at an couch angle of 0°. The field setups for the plans were a four field box, a five field and six field plan. Since the coordinate system for beam orientation in the XiO TPS used is not the same as with the one used in DOSXYZnrc, transformations where carried out to enable correct translation of beam, gantry, couch and MLC angles and is discussed below.

5.5.1 DICOM TO DOSXYZnrc Transformation

BEAMnrc and DOSXYZnrc define beam orientation in a different way compared to the XiO TPS. Usually a TPS uses the defined DICOM coordinate system which is the existing standard for communications between different diagnostic and therapeutic modalities. Therefore, since the particle and photon transport simulation code used in this study cannot read DICOM TPS generated plans, transformation of the coordinate system was necessary to convert the patient setup and beam orientation information from DICOM to DOSXYZnrc.

Zhan *et al.* (2012) derived equations which were computationally implemented and verified on plans generated from Eclipse and Pinnacle TPS's. The equations takes into account the gantry angle(θ_G) , the treatment couch angle (θ_T), the polar angle(θ) defined by equation 5-1, the azimuthal angle (ϕ)defined by equation 5-2 and collimator rotational angle ($\Phi_{col}^{(beam)}$) whereby:

$$\theta = cos^{-1}(\sin\theta_T \cos\theta_G) \tag{5-1}$$

$$\phi = tan^{-1}\left(\frac{-\cos\theta_G}{cos\theta_T\, sin\theta_G}\right) \tag{5-2}$$

$$\Phi_{col}^{(beam)} = \frac{3\pi}{2} - \theta_c tan^{-1}\left(\frac{-\sin\theta_T \cos\theta_G}{cos\theta_T}\right) \tag{5-3}$$

Collimator rotational angle equation 5-3, was derived taking into account that the BEAMnrc generated PS file does not use similar coordinates as DOSXYZnrc.

Table 5.2: DICOM to DOSXYZnrc transformations for beams orientation

Treatment Plan	Beam	DICOM			DOSXYZnrc		
		θ_c	θ_G	θ_T	$\Phi_{col}^{(beam)}$	θ	Φ
4 Field box	1	0	0	0	270	90	-90
	2	0	180	0	270	90	90
	3	0	270	0	270	90	180
	4	0	90	0	270	90	0
5 Field	1	0	0	0	270	90	-90
	2	0	315	0	270	90	225
	3	0	135	0	270	90	45
	4	0	45	0	270	90	-45
	5	0	225	0	270	90	135
6 Field	1	0	0	0	270	90	-90
	2	0	180	0	270	90	90
	3	0	315	0	270	90	225
	4	0	135	0	270	90	45
	5	0	45	0	270	90	-45
	6	0	225	0	270	90	135

5.5.2 Combining Dose Files

A FORTRAN code in appendix D was developed locally at the department to combine individual 3ddose files produced from DOSXYZnrc phantom simulations, to produce a single dose file that contains the total dose information from all the treatment fields used in a multiple-field plan.

5.6 Calculating Tumour Dose Enhancement Factors

Having completed simulations with patient CT phantom using DOSXYZnrc code, dose enhancement within a tumour volume was calculated. This was done using separate simulations based on the photon spectra obtained from the target combination between carbon and tungsten and water and tungsten using an unflattened beam.

Dose enhancement was quantified by calculating the dose enhancement factor (DEF) defined as the ratio of average dose obtained in the tumour with and without NPs at the isocentre using altered spectral beams obtained from 6 MV photon beams using FFF linac. DEFs are defined by the formula:

$$\text{DEF} = \frac{\text{Isocentre tumour dose obtained in NPs seeded tumour}}{\text{Isocentre tumour dose in tumour without NPs}}$$

The number of histories simulated for each case ensured that the average statistical uncertainty in dose calculation in patient CT phantom with and without NPs was reduced to below 1%.

The uncertainty in DEFs was 1.5%. This was calculated as the standard deviation of the average values of the DEFs for the number of history simulated.

References

1. Maughan RL, Chuba PJ, Porter AT *et al.,* 1997. The elemental composition of tumours: Kerma data for neutrons: Med. Phys; 24,1241.

2. Hainfeld JF, Slatkin DN, Smilowitz HM, 2004. The use of gold nanoparticles to enhance radiotherapy in mice. Phys Med Biol; 49:N309-315.

Chapter 6: Results and Discussions

6.1 Introduction

In this section the results obtained from BEAMnrc simulations of the primary target and 6 MeV flattening filter free (FFF) Elekta linac head are provided. DOSXYZnrc simulation results for a 3-dimensional water phantom and a constructed patient CT phantom are also presented. The results focused on the finding and use of suitable Bremsstrahlung targets for tumours enriched with nanoparticles (NPs) for radiation dose enhancement. This was made possible by investigating energy spectra produced by water/tungsten and carbon/tungsten primary/Bremsstrahlung target combinations of various thicknesses.

To characterise the x-ray beams through evaluation of dose enhancement in these tumours, one of the target material thicknesses was kept constant among tungsten, carbon and water for comparison. Results of a beam from an unaltered Bremsstrahlung tungsten target layer of 0.3 cm thickness were included denoted by “Unaltered”. The number of histories simulated for each case was enough to reduce the average statistical uncertainty to below 1%.

6.2 Primary Target Electron Beam Results

Figure 6.1 shows the MC model of the primary target simulated using BEAMnrc. The primary target was either a water or a carbon layer with thicknesses ranging between 0.1 cm and 4.0 cm. A 6 MeV electron beam was directed onto the target and phase space (PS) files were collected at a plane just below the primary target for beam analysis purposes. This primary target was introduced to act as a moderator to slow the 6 MeV electrons down in order to generate softer x-ray beams in a secondary Bremsstrahlung target.

BEAMDP was used to extract the spectral distribution, energy fluence data and angular distributions of electrons from the PS files obtained just below the primary target. The electron cut-off energy used was 0.521 MeV.

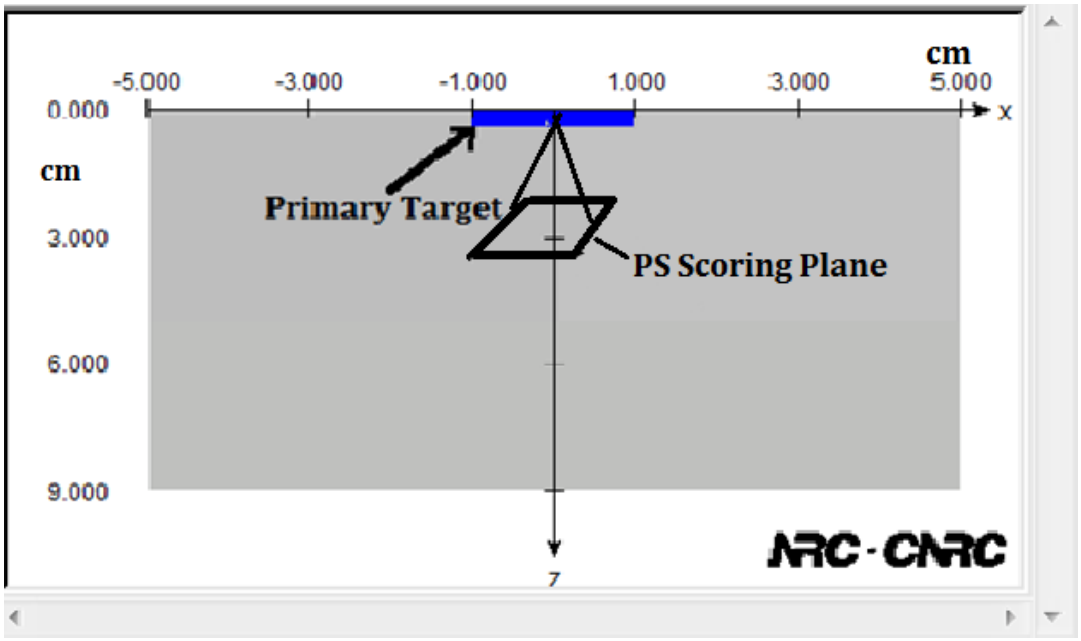

Figure 6.1: BEAMnrc MC model for the primary target which comprised different thicknesses of water or carbon, designed to reduce the electron energy from an original value of 6 MeV.

6.2.1 Electron Beam Mean Energy

Table 6.1 (a) and (b) show the calculated mean energy of the original 6 MeV electrons that traversed the primary target made up of different thicknesses of water or carbon. Water and carbon were chosen in this study due to their smaller atomic number which reduces the amount of Bremsstrahlung events that may cause hazardous levels of unwanted radiation. The energies were calculated from electron energy spectra extracted from the above PS files using the BEAMDP code.

Table 6.1

(a) Mean electron energies after traversing different thicknesses of water layers.

Water Layer (cm)	0.1	0.4	0.8	1.4	2.0	2.5
Mean Electron Energy (MeV)	5.74	5.07	4.20	2.93	1.85	1.19

(b) **Mean electron energies after traversing different thicknesses of carbon layers.**

Carbon Layer (cm)	0.1	0.4	0.8	1	1.2	1.4
Mean Electron Energy (MeV)	5.51	4.23	2.59	1.83	1.22	0.957

The mean energy of the exit electrons decreases with increase in primary target thickness due to mostly collisional losses.

6.2.2 Electron Beam Energy Spectra

Figure 6.2 shows normalised electron energy spectra obtained at a plane just below the primary target for different thicknesses of water and carbon layers. The energy spectra were extracted from PS files collected below the water or carbon target hit by a 6 MeV electron pencil beam.

According to figure 6.2 (a) at 0.1 cm water layer thickness, there is no energy straggling, just a sharp peak with a 0.25 MeV drop in the peak energy due to the 0.1 cm water target thickness. For thinner targets there is less absorption of the incident electron beam. As the water thickness increases the energy spectra begins to show signs of energy straggling, therefore leading to lower mean electron energy.

The energy straggling becomes more visible at 0.8 cm and the energy components stretch to a minimum of 4 MeV. As we go further to the 2 cm thickness the energy straggling is more pronounced leading to more lower energy components for electrons and at 2.5 cm it is even more pronounced.

(a)

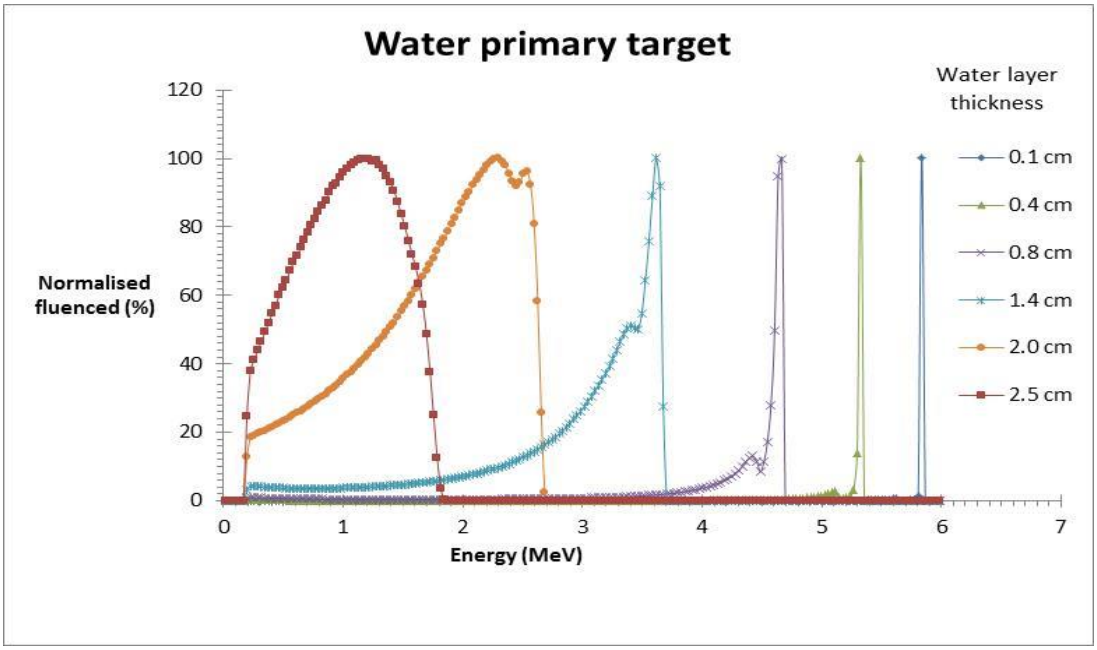

(b)

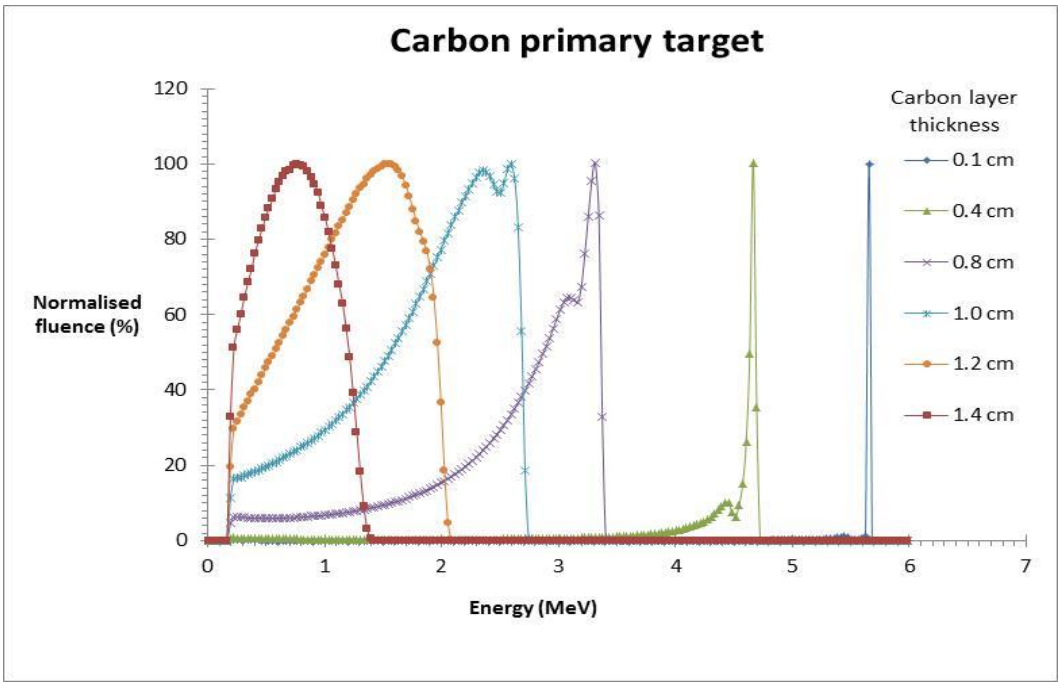

Figure 6.2: Electron energy spectra for primary target material of (a) water and (b) carbon layers at different thicknesses. The incident pencil beam of electrons had an energy of 6 MeV.

According to figure 6.2 (b) at 0.1 cm carbon layer there is no energy straggling. It is also just a 0.4 MeV drop in the peak energy due to the 0.1 cm carbon target thickness. As the carbon thickness increases the energy spectra begins to show signs of energy straggling as well. The energy straggling is more pronounced beginning from 0.4 cm leading to more lower energy components for electrons. For thickness larger than 1.4 cm the target begins to generate Bremsstrahlung x-rays only that is not suitable for use in the secondary Bremsstrahlung tungsten target. In the case of the more dense carbon, the thickness at which only the weak Bremsstrahlung occurs is just beyond 1.4 cm opposed to just above 3.0 cm in water. The density of carbon is 2.27 times that of water and the ratio of 3 and 1.4 is 2.14 which is closer to 2.27 when density scaling is applied to thickness.

6.2.3 Electron Beam Energy Fluence

Figure 6.3 shows the normalised fluence versus position for electron beams obtained at a plane just below the primary target (the PS files obtained above) for different thicknesses of water and carbon layers.

According to figure 6.3 (a) and (b) it is evident when a pencil beam of electrons passes through an absorbing medium such as water or carbon, the electrons undergo multiple scattering. This causes the original pencil beam to spread out to form a fluence distribution. This is due to Coulomb interactions between the incident electrons and nuclei of the absorber. The scattering of electrons traversing a path length (l) through this absorbing medium is described by the mean square scatter angle, $\bar{\theta}^2$ that is proportional to the mass thickness (ρl) of the absorber. Therefore the spatial spread of electrons in water or carbon is explained by the mass scattering power (T/ρ) define by ICRU as:

$$\frac{T}{\rho} = \frac{\theta^2}{\rho l} \tag{6.1}$$

(a)

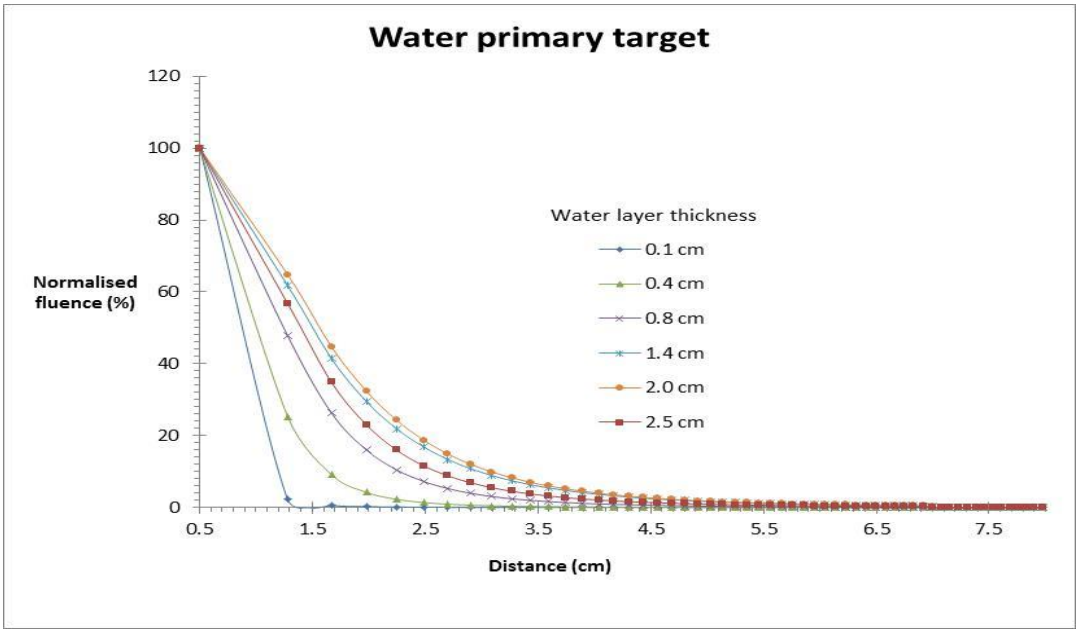

(b)

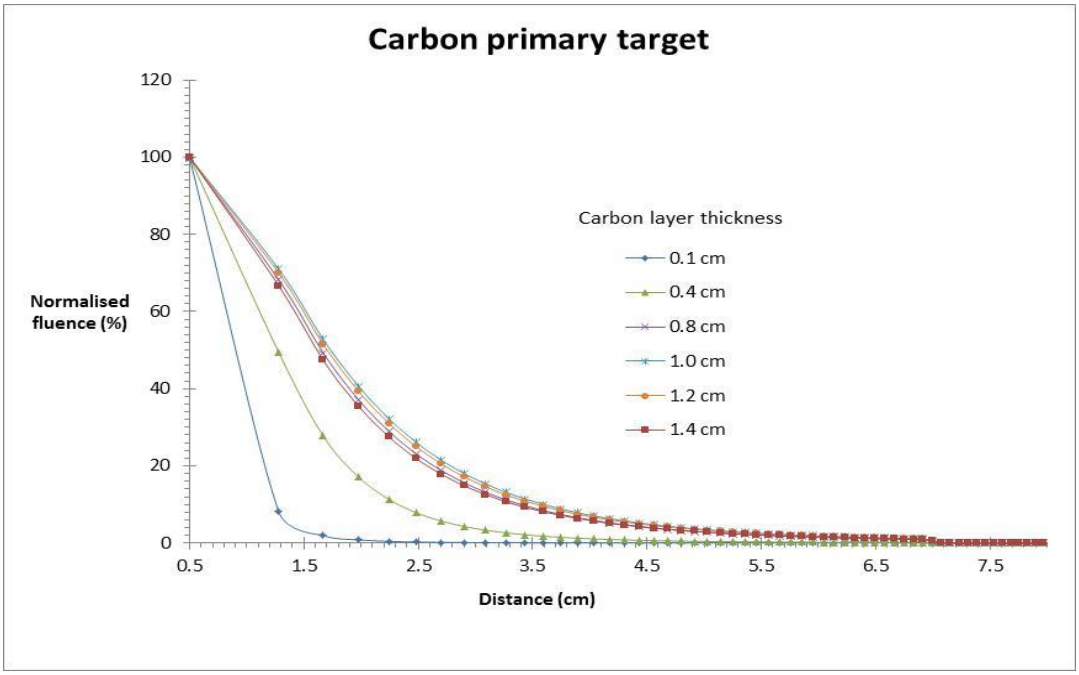

Figure 6.3: Electron fluence plots for primary target material of either (a) water or (b) carbon layers.

Therefore according to figure 6.3 (a) and (b) and equation 6.1, the lateral electron spread at 0.1 cm thickness is less as compared to 4 cm, say, 1.4 cm for carbon and 2.5 cm for water .

6.2.4 Electron Beam Angular Distribution

Figure 6.4 shows the angular distribution of electrons at the plane immediately below the primary target for different thicknesses of water and carbon layers. All angular distributions have been normalized to their maximum value and considered all electrons reaching the PS plane within a 3×3 cm^2 area.

For water, according to figure 6.4 (a), at thicknesses below 0.8 cm, electrons are scattered within 40^0 angle, within 1.4 to 2.5 cm they are scattered up to 80^0.

For carbon, according to figure 6.4 (b), at thicknesses below 0.4 cm, electrons are scattered within 40^0 angle, around 0.8 to 1.4 cm thickness they are deflected up to 80^0.

(a)

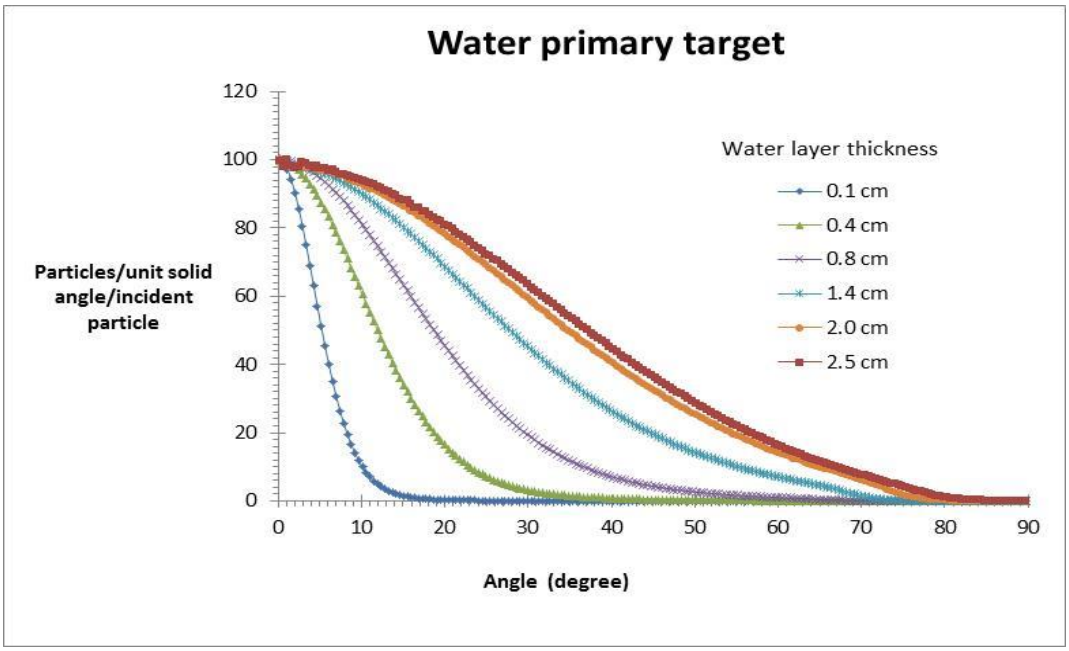

(b)

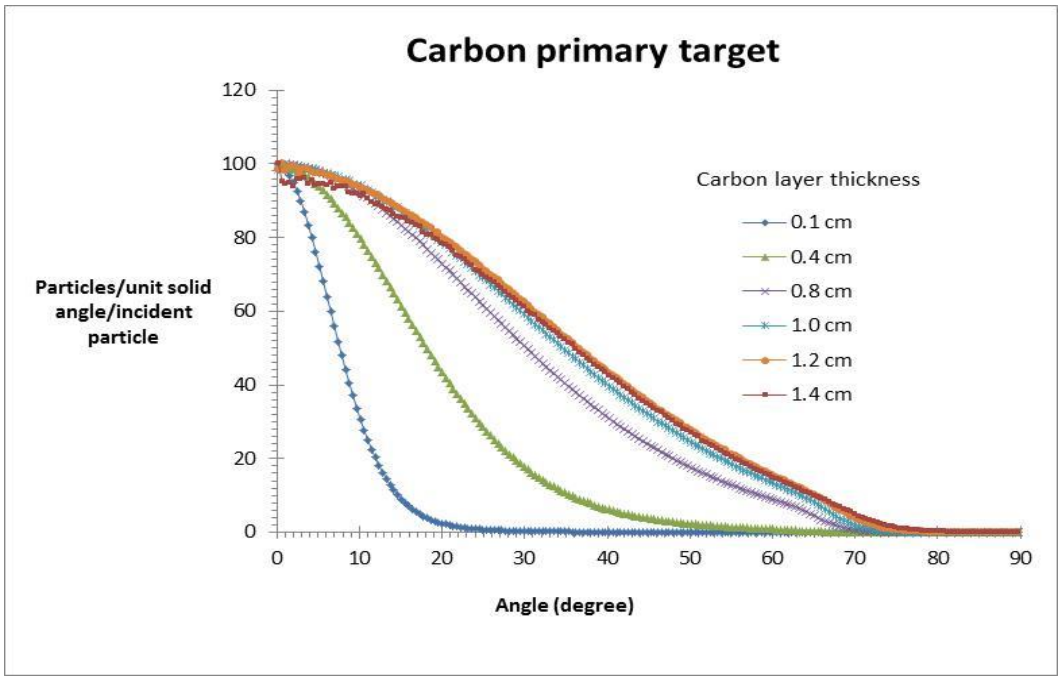

Figure 6.4: Electrons angular distribution for primary target material of either (a) water or (b) carbon layers, along the central axis of the incident electron pencil beam of 6 MeV.

6.3 Modelled Linac Head

Figure 6.5 shows a linac head modelled using BEAMnrc which consisted of a secondary target, primary collimator, MLCs and X,Y Jaws. The ionisation chamber and the mirror were not modelled because they play a negligible role in radiation attenuation hence were irrelevant for this study. It was important to model a flattening filter free machine since the filter can harden a softer x-ray beam. All dimensions of these components were explained in the previous chapter. PS files obtained from the primary target (moderator) simulations were used as the input source of electrons onto the secondary target (a) made of tungsten (W). Several simulations were run to get suitable primary/secondary target thicknesses between water/tungsten and carbon/tungsten layers. FFF linac results for the original Bremsstrahlung target were also included.

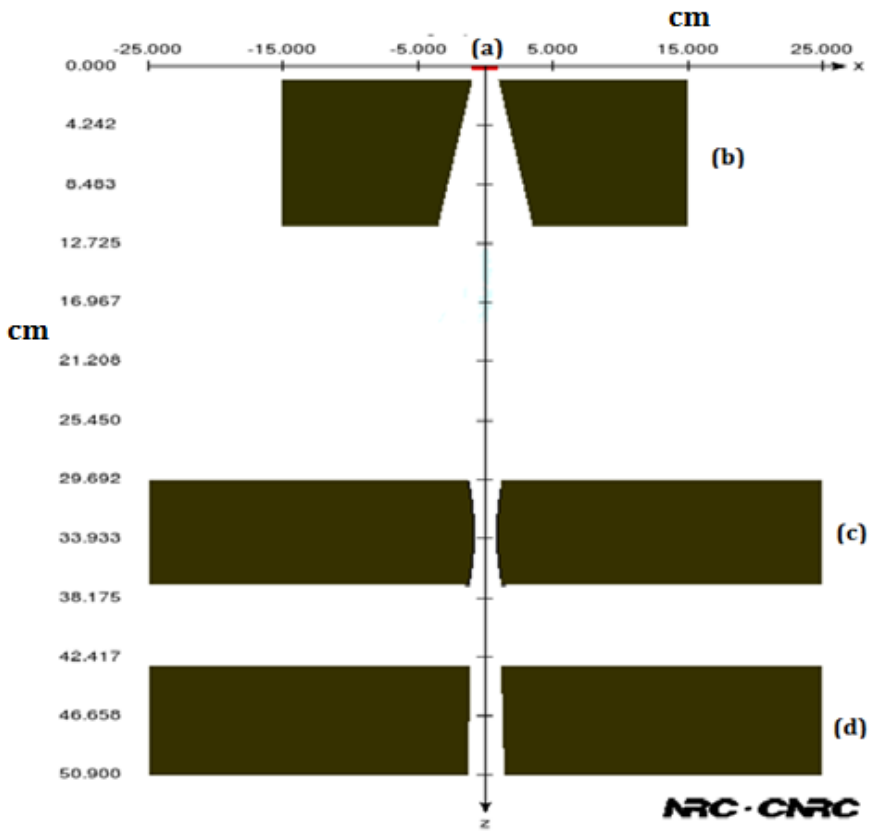

Figure 6.5: MC model for the Elekta Precise linac head simulated; (a) Secondary tungsten target, (b) Primary collimator, (c) MLCs and (d) X,Y Jaws.

6.3.1 X-ray Beam Mean Energy

Simulations were run using the MC linac model in figure 6.5. Different electron spectra from the primary target simulations in the previous sections were selected and used as input sources incident onto various secondary tungsten target layers based. For water and carbon, five electron spectra for 0.8, 1.4, 1.5, 2.0 and 2.5 cm target thickness were selected for investigation. The selection was based on the electron energy spectra produced.

For the secondary target, tungsten layers ranging between 0.07 cm and 0.19 cm were investigated. The selection of photon beams produced was based on obtaining beams with more low energy photons. Simulations were run using a 10 x 10 cm^2 field size to calculate x-ray mean energies from phase space data obtained below X,Y jaws.

Photon mean energies in tables 6.2 (a) and (b) and 6.3 (a) and (b) were calculated using the different energy electron beams that now strikes the secondary target at an SSD of 100 cm for a field size of 10 x 10 cm^2 along the beam central axis. The combinations are of water/tungsten and carbon/tungsten layers, where the secondary target is just tungsten and the primary is either water or carbon.

The mean energy of the photon beam, generated by 6 MeV electrons, from an original linac with tungsten target (0.3 cm) was also calculated for comparison and is denoted by “Unaltered” throughout the chapter. The calculated mean photon energy for the original linac was found to be 1.36 MV.

With the $3x10^8$ histories simulated for each case, the average statistical uncertainty was below 1%.

Table 6.2:

In the table the mean photon energies are shown for (a) two primary water targets that first slowed down the 6 MeV electron pencil beam to be used as sources in different tungsten targets to generate the ten photon beams.

(a) Mean photon energies (MeV) obtained after two water target electron spectra traverses through various tungsten layers:

	Tungsten (cm)				
Water (cm)	**0.07**	**0.10**	**0.13**	**0.16**	**0.19**
1.4	***0.743***	***0.805***	***0.864***	***0.877***	***0.906***
2.5	***0.427***	***0.460***	***0.483***	***0.502***	***0.521***

(b) Mean photon energies (MeV) obtained for various moderated water target electrons traversing a constant tungsten (0.13 cm) layer:

Water (cm)	**0.8**	**1.4**	**1.5**	**2.0**	**2.5**
Mean E (MeV)	***1.000***	***0.864***	***0.783***	***0.669***	***0.483***

According to table 6.2 (a), when the water layer thickness is kept constant and the tungsten layer thickness is changed, this will increase the Bremsstrahlung mean energy as the tungsten layer increases. The mean energy increases as the target thickness increases due to beam hardening because of filtration of the target itself.

According to table 6.2 (b), keeping tungsten constant (in this case, 0.13 cm) whilst increasing the water layer thickness the photon energy generated follows the trend for electron spectrum energies from primary target. The mean energy decreases until approximately 2.5 cm water thickness is attained. These lower mean energy electrons gives rise to lower energy Bremsstrahlung photons, but if the secondary tungsten target is too thick it may cause beam hardening and therefore an increase in the average exit energy of the photons.

Table 6.3:

(a) Mean photon energies (MV) obtained after two carbon target electron spectra traverses through various tungsten layers:

	Tungsten (cm)				
Carbon (cm)	**0.07**	**0.10**	**0.14**	**0.16**	**0.19**
0.8	***0.669***	***0.723***	***0.770***	***0.791***	***0.815***
1.4	***0.368***	***0.395***	***0.428***	***0.441***	***0.457***

(b) Mean photon energies obtained after various carbon target electron spectra traverses through a constant tungsten (0.14 cm) layer:

Carbon (cm)	**0.5**	**0.8**	**1.0**	**1.2**	**1.4**
Mean E (MeV)	***0.960***	***0.770***	***0.611***	***0.529***	***0.428***

According to table 6.3 (a) when the carbon layer is kept constant whilst increasing the tungsten layer thickness this will increase the mean photon energy.

According to table 6.3 (b) , keeping tungsten constant whilst increasing the carbon layer thickness, the mean photon energy decreases until a value of approximately 1.4 cm thickness is attained.

Comparing calculated values to the original linac beam energy which had a mean photon energy of value of 1.38 MV; all calculated energies using the modelled electron beams were lower since the primary water or carbon layers act as moderators that slows down the original 6 MeV electrons before striking the secondary tungsten target.

6.3.2 X-ray Beam Energy Spectra

Figures 6.6-6.9 show the photon spectra calculated from PS files obtained at a plane just below the X,Y jaws for the modelled beams from the FFF Elekta linac head. These beams were generated using electron spectra obtained from the primary target simulations for radiation field sizes of 5 x 5 cm^2, 10 x 10 cm^2 and 20 x 20 cm^2. They were calculated for water/tungsten and carbon/tungsten target combinations. The spectra were normalized to 100 percent and were calculated over 200 bins.

Dose enhancement in tumours doped with NPs relies on the photoelectric effect due to production of additional electrons. The photoelectric effect is proportional to the fourth-to-fifth power of the atomic number of the absorber hence target combinations that generated photons of approximately 0.5 MV mean energy which suits gold (79) NPs were selected for further investigation.

Therefore a water/tungsten target combination, of 2.5 cm water combined with various tungsten thicknesses were used to generate photon beams. Tungsten was then kept constant at 0.13 cm and also combined with various water thicknesses for investigating effects of changing electron spectra on the generated photon beams.

The above process was repeated for carbon/tungsten target combinations. This time 1.4 cm carbon combined with various tungsten thicknesses were investigated. Tungsten was then kept constant at 0.14 cm and combined with various carbon thicknesses for the other set of photon beams.

6.3.2.1 Photon Energy Spectra for Water/Tungsten Bremsstrahlung Target Combinations

In the next set of graphs, the Bremsstrahlung energy spectra for the electrons transmitted through the 2.5 cm thickness primary water target is calculated from PS files just below the exit plane of the linear accelerator for field ranging between 5 x 5 cm^2 and 20 x 20 cm^2. For comparison, the original 6 MV Bremsstrahlung spectrum is also shown. In this case different tungsten layers for the secondary target were used to examine the effect on the transmitted Bremsstrahlung photons.

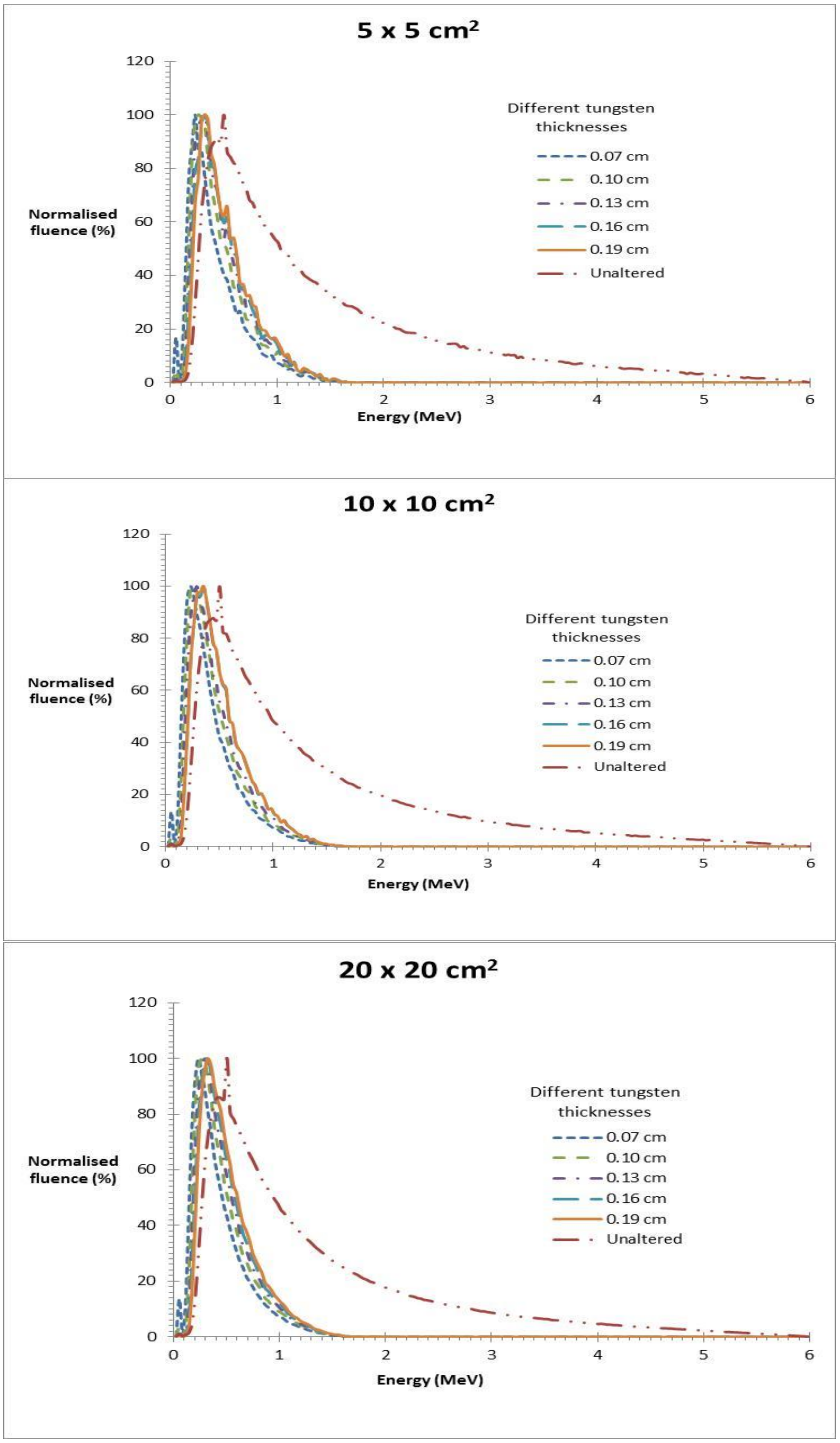

Figure 6.6: Normalised photon energy spectra from beams of an electron spectrum for a water layer target thickness (2.5 cm) combined with different tungsten layers for the shown range of field sizes.

The next set of graphs shows the energy spectra obtained from different water thicknesses

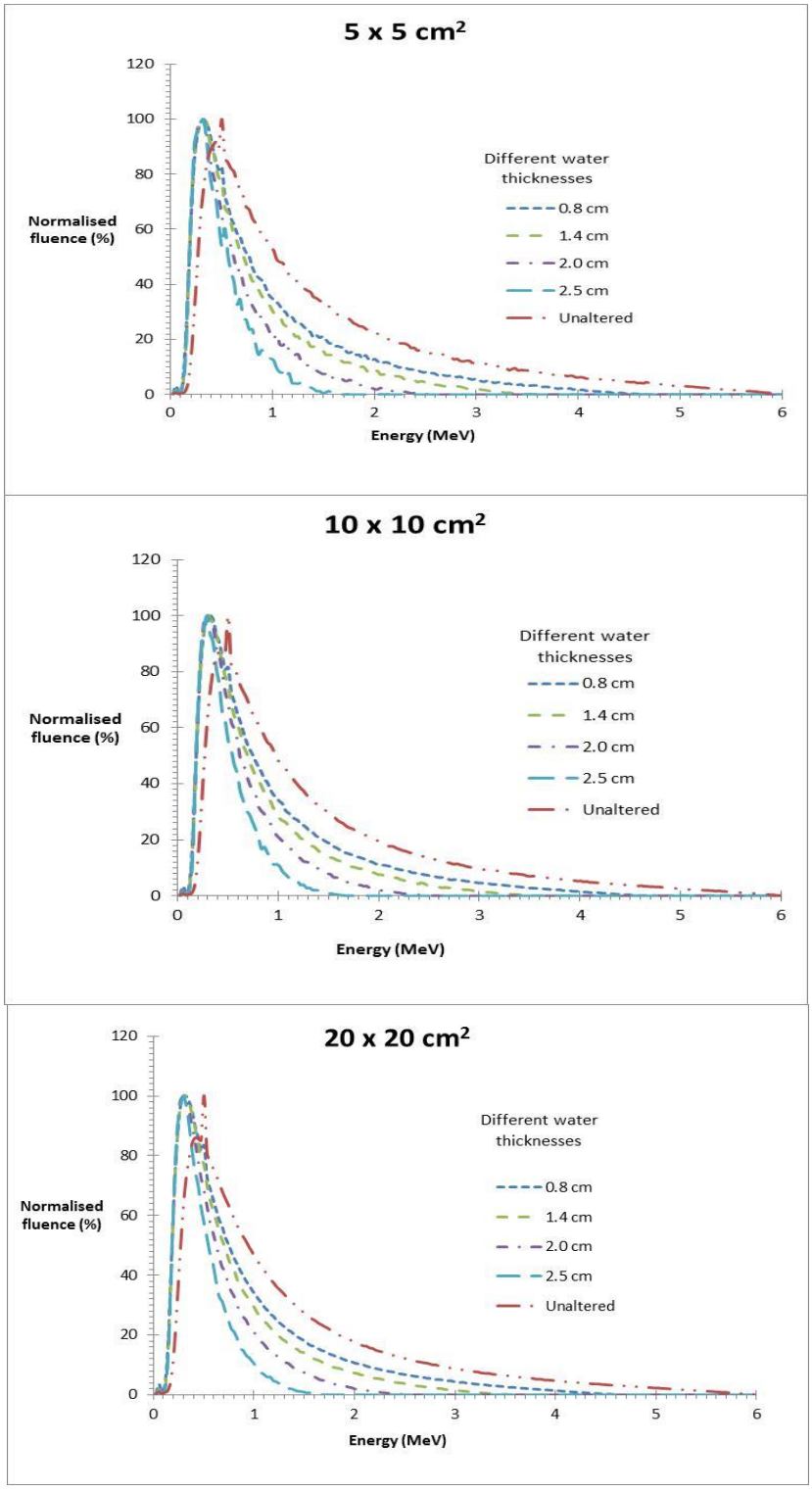

Figure 6.7: Normalised photon energy spectra from beams of various electron spectra for water layers combined with a constant tungsten (0.13 cm) layer for the shown range of field sizes.

The set of graphs in figure 6.7 shows the Bremsstrahlung energy spectra for the electrons transmitted through different thicknesses of the primary water target is calculated from PS files just below the exit plane of the linear accelerator for field ranging between 5 x 5 cm^2 and 20 x 20 cm^2. For comparison, the original 6 MV Bremsstrahlung spectrum is also shown. In this case the secondary tungsten target was fixed at 0.13 cm thickness.

6.3.2.2 Extracted Photon Energy Spectral from Carbon/Tungsten Bremsstrahlung Target Combinations

In figure 6.8 the effect of secondary tungsten target thickness is studied when a 1.4 cm thick primary carbon target is used to slow down the 6 MeV photons emerging from the waveguide.

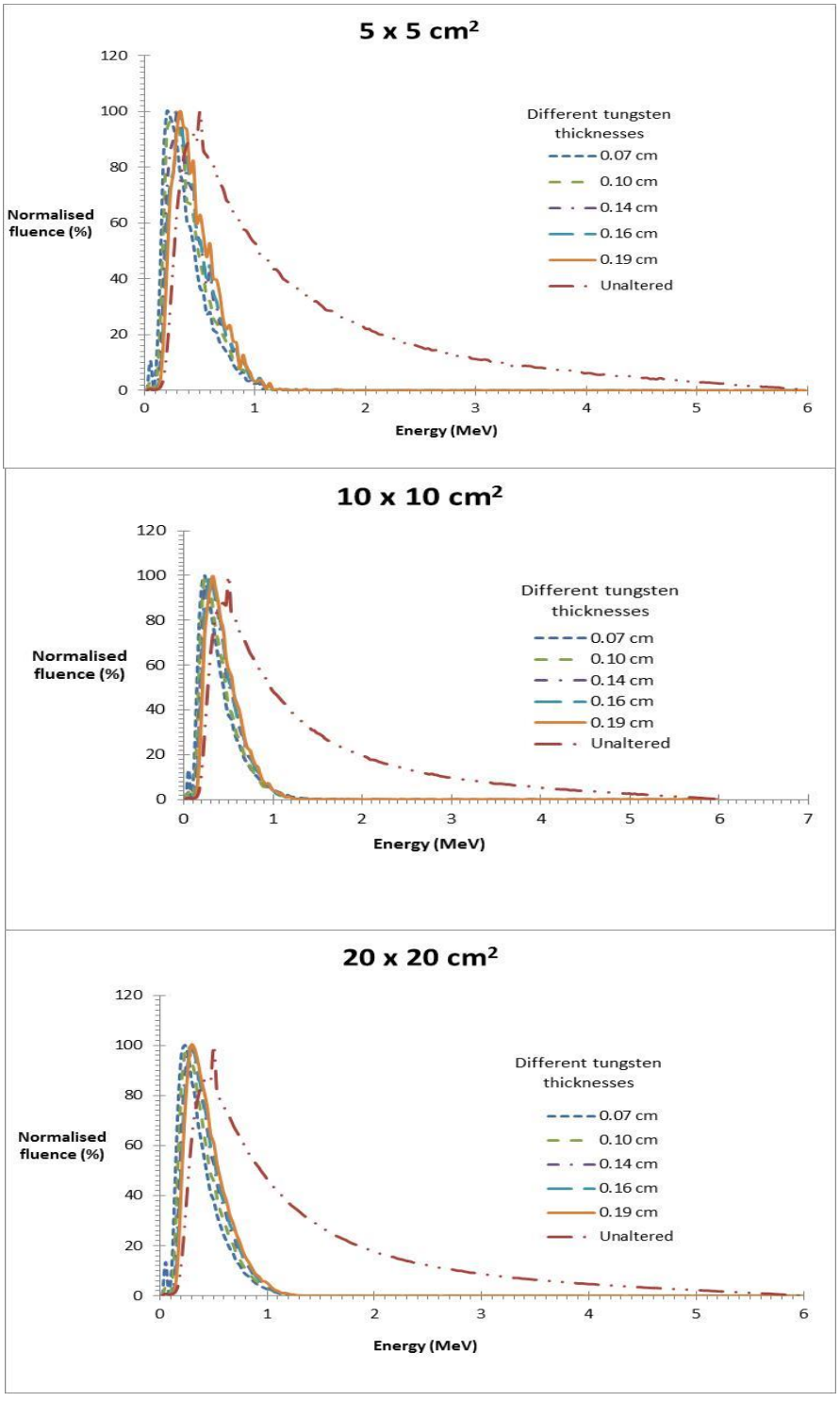

Figure 6.8: Normalised photon energy spectra from beams with an electron spectrum obtained for a carbon layer target thickness (1.4 cm) combined with different tungsten layers for the shown range of field sizes.

In figure 6.9 two cases of different carbon layers for the primary target are shown with a constant 0.14 cm thickness of tungsten.

According to figures 6.6 and 6.8 changing the tungsten thickness and either keeping water or carbon layers constant does not show a strong change in energy spectra. Photon energy spectra depend strongly on the change of the thickness of carbon and water layers as shown in figure 6.7 and 6.9. Modelled altered electron energies generated maximum photon energies of significantly lower than 6 MV demonstrating slowing down of electrons in the primary target of either water or carbon.

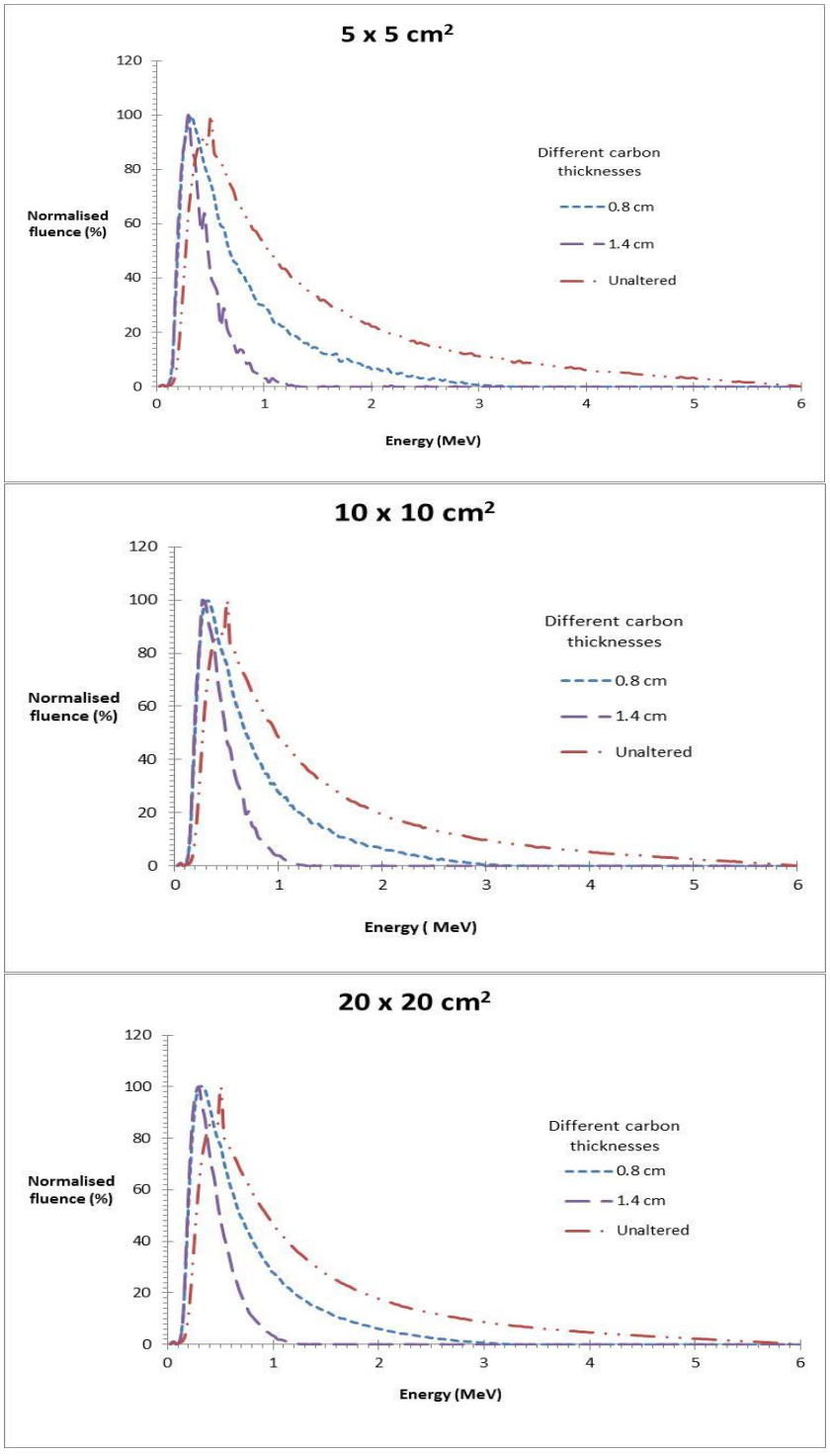

Figure 6.9: Normalised photon energy spectra from beams of various electron spectra for two carbon layers combined with a constant tungsten (0.14 cm) layer for the shown range of field sizes.

6.3.3 Off-axis Mean Energy Distribution

Figures 6.10 (a – e) show the off-axis photon beam mean energy calculated at different off-axis annuli from PS files collected at a plane just below the X,Y jaws of the linac. The mean energy distributions correspond to the target combinations from section 6.3.2. The mean energies were determined from a circular field with 10 annuli of 1 cm width. Simulations were carried using a 20 x 20 cm^2 field size.

From figures 6.10 (a) to (e) it is evident that the mean energy is almost uniform across the beam within the 7 cm radius from the central axis. Beyond 7 cm, the average energy decreases. It is observed that the mean energy values have relatively high standard deviation at the edge of the beam when compared to mean energy values towards the central axis of the beam. The observation can be attributed to the sparse amount of photons at the field edge which increases the variance on the data. There are a greater number of low energy photons and a small number of high energy photons such that the difference when calculating the standard deviation is high.

(a)

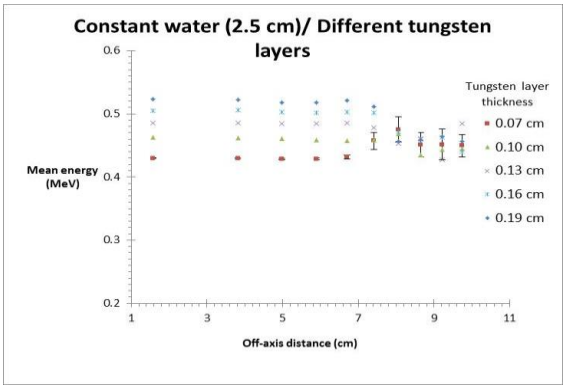

(b)

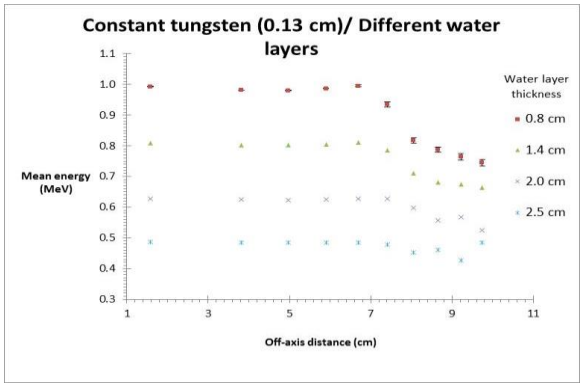

(c)

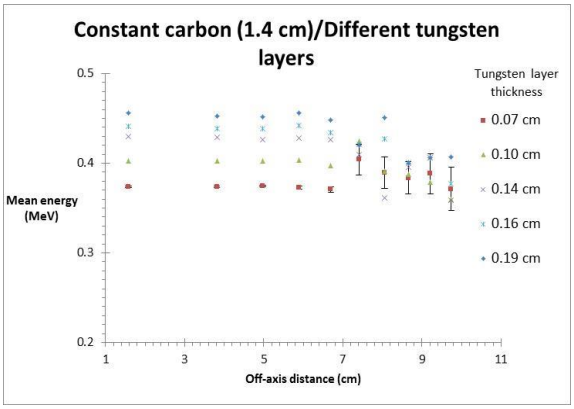

(d)

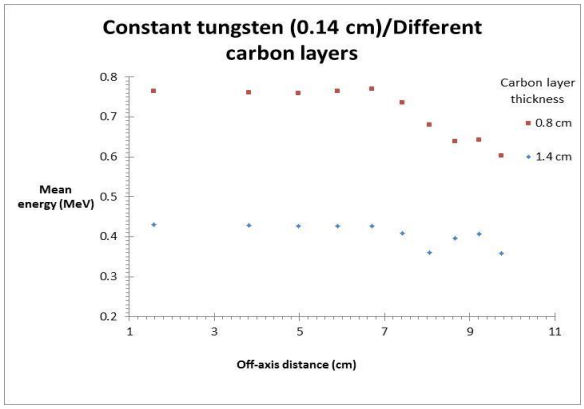

(e)

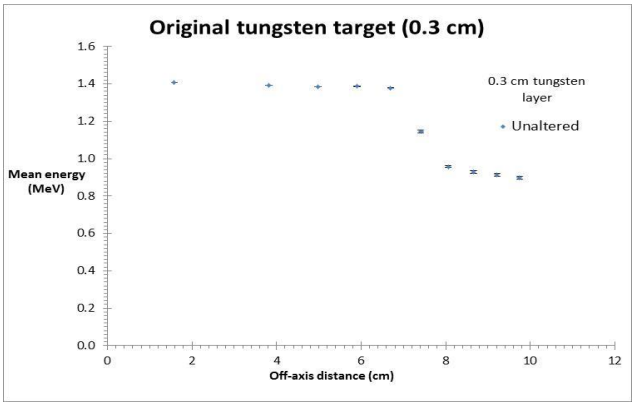

Figure 6.10: Off-axis photon beam mean energy distribution for various thicknesses Bremsstrahlung target combinations; (a) Constant water (2.5cm)/ different tungsten, (b) Constant tungsten (0.13 cm)/ different water, (c) Constant carbon (1.4 cm)/different tungsten, (d) Constant tungsten (0.14 cm)/ different carbon and (e) Original tungsten target (0.3 cm) with 6 MeV electron beam.

6.4 Water Phantom Simulation

6.4.1 Percentage Depth Doses

The penetration properties of the photon beams with energy spectra as studied from the previous chapter were investigated using DOSXYZnrc. Graphs extracted in this chapter are from DOSXYZnrc generated 3ddose files and normalized to their own maximum. They were extracted using a MCSHOW package.

Figures 6.11-6.14 show the calculated depth dose curves from various Bremsstrahlung target combinations. Beams were simulated at field sizes of 5 x 5 cm^2, 10 x 10 cm^2 and 20 x 20 cm^2 in a water phantom. Results of a 6 MV FFF Elekta precise linac beam were included for comparison denoted by "unaltered". The calculated depth-dose distributions were prepared specifically for MC modelled beams characterization, corresponding to Bremsstrahlung target combinations in section 6.2.

According to figure 6.11 and 6.13 it is evident that by keeping the thickness of water or carbon layer constant and changing the tungsten target thickness, the depth of maximum dose (dmax) as well as the percentage surface dose remains almost the same. The energy of the incident photon beam is the predominant factor in determining the penetration of the beams in water, as expected. Thus keeping water or carbon constant gives almost the same lowest beam quality, with a PDD (10 cm) of approximately 50% compared to beams obtained from an unaltered linac target, PDD (10 cm) of 64% for a 10 x 10 cm^2 field as shown in figures 6.10 and 6.12.

6.4.1.1 PDDs for Water/Tungsten Bremsstrahlung Target Combinations

Figures 6.11 and 6.12 present the simulated central axis PDD curves at the photon beams obtained using water/tungsten target combinations at various field sizes indicated in a virtual water phantom.

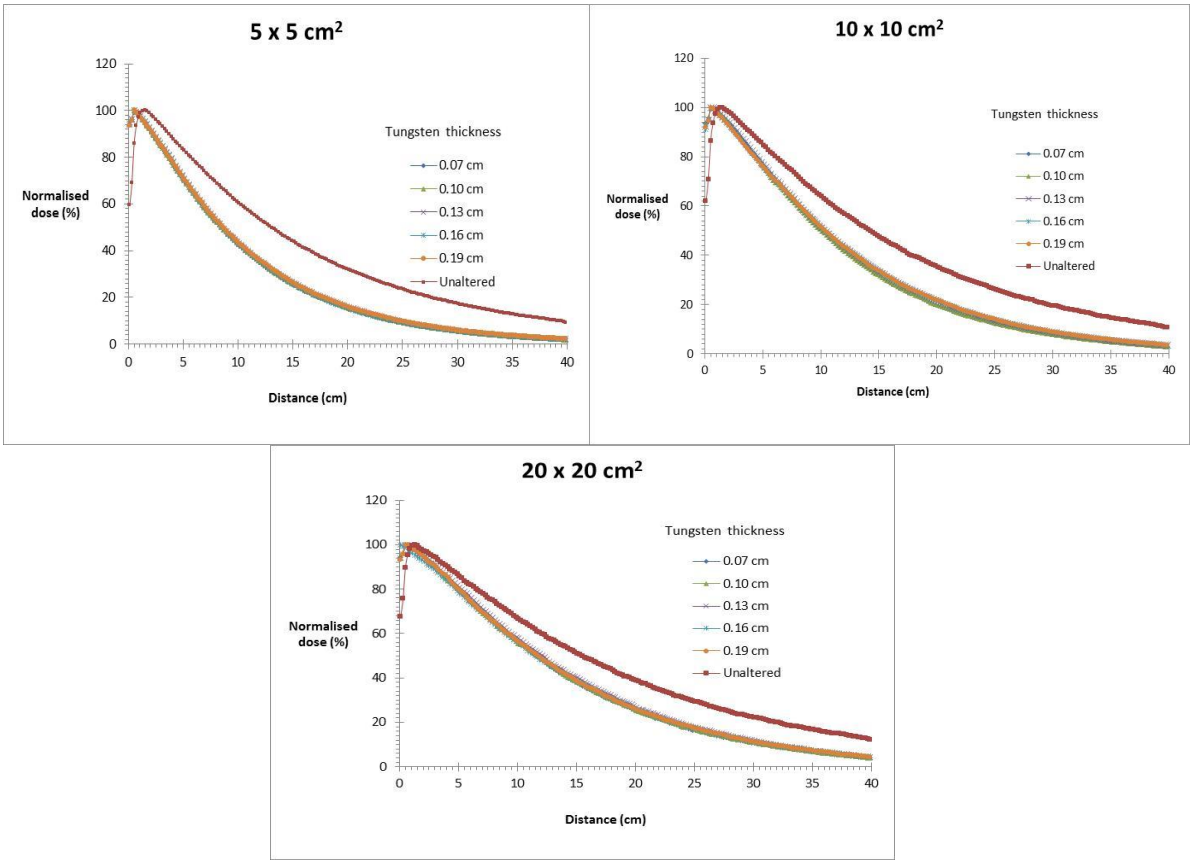

Figure 6.11: Normalised percentage depth dose from photon beams generated with an electron spectrum for a primary water layer target thickness (2.5 cm) combined with different secondary target tungsten layers for the indicated field sizes.

The following set of graphs represent normalised percentage depth dose from photon beams for primary target water layers combined with a constant secondary tungsten (0.13 cm) layer thickness.

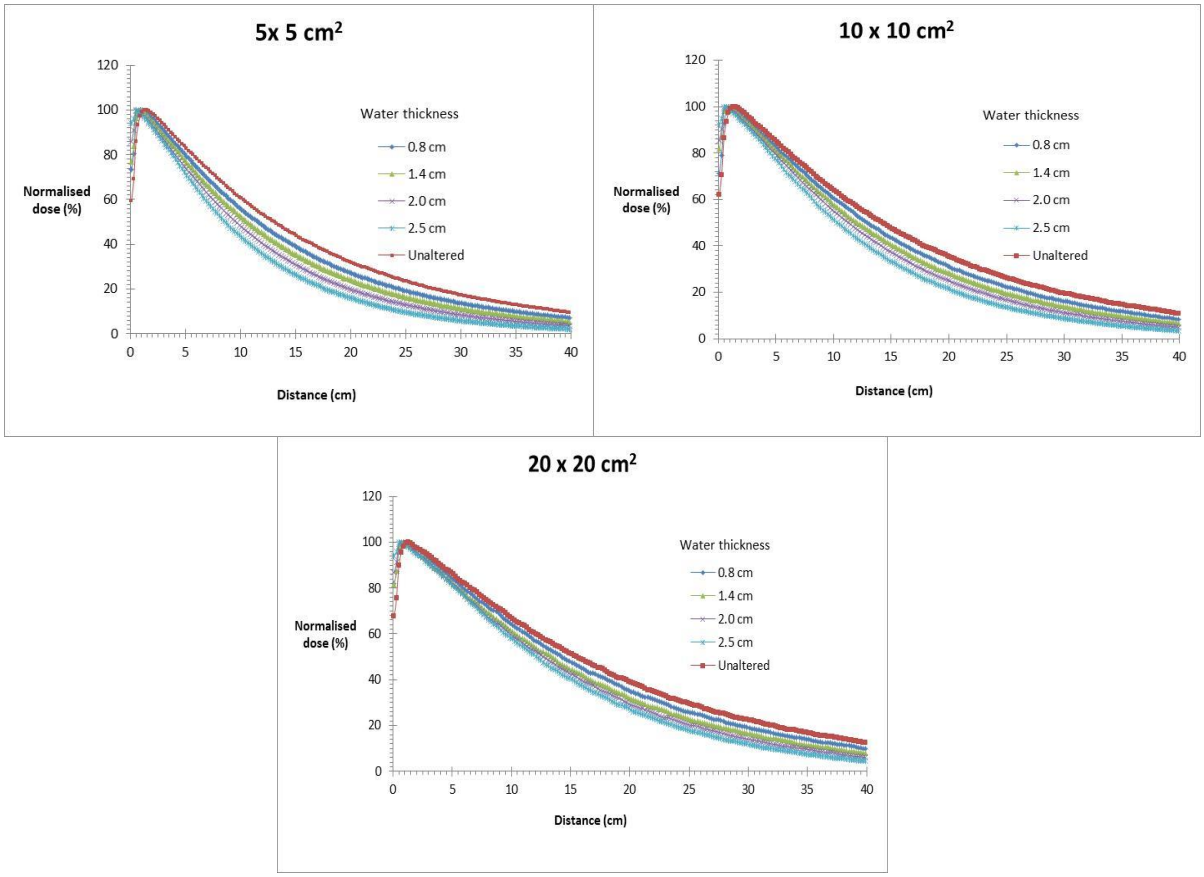

Figure 6.12: Normalised percentage depth dose from photon beams for primary target water layers combined with a constant secondary tungsten (0.13 cm) layer at the indicated field sizes.

According to figure 6.12 and 6.14 when the tungsten target thickness is kept constant whilst water or carbon thickness is changing, depths of maximum dose as well as the percentage surface doses changes with change in thickness. The penetration ability relied much on the beams energy and the primary target thickness. Various PDDs (10 cm) of between 40% and 60% were obtained for a 10 x 10 cm^2 field size.

6.4.1.2 PDDs for Carbon/Tungsten Bremsstrahlung Target Combinations

The following figures 6.13 and 6.14 present the simulated central axis PDD curves at the photon beams obtained using carbon/tungsten target combinations at various field sizes in a water phantom.

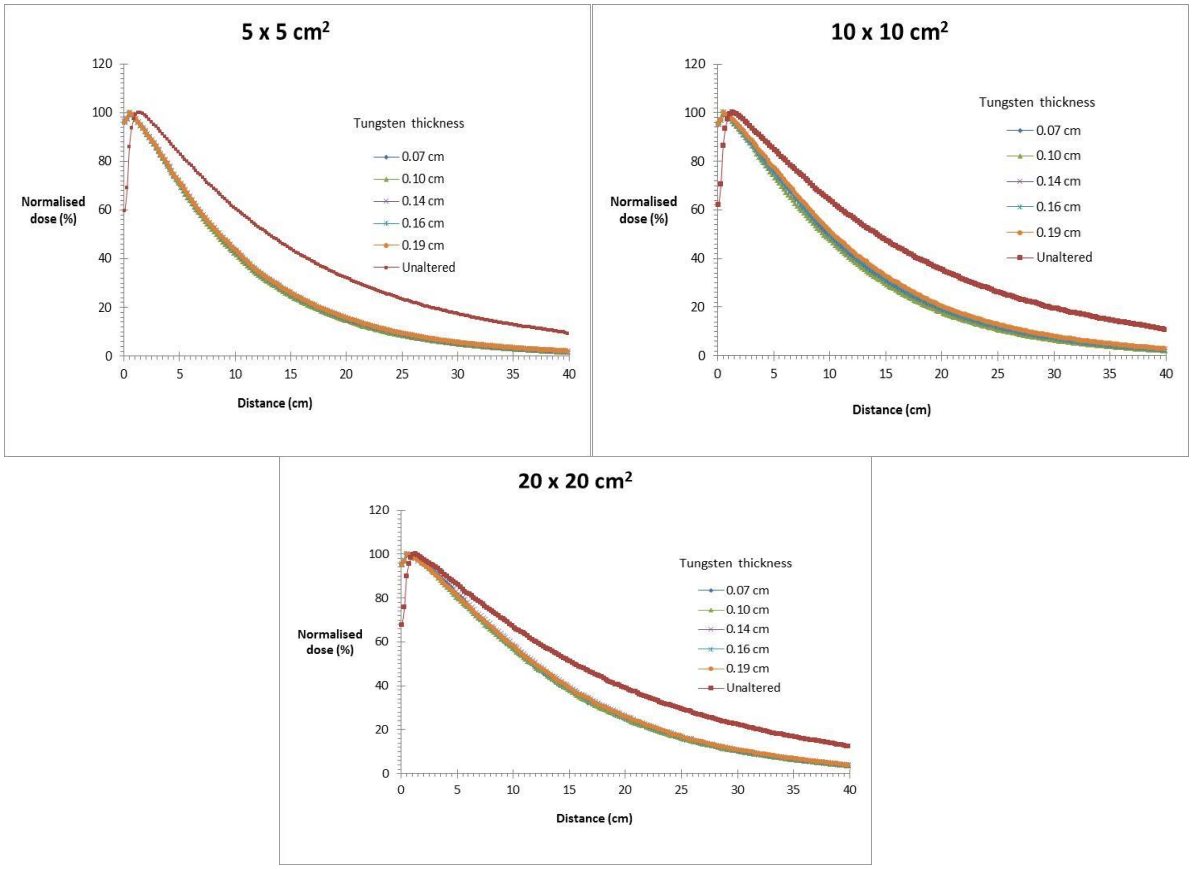

Figure 6.13: Normalised percentage depth dose from photon beams for a carbon layer target thickness (1.4 cm) combined with different tungsten layers at the indicated field sizes.

A set of PDDs below on figure 6.14 shows a significant difference in PDDs for different thicknesses of carbon which implies that there is a high dependence of PDDs on the thickness of carbon layer when tungsten is kept constant.

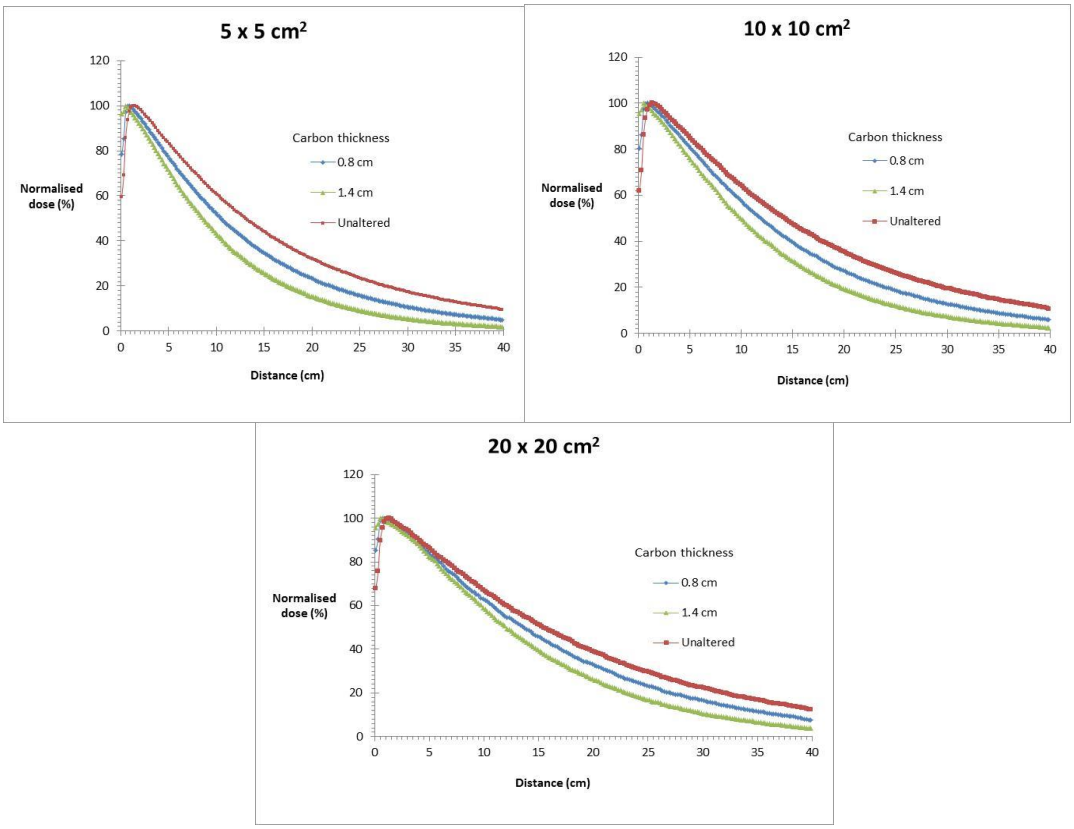

Figure 6.14: Normalised percentage depth dose from photon beams for carbon layers combined with a constant tungsten (0.14 cm) layer at the indicated field sizes.

6.4.2 Planar Dose Profiles

Figures 6.15 – 6.18 show a set of dose profiles extracted from a DOSXYZnrc water phantom which was a follow up from plotted PDDs for the same target combinations. Dose distributions were calculated using the PS files obtained from modelled beams from water/tungsten and carbon/tungsten Bremsstrahlung target combinations. The profiles data were obtained at 10 cm depth, for field sizes of 5 x 5 cm^2, 10 x 10 cm^2 and 20 x 20 cm^2 defined at 100 cm SSD. All

profiles were normalized on the central axis (CAX). Original 6 MV beam results are included for comparison. The graphs were extracted using the MCSHOW package. The Bremsstrahlung target combinations correspond to the ones in chapter 6.3.1. The statistical variance in the MC simulations was kept below 1%**.**

6.4.2.1 Planar Dose Profiles for Water/Tungsten Bremsstrahlung Target Combinations

Figures 6.15 and 6.16 (a – c) present the simulated DPs for indicated field sizes at the x-ray photon beams obtained using water/tungsten target combinations at 10 cm depth in a virtual water phantom.

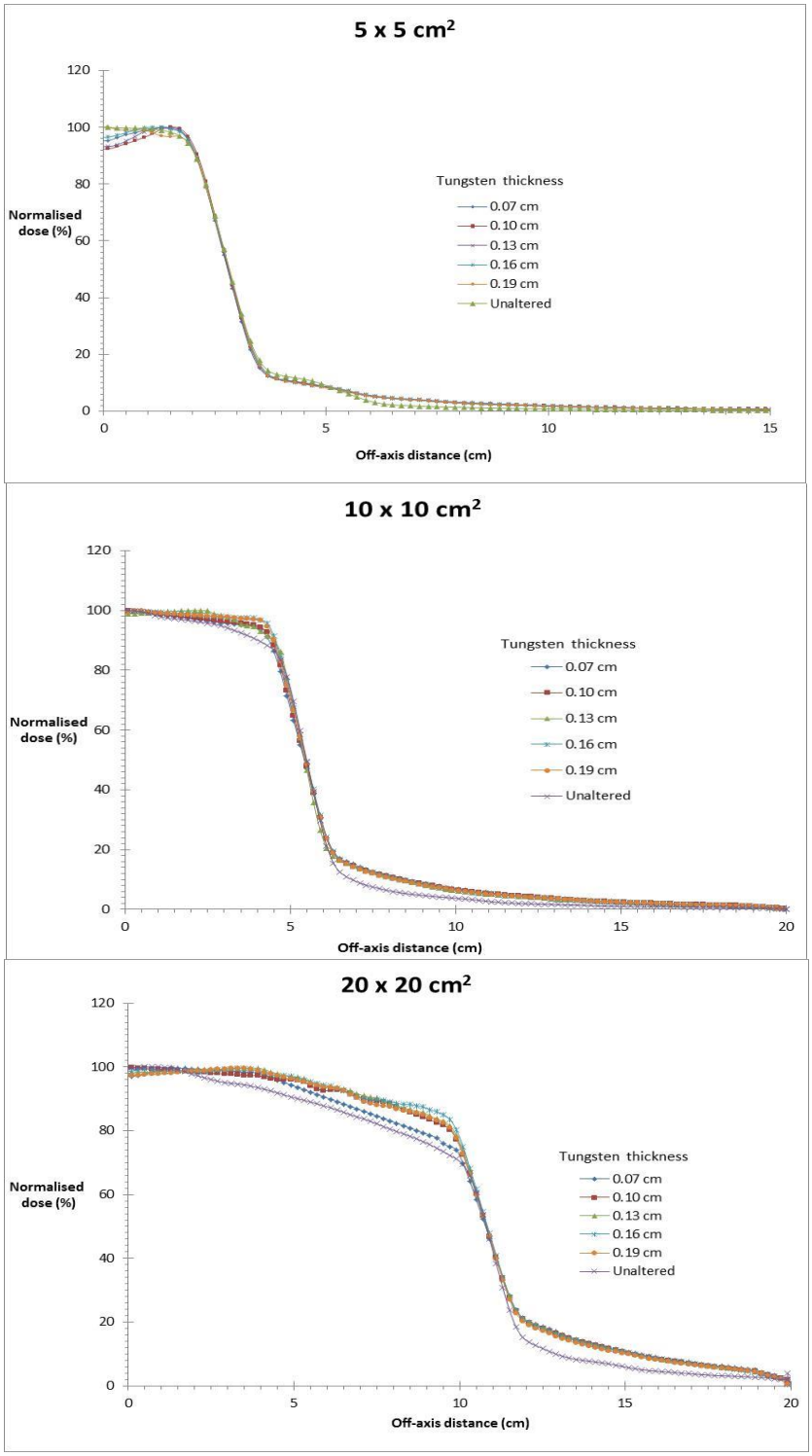

Figure 6.15: : Normalised photon dose profiles at 10 cm depth in water for a range of field sizes obtained from beams of a constant water layer (2.5 cm) combined with various tungsten layers for the following fields: (a) 5 x 5 cm^2, (b) 10 x 10 cm^2 and (c) 20 x 20 cm^2 .

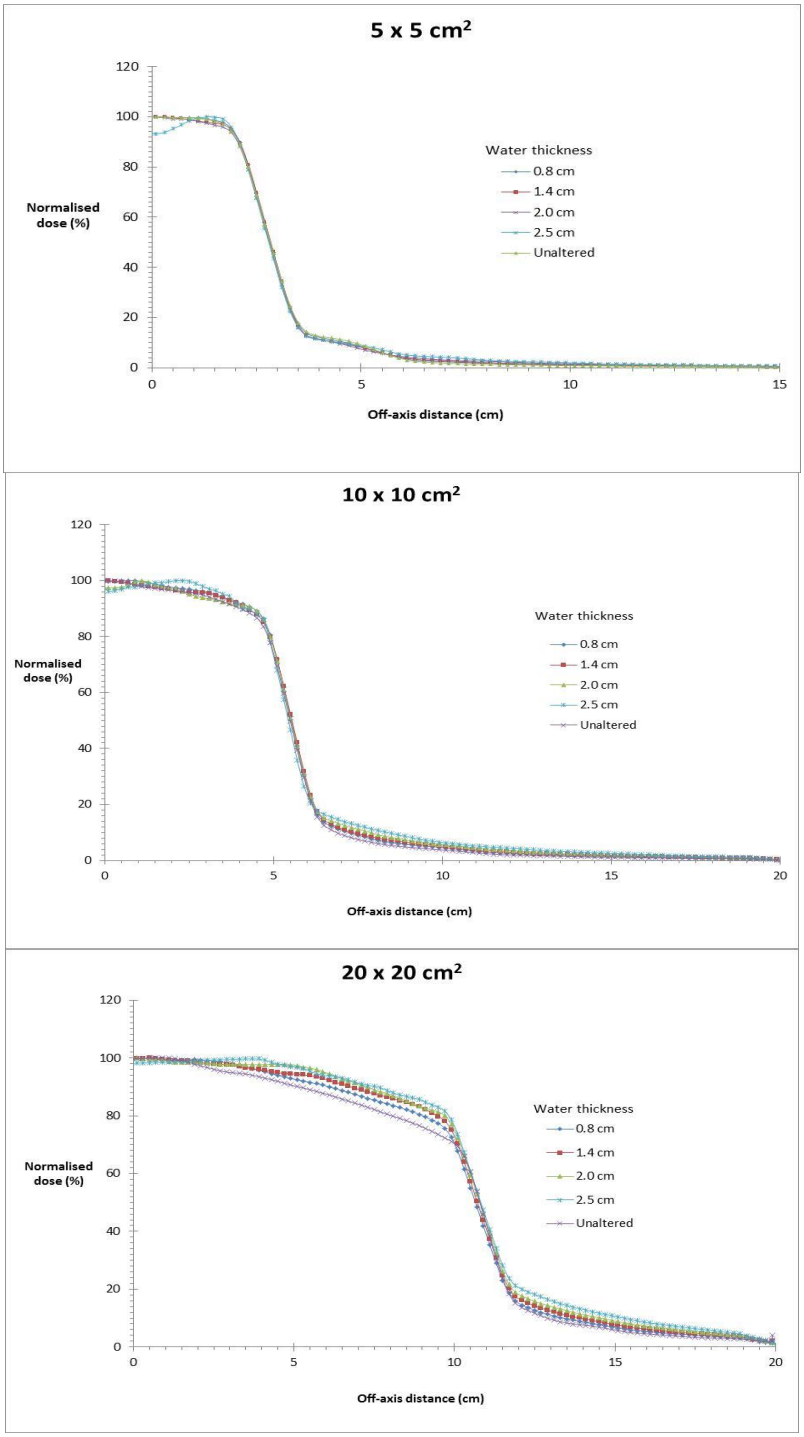

Figure 6.16: Normalised photon dose profiles at 10 cm depth in water for a range of field sizes obtained from beams of a constant tungsten layer (0.13 cm) combine with various water layer thicknesses for: 5 x 5 cm^2, 10 x 10 cm^2, and 20 x 20 cm^2 field size.

6.4.2.2 Planar Dose Profiles for Carbon/Tungsten Bremsstrahlung Target Combinations

Figures 6.17 and 6.18 present the simulated DPs for indicated field sizes at x-ray photon beams obtained using carbon/tungsten target combinations at 10 cm depth in a virtual water phantom.

According to figures 6.15 to 6.18 the width of the geometric penumbra depends on the source size. Outside the geometry limits of the beam, the dose variation is the result of side scatter from field as well as leakage and scatter from the collimator system.

In all cases the dose at periphery of the field was greater for the lower energy photon beams compared to the original beam. The scattering is more for these lower energy photon beams compared to the original 6 MV beam. Also the absence of a flattening filter will cause the higher energy beams to be more peaked in intensity along the CAX leading to a relative less dose at the field edge regions, when compared to lower energy beams. The different field sizes as presented on figure 6.15 to 6.18 that were shaped by the MLC and back-up jaws. These beams were used to investigate photon radiation dose enhancement in NPs seeded tumours using a constructed patient CT phantom.

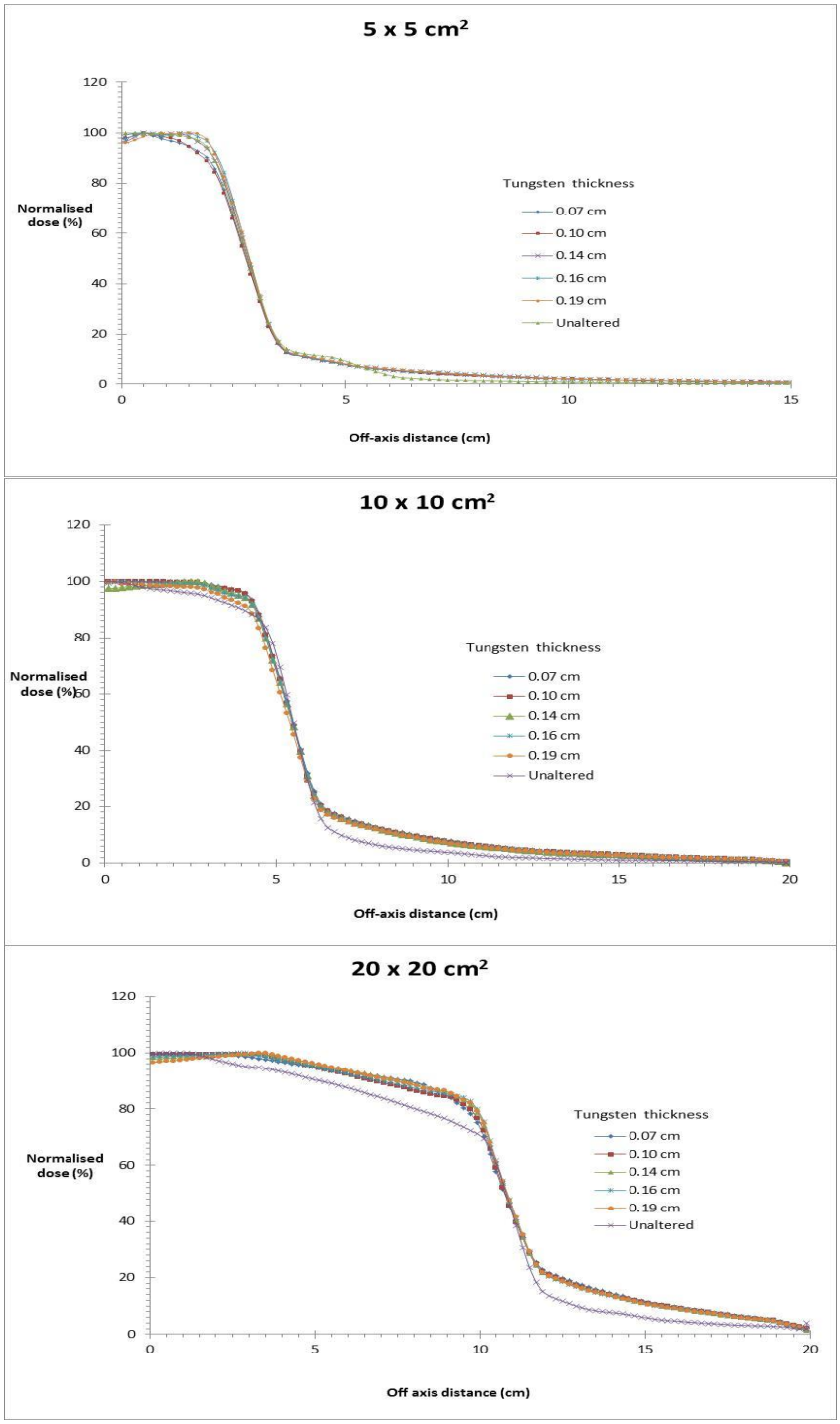

Figure 6.17: : Normalised photon dose profiles at 10 cm depth in water for a range of field sizes obtained from beams of a constant carbon layer (1.4 cm) combine with various tungsten layers for fields of: 5 x 5 cm^2, 10 x 10 cm^2 and 20 x 20 cm^2 field size.

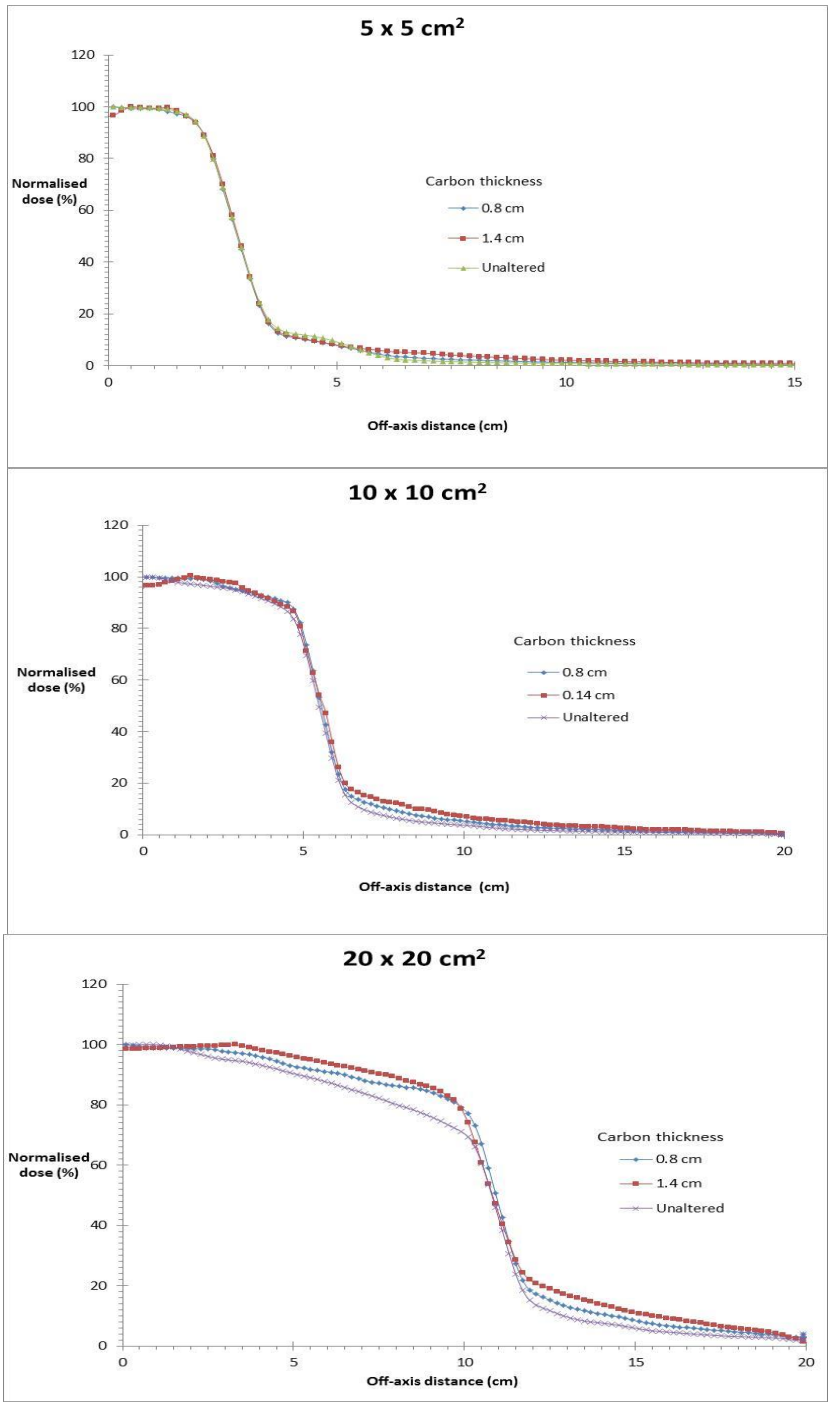

Figure 6.18: Normalised photon dose profiles at 10 cm depth in water for a range of field sizes obtained from beams of a constant tungsten layer (0.14 cm) combine with two carbon thicknesses for the fields of: 5 x 5 cm^2, 10 x 10 cm^2, and 20 x 20 cm^2 field size.

6.5 Constructed Patient CT Phantom Simulations

The treatment planning strategy in this study was based on the ICRU 50 guideline by Landberg *et al.* that stipulates that an optimal treatment plan is one wherein the whole PTV receives between 95% and 107% of the prescription dose. The following results presents percentage planar dose profiles obtained using a constructed patient CT phantom in the x-axis direction along the isocentre to determine NP dose enhancement.

The PTV was the prostate and all beams used were equally weighted. The beams' isocentre were positioned at the centre of the PTV. The x, y and z coordinates of the isocentre were 0.56, 1.19 and -3.9 respectively. Three planning strategies were simulated namely, 4, 5 and 6 field plans, based on 3DCRT to compare NPs dose enhancement using various Bremsstrahlung target combinations. All the beams were conformed to the shape of the the tumour using MLCs with the aid of XiO treatment planning system as explained in the previous chapter.

Dose distributions were calculated for all beams obtained from Bremsstrahlung target combinations of water/tungsten, carbon/tungsten and original bremstrahlung linac tungsten target of 0.3 cm, using tumour with and without nanoparticles as explained in chapter 5.

The concentration of gold-nanoparticles (AuNPs) of 7mg/1000mg in the tumour was kept constant in this study. On all the graphs "Au/Tumour mix" is a composition mixture of the tumour and AuNPs and "Tumour only" is a tumour composition only. Based on average PTV dose, DEFs were calculated along the x-axis. The PTV dose to calculate DEFs was extracted from 3ddose data as generated by DOSXYZnrc. Dose profiles were sampled along a yellow line drawn over the corresponding CT data. This line passes through the isocentre for all the three treatment strategies used, namely 4F, 5F and 6F plans. All the DPs in the following sections were normalized to the maximum dose value along the isocentre in tumour without NPs.

6.5.1 Four Field Plan Simulations

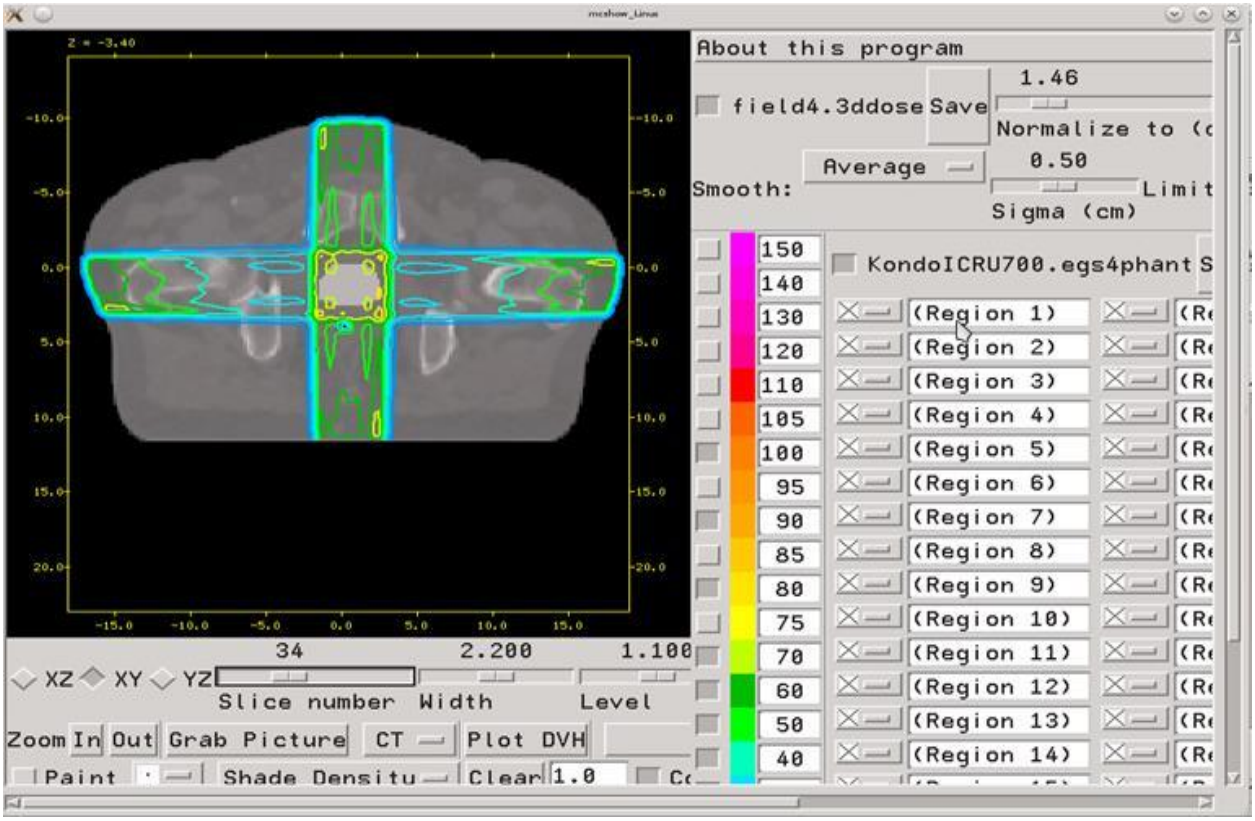

Figure 6.19: MCSHOW GUI showing the isodose curves through isocentre for a 4F box plan for modelled photon beams, obtained from DOSXYZnrc simulations of a patient CT phantom. The PTV is shown in grey inside the intersection of the four beams.

Figure 6.19 shows the isodose distribution simulated for a 4F box plan with 2 lateral beams passing through the right and left pelvis and the other two beams which are anterior-posterior (AP) and posterior-anterior (PA) beams. The isodose lines shown represent percentage dose since all the dose is normalised to the global maximum value.

Figure 6.20 shows the percentage dose profiles (DPs) for a 4F box plan obtained at the isocentre for water/tungsten Bremsstrahlung target beams. It is evident that dose enhancement can be obtained by changing the thickness of water target and keeping tungsten target constant.

As water thickness increases according to table 6.4, the dose enhancement also increase until a certain maximum thickness is reached. It can be noted that dose enhancement is quite visible at 2.5 cm water target and less visible at smaller thickness of 0.8 cm. In this case the tungsten layer thickness was kept constant at 0.13 cm.

6.5.1.1 Dose Distributions for Water/Tungsten Bremsstrahlung Target Combinations

In this section the influence of the number of fields in a radiation treatment plans on the resulting DEF is examined along the x-axis for various beams.

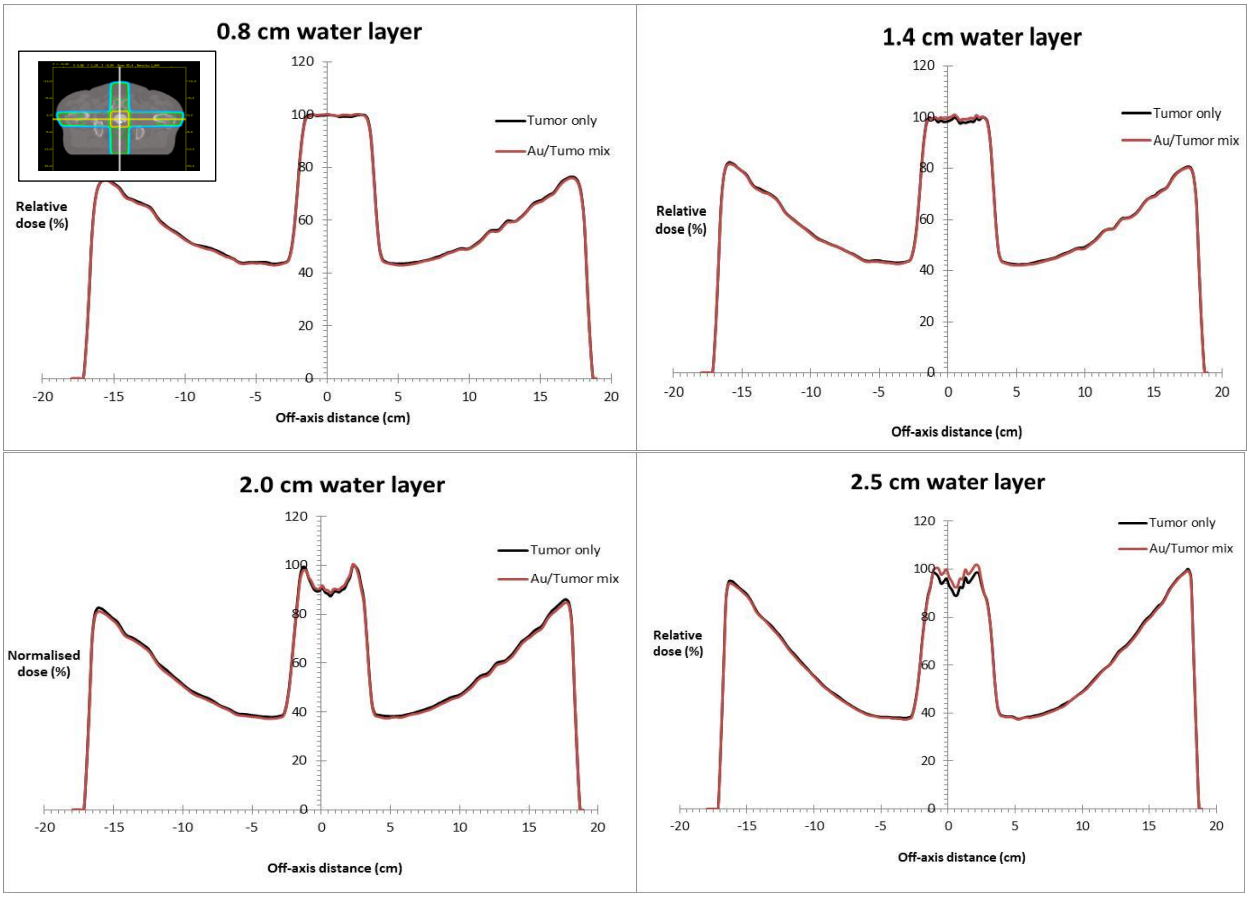

Figure 6:20: DPs along the x-axis for a 4F box plan using CT phantom with and without NPs in the PTV for beams obtained from Bremsstrahlung target combinations of a constant tungsten layer (0.13 cm) and various water layers.

In the above set of graphs on figure 6.20, beams from various thicknesses of primary target of water were investigated.

Table 6.4: Average DEFs for various water layers and a constant tungsten layer beams. The uncertainty in the data is 1.5%.

	Water layer (cm)			
	0.8	**1.4**	**2.0**	**2.5**
Average photon energy (MV)	**1.000**	**0.864**	**0.669**	**0.483**
DEF	**1.005 ± 0.015**	**1.011 ± 0.015**	**1.017 ± 0.015**	**1.040 ± 0.015**

The next set of graphs on figure 6.21 show DPs for a 4F plan obtained using photon beams from water/tungsten X-ray source target combination. Water thickness was kept constant at 2.5 cm and tungsten was varied between 0.07 cm to 0.19 cm.

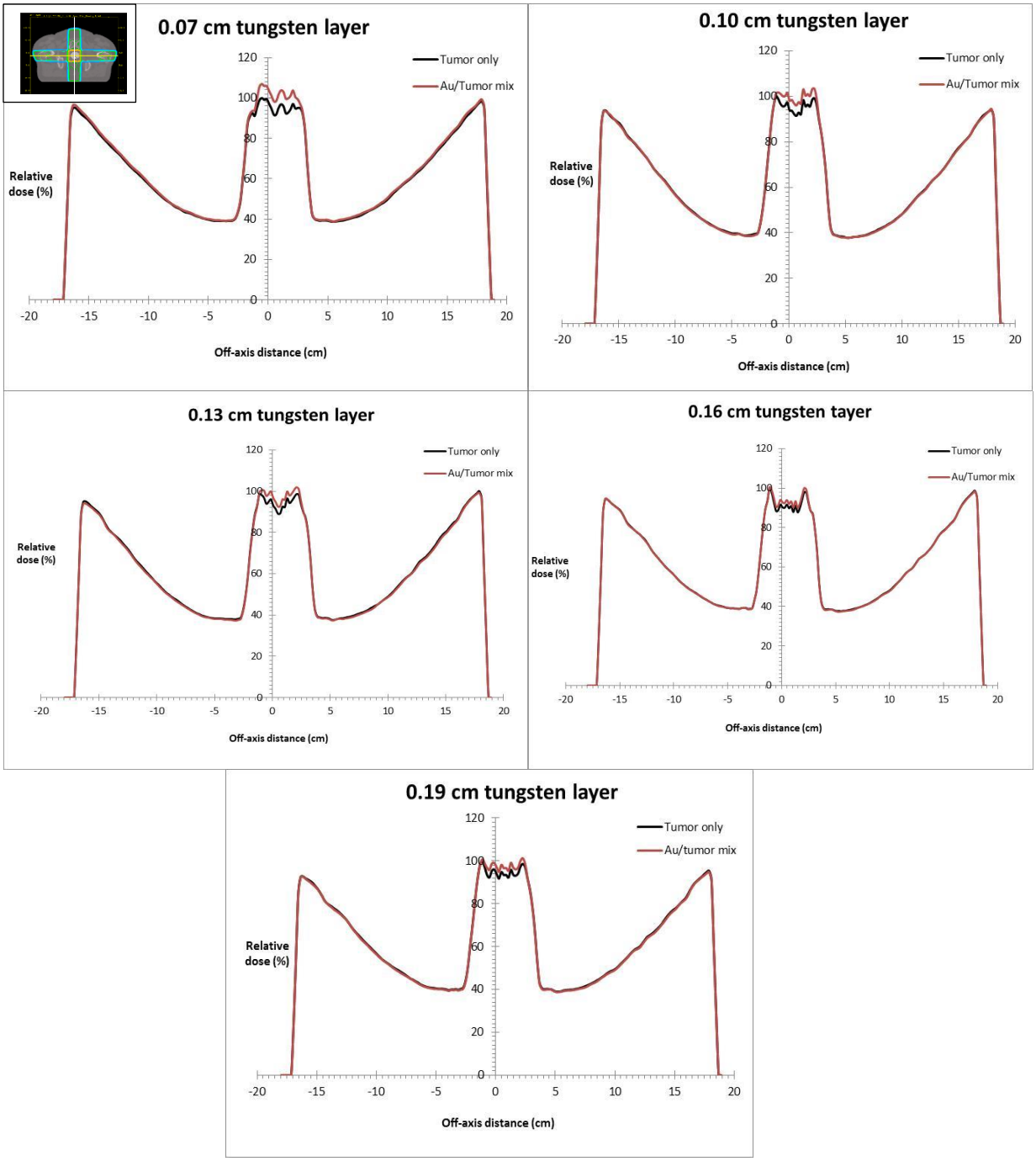

Figure 6.21: DPs along the *x*–axis for a 4F box plan with and without NPs in the PTV from beams obtained from Bremsstrahlung target combinations of a constant water layer (2.5 cm) and various tungsten layers**.**

Table 6.5: Average DEFs for various tungsten layers and a constant water layer of 2.5 cm. The uncertainty in the data is 1.5%.

	Tungsten layer (cm)				
	0.07	**0.10**	**0.13**	**0.16**	**0.19**
Average photon energy (MV)	**0.427**	**0.460**	**0.483**	**0.502**	**0.521**
DEF	**1.069 ± 0.015**	**1.051 ± 0.015**	**1.040 ± 0.015**	**1.025 ± 0.015**	**1.036 ± 0.015**

Dose enhancement is more prominent at 2.5 cm water thickness as shown in table 6.5. At this thickness the average mean photon energy was found to be 0.483 MV which was the lowest energy among all other thicknesses. For kilovoltage interactions, the total energy deposition is dominated by the photoelectric effect. This physical phenomenon dominates therefore a high dose enhancement is obtained.

At high kilovolt energies and low megavolt energies obtained below 2.5 cm water thickness Compton scattering becomes dominant which contribute less to the generation of photoelectrons suitable for dose enhancement, therefore dose enhancement is low.

Dose profiles of 0.8 cm and 1.4 cm are flat along the central axis. As illustrated by planar dose profiles above and it is evident that the two-target configuration contributes to absorption of x-ray energy photons along the beam central axis in the PTV when enriched with NPs.

Changing tungsten thickness and keeping water constant also demonstrates the dependence of dose enhancement on the mean energy. At thinner tungsten layer of 0.07 cm, highest dose enhancement was obtained and the lowest dose enhancent was obtained at the thicker tungsten Bremsstrahlung target. The energy of the beam increase with increase in tungsten thickness due to internal absorption of lower energy photons in the target itself.

6.5.1.2 Dose distributions for Carbon/Tungsten Bremsstrahlung Target Combinations

The next set of graphs shows the DEF along the x-axis for a constant layer of 0.14 cm of tungsten and two different thicknesses of carbon.

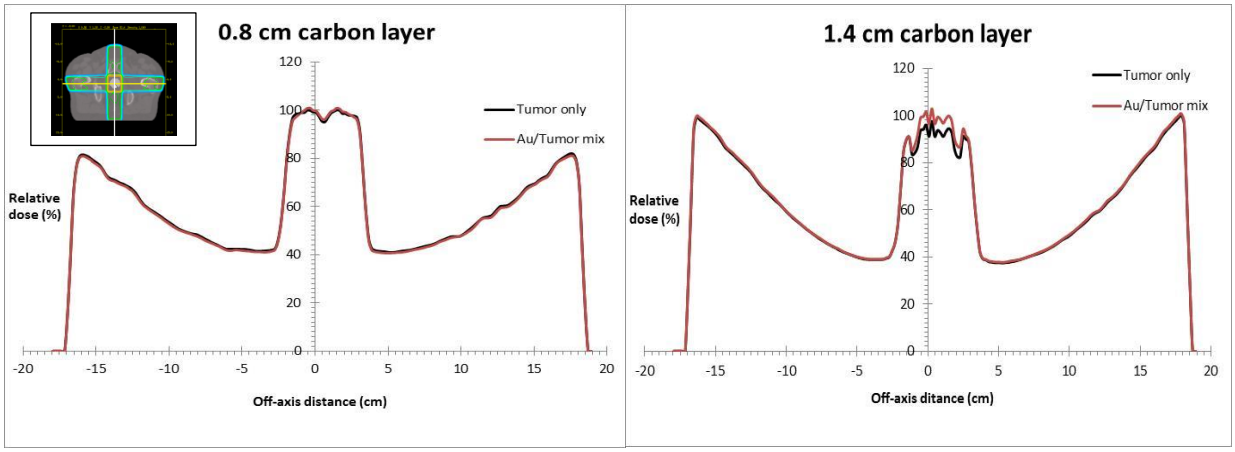

Figure 6.22: DPs along the *x*–axis for a 4F box plan using the patient CT phantom with and without NPs from beams obtained from Bremsstrahlung target combinations of a constant tungsten (0.14 cm) layer and two carbon layers.

Table 6.6: Average DEFs for two carbon layers and a constant tungsten layer (0.14 cm) Uncertainty in DEFs is 1.5%.

	Carbon layer (cm)	
	0.8	**1.4**
Average photon energy (MV)	**0.770**	**0.428**
DEF	**1.011 ± 0.015**	**1.051 ± 0.015**

The next set of graphs shows the DPs for a constant layer of 1.4 cm carbon and various layers of tungsten.

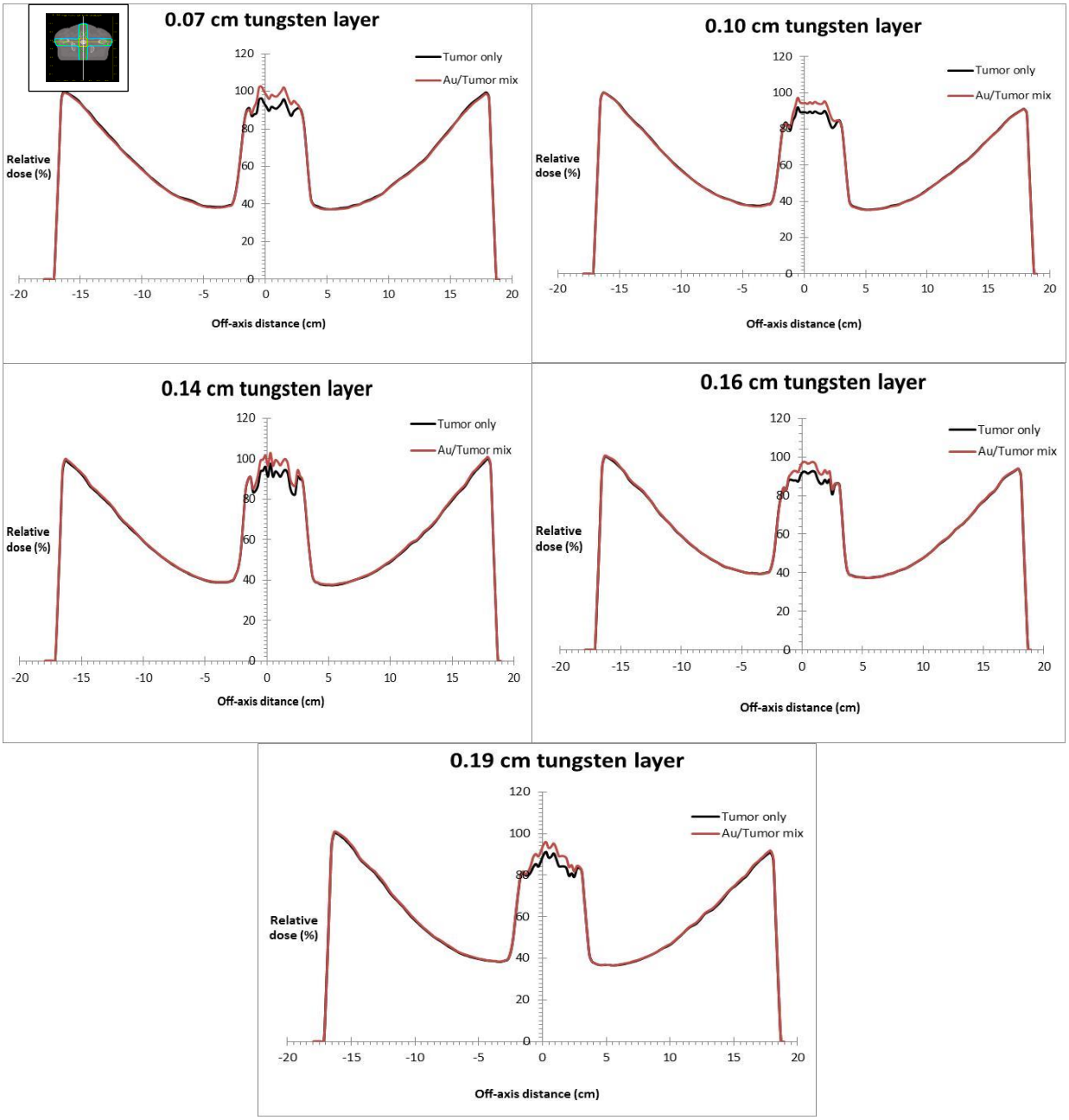

Figure 6.23: DPs along the *x*–axis for 4F box plan using CT phantom study set with and without NPs from beams obtained from Bremsstrahlung target combinations of a constant carbon layer (1.4 cm) and increasing tungsten layers **.**

Table 6.7: Average DEFs for a constant carbon layer, 1.4 cm, and different tungsten layers. The uncertainty in the data is 1.5%.

	Tungsten layer (cm)				
	0.07	**0.10**	**0.14**	**0.16**	**0.19**
Average photon energy (MV)	**0.368**	**0.395**	**0.428**	**0.441**	**0.457**
DEF	**1.074 ± 0.015**	**1.057 ± 0.015**	**1.051 ± 0.015**	**1.056 ± 0.015**	**1.053 ± 0.015**

Results obtained using carbon/tungsten target combinations in figures 6.22 and 6.23 have relative high dose enhancement values compared to water/tungsten Bremsstrahlung target combinations. A DEF value of 7.4 ± 1.5% was obtained at 0.07 cm tungsten thickness combined with 1.4 cm carbon compared to 6.9 ± 1.5% obtained using water. The dose enhancement of these target combinations also depends on the beam energy as shown in tables 6.6 and 6.7. For carbon the maximum dose enhancement occurs at 1.4 cm thickness when tungsten is kept constant at 0.07 cm. Similar observation was found using a water layer of thickness 2.5 cm. There is also a decrease of dose enhancement with increase in tungsten thickness since the beam energy starts to increase due to preferential attenuation of low energy photons.

Based on 4F plan results, carbon is more efficient at moderating the electron beam to generate photon beams for dose enhancement at lower thickness compared to water, although water can just be as good at larger thickness.

6.5.2 Five Field Plan Simulations

Figure 6.24 show isodose distributions in a 5F plan. The five beams consist of an anterior/posterior beam, gantry angle at 0^0 and 4 oblique beams at gantry angles 45^0, 135^0, 225^0 and 315^0. The oblique beam angles avoids the pelvis bones, hence there is less attenuation of the photon beam. Bones have a higher density and a high average atomic number compared

to soft tissue, hence they cause beam attenuation which leads to lower dose delivery to the PTV. Therefore 5F plan gives a better target coverage in the PTV and increased dose delivery to the tumour compared to a 4F box plan.

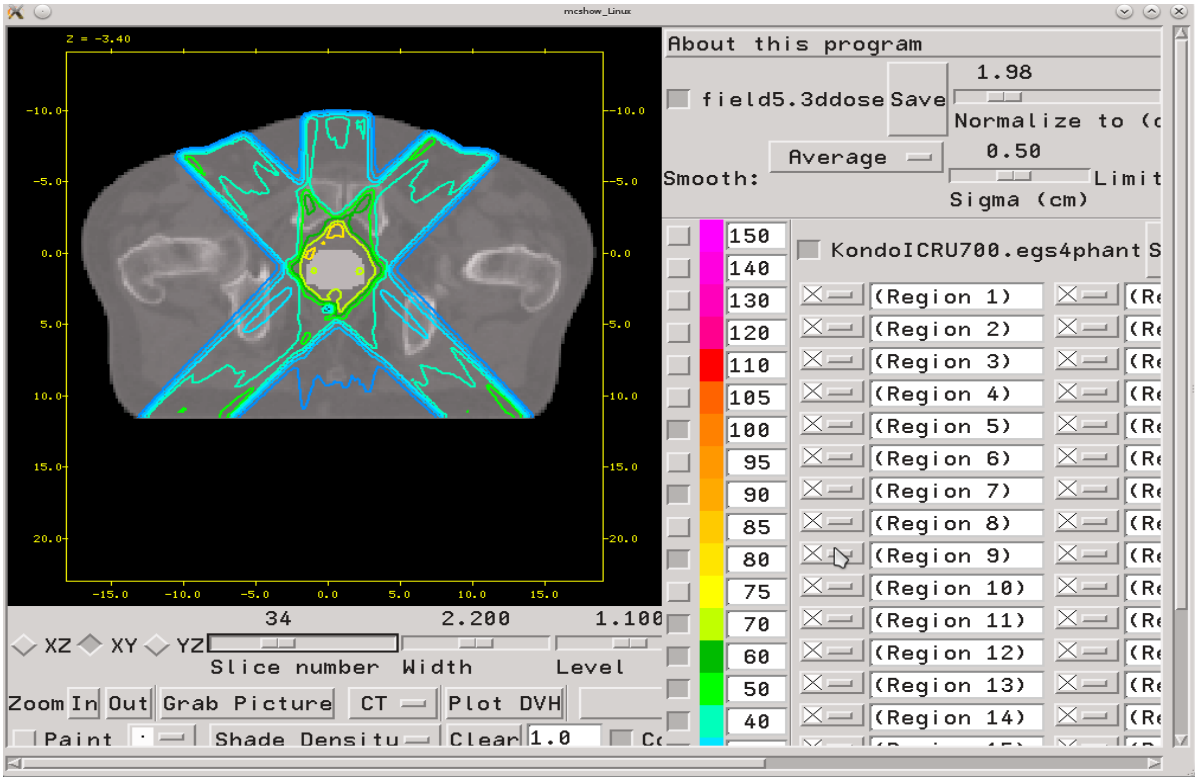

Figure 6.24: MCSHOW GUI showing the isodose curves through isocentre for 5F plan beam obtained from DOSXYZnrc simulations of a patient CT phantom.

6.5.2.1 Dose Distributions for Water/Tungsten Bremsstrahlung Target Combinations

The next set of four figures shows the DP along the x-axis for the 5F plan. The CT data insert in the first figure shows the yellow x-axis on it. The water thickness is varied while the tungsten target has a fixed value of 0.14 cm.

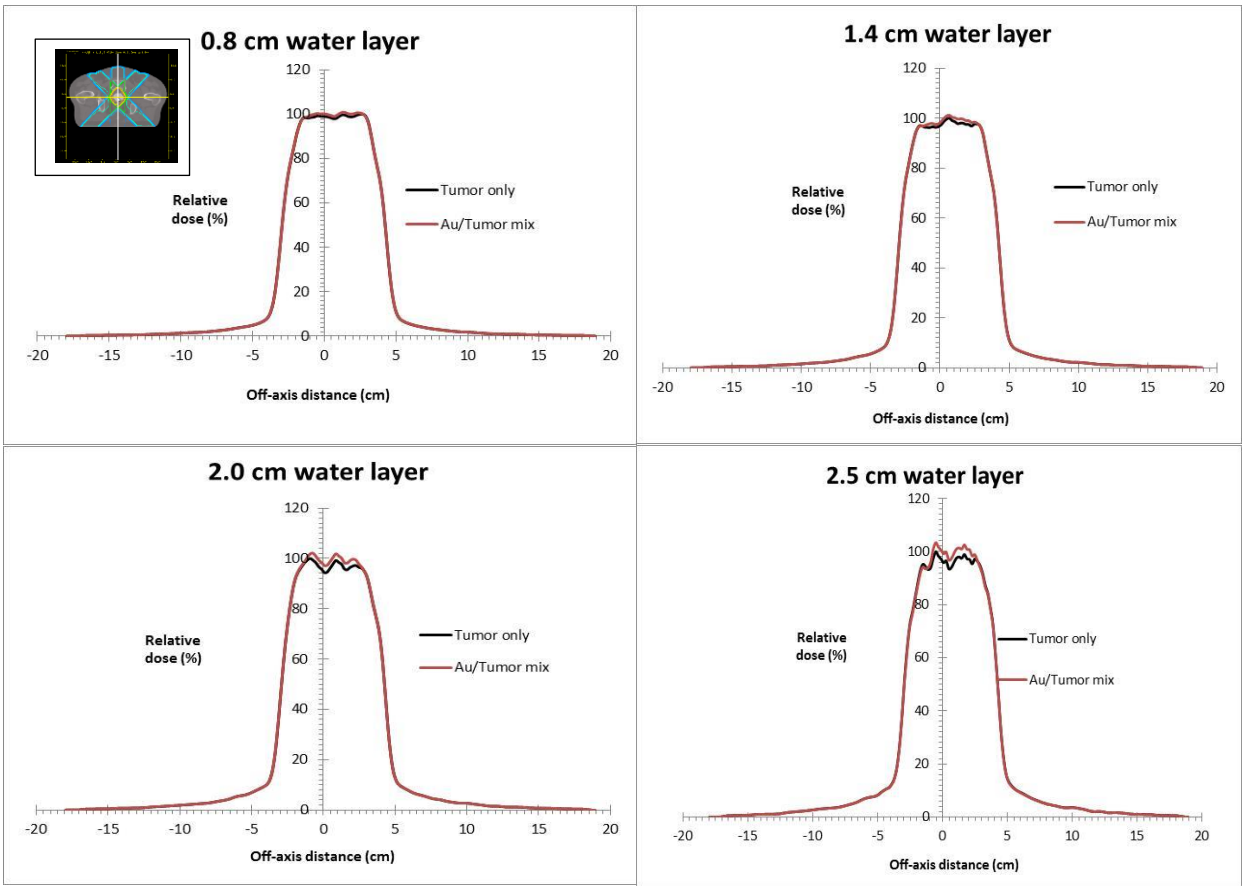

Figure 6.25: Calculated DPs along the *x*–axis (yellow line on insert in first figure) for a 5F box plan at using patient CT phantom with and without NPs from beams obtained from Bremsstrahlung target combinations of a constant tungsten layer and various water layers.

Table 6.8: Average DEFs for various water layers (primary target) and a constant (0.13 cm) tungsten layer (secondary target) beams. The uncertainty in the data is 1.5%.

	Water layer (cm)			
	0.8	**1.4**	**2.0**	**2.5**
Average photon energy (MV)	**1.000**	**0.864**	**0.669**	**0.483**
DEF	**1.011 ± 0.015**	**1.012 ± 0.015**	**1.028 ± 0.015**	**1.046 ± 0.015**

In the next set of graphs the water layer is retained at 2.5 cm thickness while the tungsten layer in the secondary target is now varied from 0.07 cm to 0.19 cm.

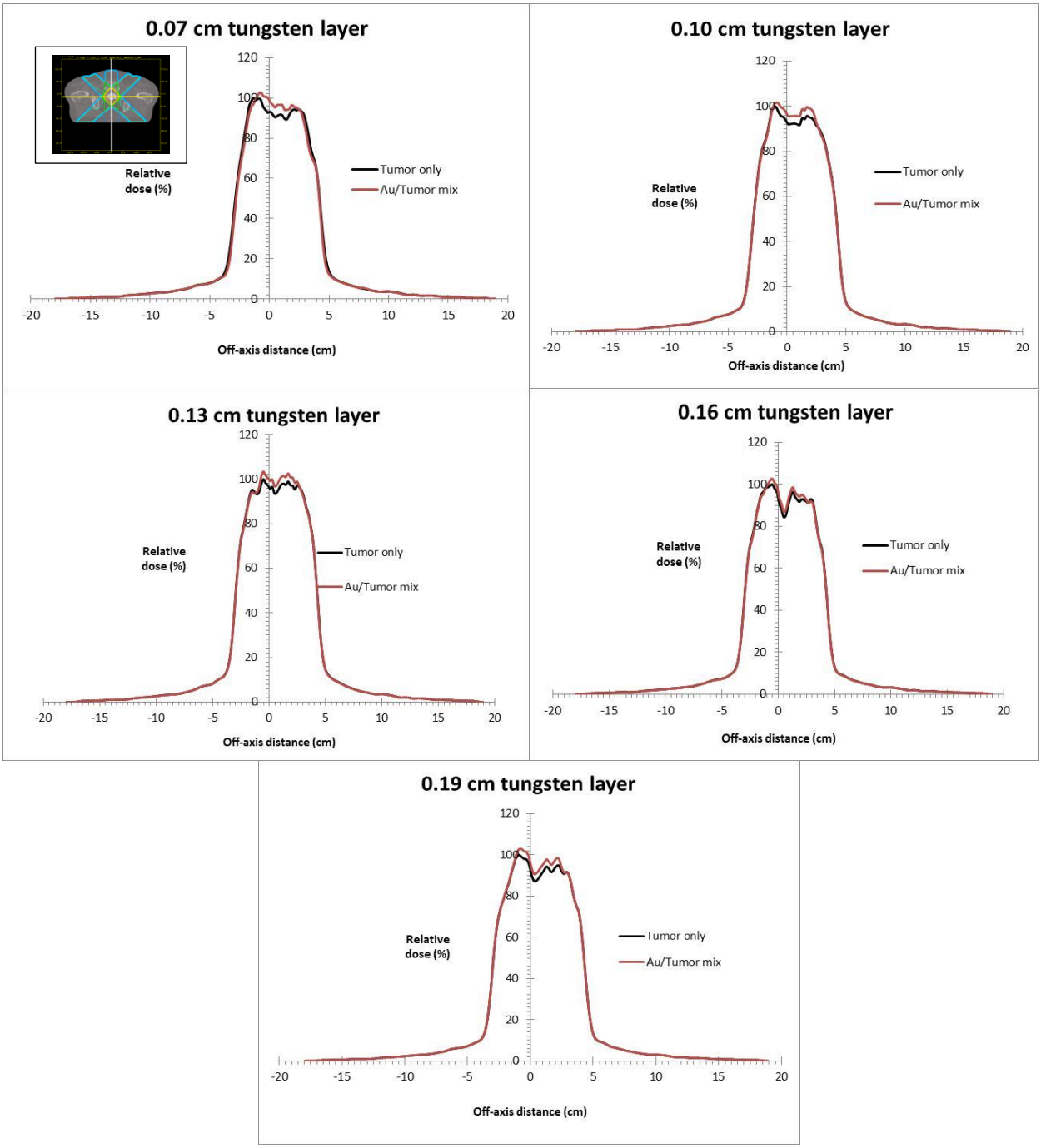

Figure 6.26: DPs along the *x*–axis for a 5F box plan obtained from Bremsstrahlung target combinations of a constant water layer and various tungsten layers.

Table 6.9: Average DEFs for various tungsten layers and constant water layer (2.5 cm). The uncertainty of the DEF is 1.5%.

	Tungsten layer (cm)				
	0.07	**0.10**	**0.13**	**0.16**	**0.19**
Average photon energy (MV)	**0.427**	**0.460**	**0.483**	**0.502**	**0.521**
DEF	**1.053 ± 0.015**	**1.047 ± 0.015**	**1.046 ± 0.015**	**1.040 ± 0.015**	**1.041 ± 0.015**

For the 5F planning strategy the DEFs follow the trend of that for a 4F box plan in terms of the beam energy and the bremstrahlung target combination. High dose enhancement are obtained at the lowest energy photon beams. At 0.13 cm tungsten thickness for constant water layer of 2.5 cm DEFs are 4 ± 1.5% and 4.6 ± 1.5% for 4F and 5F strategy respectively.

According to figure 6.25 at thin water target layers such as 0.8 cm and 1.4 cm, the beam profiles are almost flat at PTV compared to thicker targets with spiked profiles. For a thicker target, this could be due to the absorbtion of photons as stated earlier. The same observation is observed for thicker tungsten layers above 0.13 cm. The MC simulation predicts high dose enhancement of about 5.3 ± 1.5% in the PTV in this 5F plan.

6.5.2.2 Dose Distributions for Carbon/Tungsten Bremsstrahlung Target Combinations.

Next two graphs are shown for DPs for the 5F plan for primary targets of 0.8 and 1.4 cm thickness of carbon. The secondary Bremsstrahlung target was kept constant at 0.14 cm tungsten.

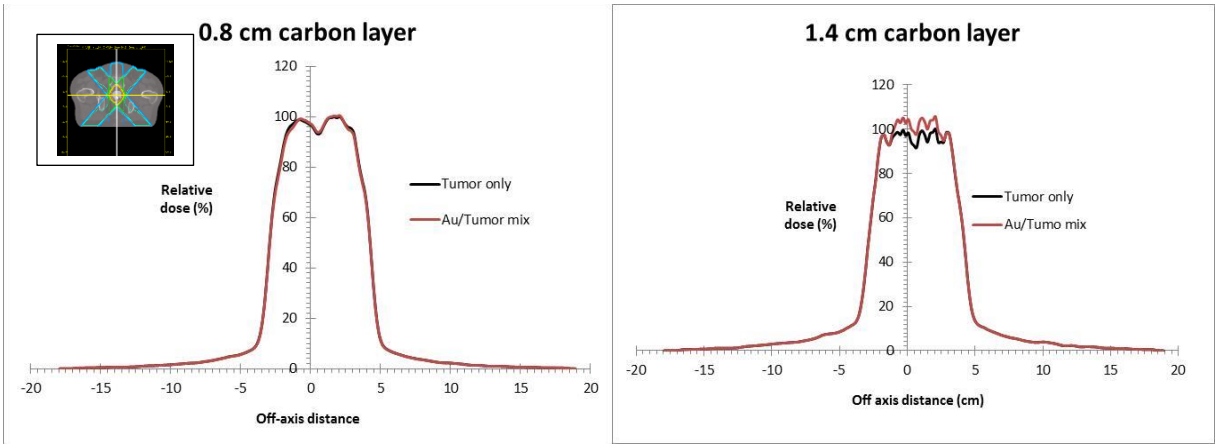

Figure 6.27: DPs along the *x*–axis for a 5F box plan from beams obtained from Bremsstrahlung target combinations of a constant tungsten layer (0.14 cm) and various carbon layers.

Table 6.10: Average DEFs for two carbon layers and constant tungsten layer (0.14 cm). The uncertainty in the data is 1.5%.

	Carbon layer (cm)	
	0.8	**1.4**
Average photon energy (MV)	**0.770**	**0.428**
DEF	**1.012 ± 0.015**	**1.060 ± 0.015**

In the next set of graphs the carbon layer is kept at 1.4 cm thickness while the tungsten layer in the secondary target is now varied between 0.07 to 0.19 cm.

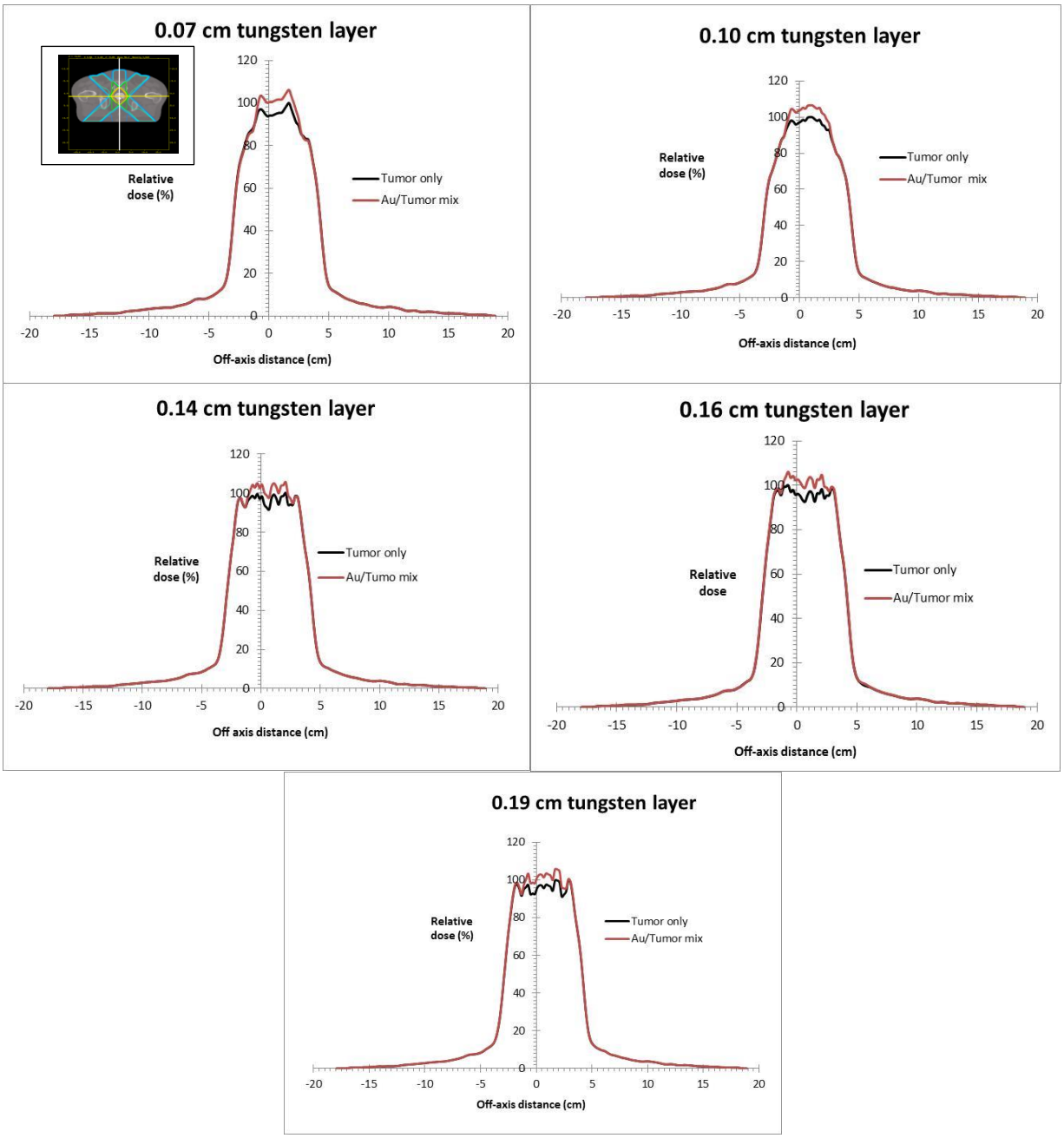

Figure 6.28: DPs along the x–axis for a 5F box plan from beams obtained from Bremsstrahlung target combinations of constant carbon layer, 1.4 cm and different tungsten layers .

Table 6.11: Average DEFs for a constant carbon layer (1.4 cm) and different tungsten layers. The uncertainty in the data is 1.5%.

	Tungsten layer (cm)				
	0.07	**0.10**	**0.14**	**0.16**	**0.19**
Average photon energy (MV)	**0.368**	**0.395**	**0.428**	**0.441**	**0.457**
DEF	**1.075 ± 0.015**	**1.069 ± 0.015**	**1.060 ± 0.015**	**1.059 ± 0.015**	**1.055 ± 0.015**

According to results in table 6.10 and 6.11, carbon/tungsten target combinations enhance dose better at 5F plan than at 4F plan. The dose enhancement also depend on the photon energy and target thickness. For tungsten layers dose enhancement was highest at 0.07 cm thickness which had the lowest photon energy and for carbon it was also highest at 1.4 cm.

6.5.3 Six field Plan Simulations

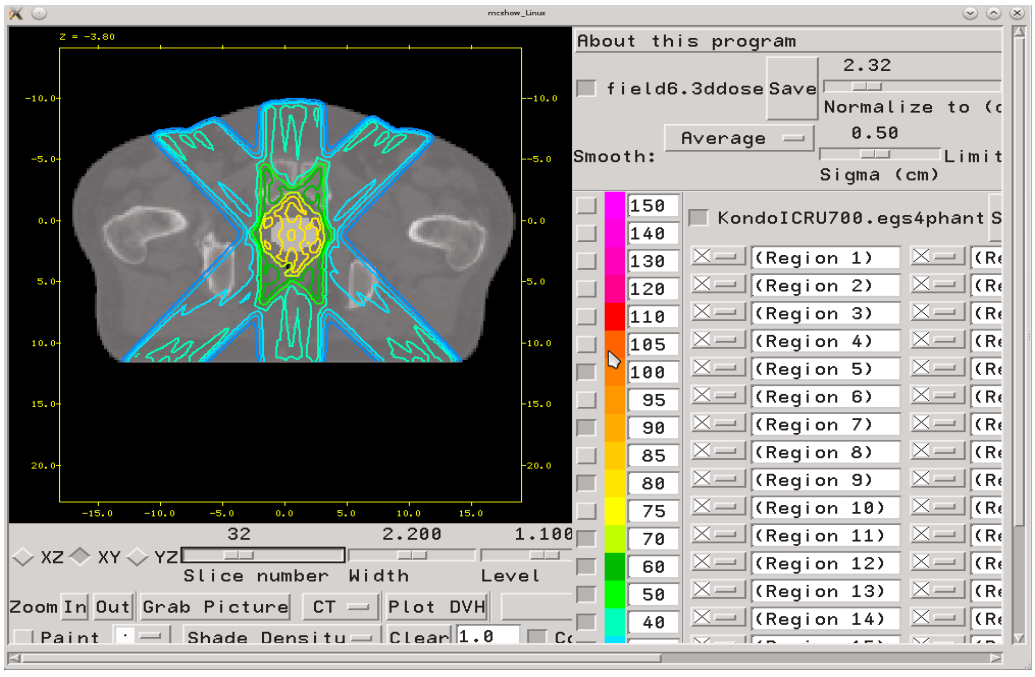

Figure 6.29: MCSHOW GUI showing the isodose curves through isocentre for 6F plan photon beam obtained from DOSXYZnrc simulations of a patient CT phantom

The 6F plan produces better PTV dose conformity compared to the 4F and 5F strategy, therefore a high dose is delivered to the target. The 6F plan involves 4 oblique angle beams and AP and PA beams. The oblique beams avoid the pelvis bone. The investigation didn't focus on the organs at risk as we were more interested in determining the amount of dose enhancement.

6.5.3.1 Dose Distributions for Water/Tungsten Bremsstrahlung Target Combinations

As in the previous two cases for 4F and 5F plans, the effect of varying the primary water or carbon target, to produce the exit electron spectra that fall in on the secondary tungsten target, that are also varied, is investigated in terms of DEF.

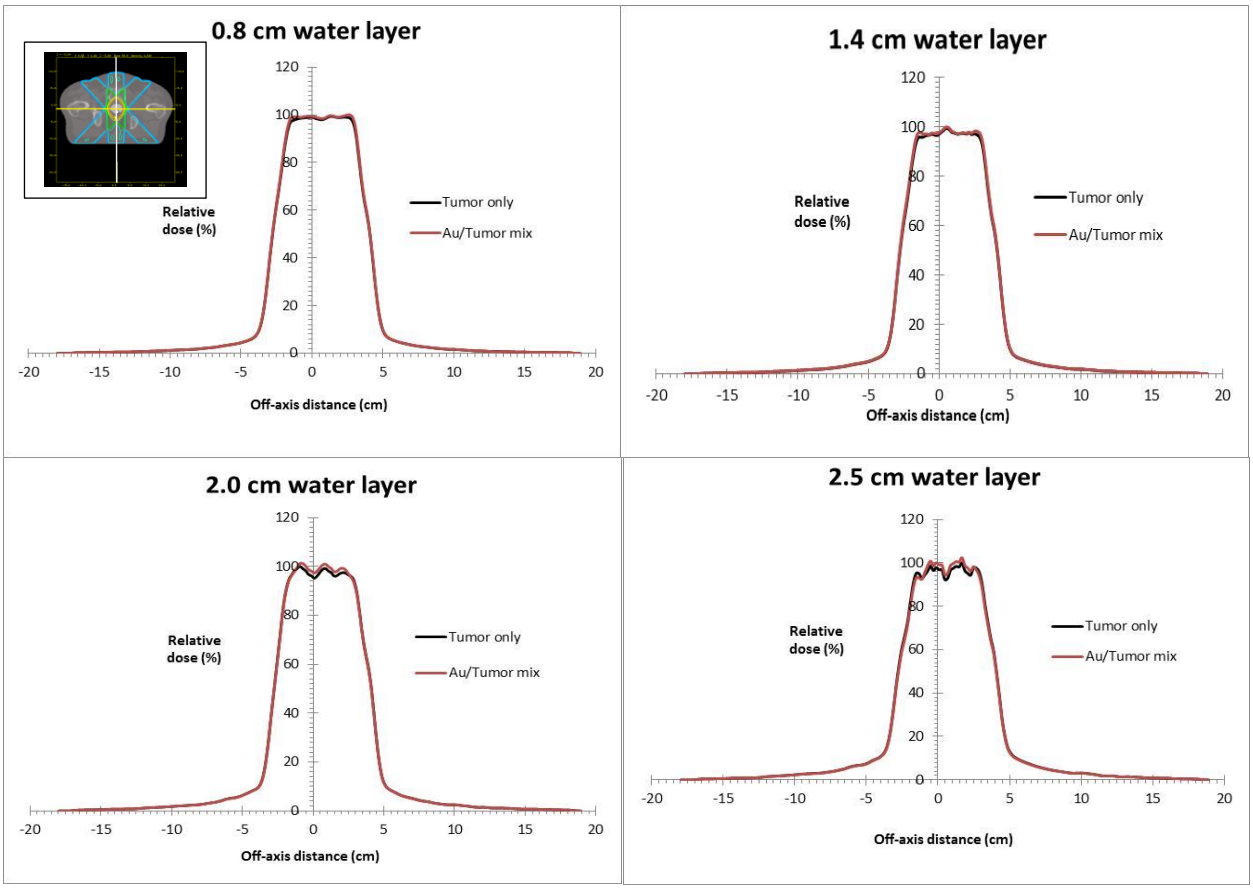

Figure 6.30: DPs along the *x*–axis for a 6F box plan from beams obtained from Bremsstrahlung target combinations of a constant tungsten layer and various water layers.

Table 6.12: Average DEFs for various water layers and a constant tungsten layer beams (0.14 cm). The uncertainty in the data is 1.5%.

	Water layer (cm)			
	0.8	**1.4**	**2.0**	**2.5**
Average photon energy (MV)	**1.000**	**0.864**	**0.669**	**0.483**
DEF	**1.005 ± 0.015**	**1.006 ± 0.015**	**1.020 ± 0.015**	**1.025 ± 0.015**

It was observed that using 6F for water/tungsten Bremsstrahlung target beams, dose was enhanced almost in the same manner as using 4F or 5F plan in terms of beam energies and target thicknesses although the DEFs were lower compared to these other two planning strategies. At 0.8 cm and 1.4 cm water thickness the enhancement is very low as these target thicknesses produce high energy beams. As it can be seen at 2.5 cm water thickness for 6F and 5F plan the MC dose enhancement ratio calculated were 2.5 ± 1.5% (Table 6.12) and 4.6 ± 1.5% (Table 6.8) respectively. This implies that higher dose enhancement ratio can be experienced using beams that avoid the spine.

Table 6.13: Average DEFs for various tungsten layers and constant water layer (2.5 cm). The uncertainty in the data is 1.5%.

	Tungsten layer (cm)				
	0.07	**0.10**	**0.13**	**0.16**	**0.19**
Average photon energy (MV)	**0.427**	**0.460**	**0.483**	**0.502**	**0.521**
DEF	**1.047 ± 0.015**	**1.035 ± 0.015**	**1.025 ± 0.015**	**1.035 ± 0.015**	**1.033 ± 0.015**

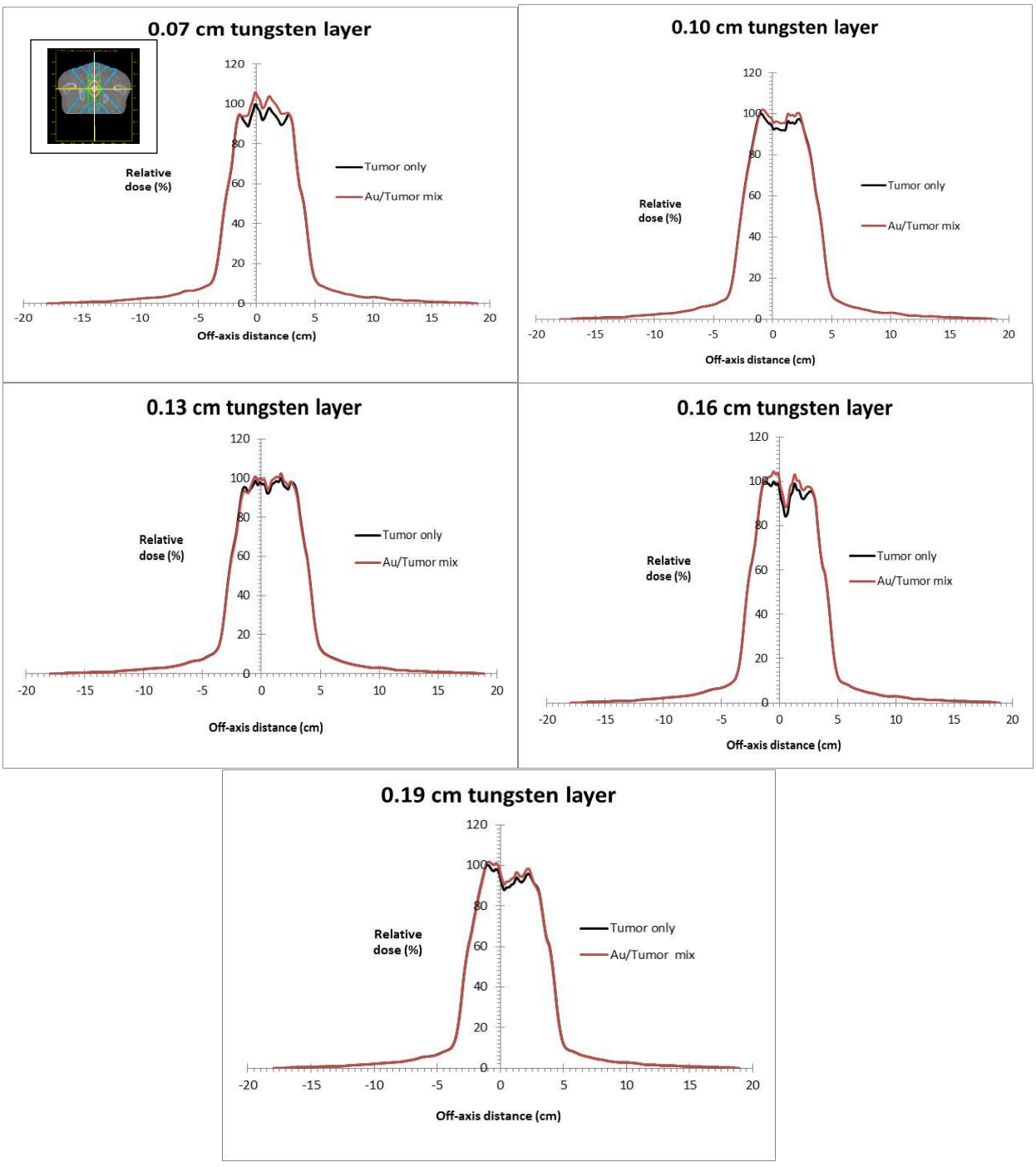

Figure 6.31: DPs along the *x*–axis for a 6F box plan from beams obtained from Bremsstrahlung target combinations of a constant water layer and various tungsten layers .

6.5.3.2 Dose Distributions for Carbon/Tungsten Bremsstrahlung Target Combinations

The following two graphs on figure 6.32 show the DPs obtained using photon beams from carbon/tungsten target combination.

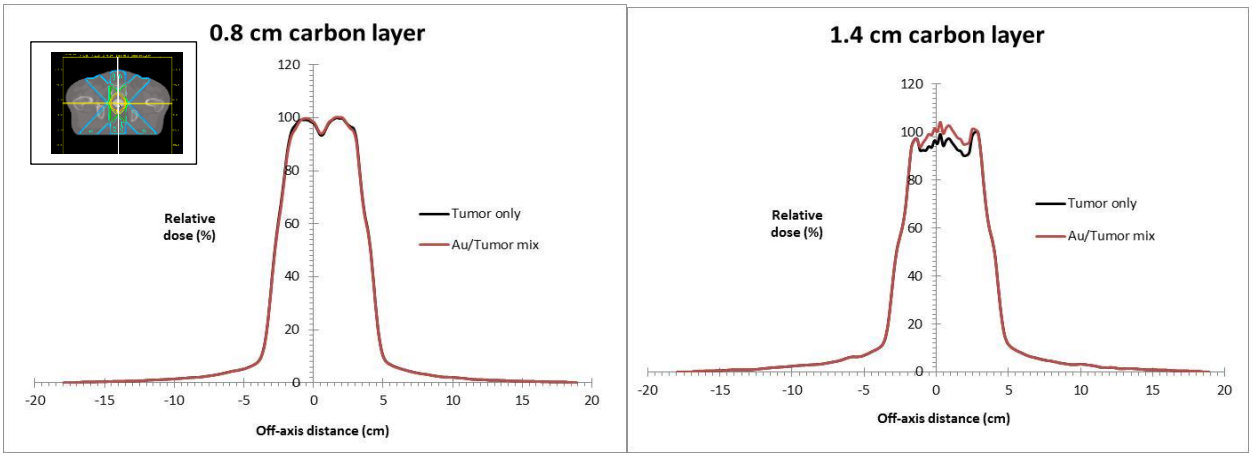

Figure 6.32: DPs along the *x*–axis for a 6F box plan from beams obtained from Bremsstrahlung target combinations of a constant tungsten layer (0.14 cm) and various carbon layers.

Table 6.14: Average DEFs for two carbon layers and a constant tungsten layer (0.14 cm). The uncertainty in the data is 1.5%.

	Carbon layer (cm)	
	0.8	**1.4**
Average photon energy (MV)	**0.770**	**0.428**
DEF	**1.007 ± 0.015**	**1.032 ± 0.015**

Set of graphs below on figure 6.33 demonstrate dose enhancement using beams obtained using constant carbon layer thickness (0.14 cm) and different tungsten thicknesses.

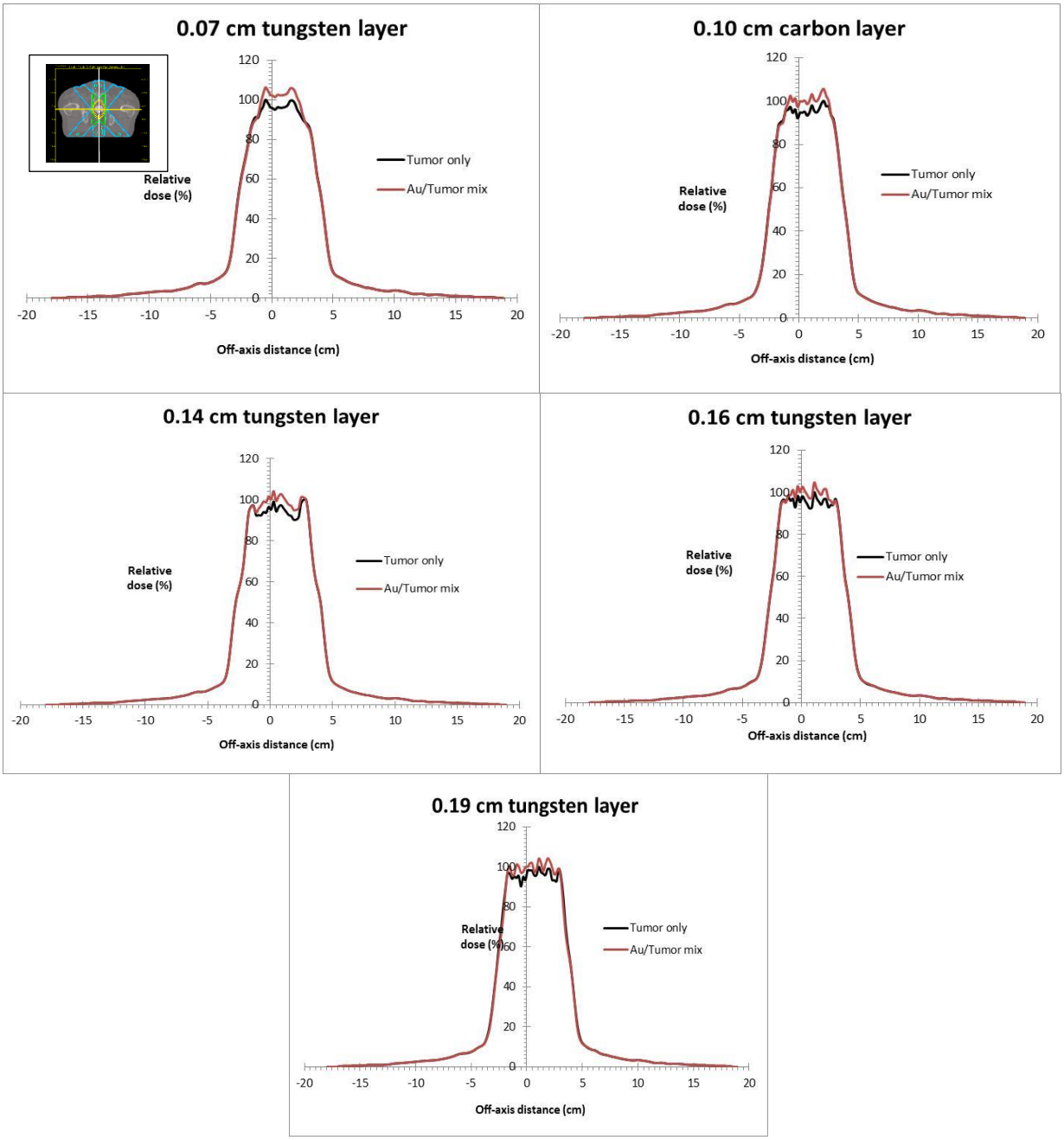

Figure 6.33: DPs along the *x*–axis for a 6F plan from beams obtained from Bremsstrahlung target combinations of a constant carbon layer, 1.4 cm and different tungsten layers

Table 6.15: Average DEFs for a constant carbon layer (1.4 cm) and different tungsten layers. The uncertainty in the data is 1.5%.

	Tungsten layer (cm)				
	0.07	**0.10**	**0.14**	**0.16**	**0.19**
Average photon energy (MV)	**0.368**	**0.395**	**0.428**	**0.441**	**0.457**
DEF	**1.065 ± 0.015**	**1.041 ± 0.015**	**1.032 ± 0.015**	**1.041 ± 0.015**	**1.040 ± 0.015**

The beam profiles observed in figures 6.32 and 6.33 are similar to those for 5 field plan for the same target combinations.

6.6 Original Flattening Filter Free 6 MV Beam Results

Figure 6.34 and table 6.16 shows that the photon dose enhancement using the 6 MV photon beam from the original target of 0.3 cm tungsten thickness is significantly lower compared to the dose enhancement obtained using primary targets of either water or carbon that act as electron moderators. According to the results in figure 6.34, a maximum dose enhancement of 0.5% was obtained using the original Bremsstrahlung target for 5F treatment strategy compared to a maximum dose enhancement of approximately 6% and 7.5% for water/tungsten and carbon/tungsten Bremsstrahlung target combinations respectively using the same treatment strategy. According to the DPs plotted, the plots for the tumour and gold NPs/tumour mixture at each graph are almost overlapping showing poor dose enhancement. The enhancement is lower for the original beam as expected since the average energy of original beam is very high (1.38 MV) compared to new modelled beams with mean energies ranging between 0.3 MV and 1 MV. At this high energy compton events are dominant which contribute less to tumour dose enhancement.

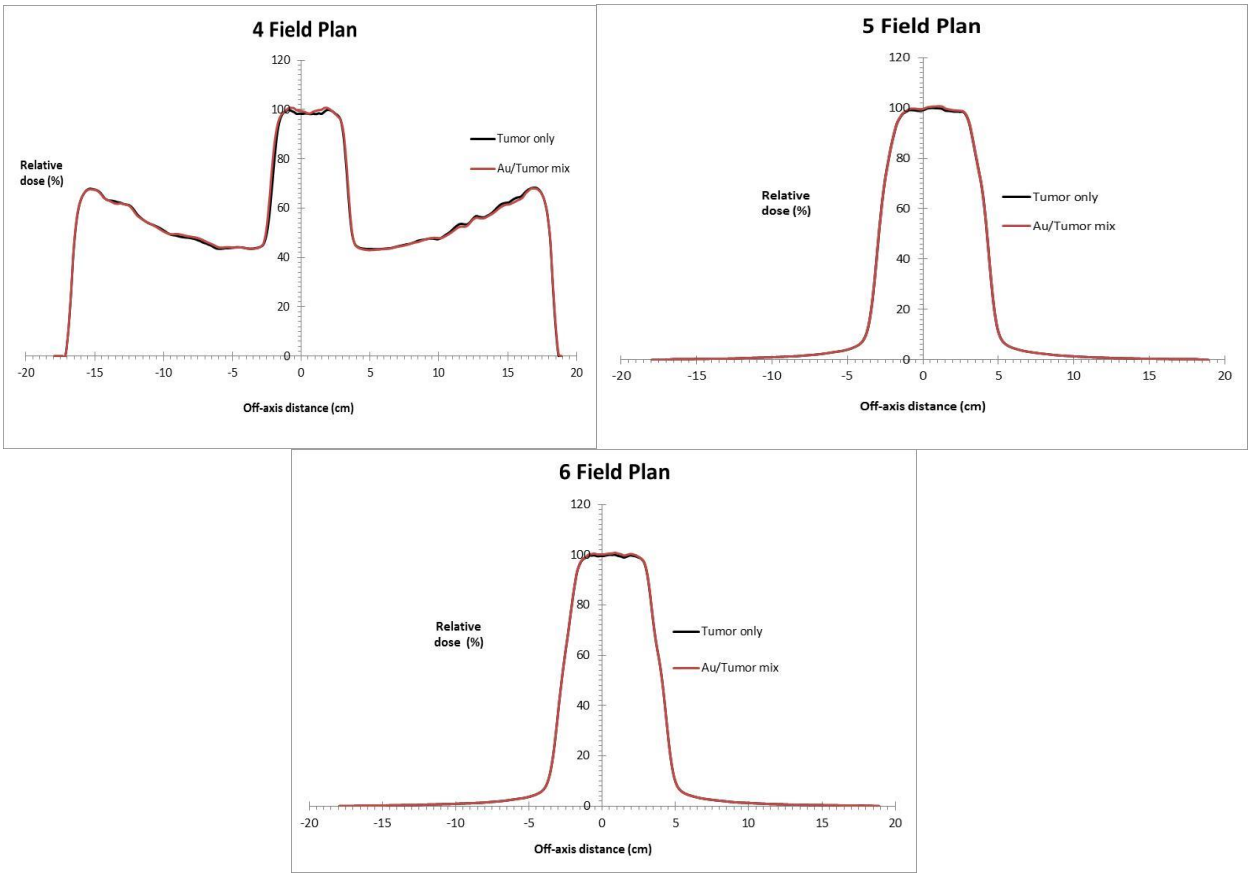

Figure 6.34: DPs along the *x*–axis for 4F box, 5F and 6F plan using an original beam from a 6 MeV FFF Elekta Precise Linac with original tungsten (0.3 cm) target

Table 6.16: Average DEFs for an original 6 MV FFF Elekta precise linac head. The uncertainty in the data is in the order of 1.5%.

Treatment Plan	4F	5F	6F
DEF	1.001 ± 0.015	1.005 ± 0.015	1.005 ± 0.015

By comparing the 3 treatment strategies investigated, namely 4F box, 5F and 6F, the general trend is that increasing the number of beams increases the dose delivery to the tumour, but the dose enhancement did not depend on the number of the fields. It appears the tumour dose enhancement depends on the beam angles in a sense that at certain angles more tissue needs

to be penetrated to reach the PTV. The beam may also have to penetrate bone structures in its path.

The beams that pass through the bones such as the spine and the pelvis bone which are high density and high Z materials contributed less to the tumour dose due to beam attenuation. Therefore the 5F plan had higher DEFs compared to the 4F strategy since most of its beams avoided bone structures such as the femurs with high density materials. 4F box had higher DEFs compared to 6F plan.

Therefore the choice of a treatment strategy is important for NPs seeded tumour radiation therapy because it can contribute in determining the optimum possible dose enhancement. As said, before, lower energy beams may enhance the dose in the tumour doped with NPs, but attenuation may reduce the primary dose at the tumour site to counter the effect of higher dose in the tumour. Although some researches have demonstrated dose enhancement with gold nanoparticles, the subject needs further research.

The following sections below (6.7 and 6.8) review the overall analysis of the effect of various photon beam energies generated using electron moderators (water or carbon primary targets) and different treatment plans dependence on NPs dose enhancement.

6.7: Photon Beam Energy Dependence on NPs Dose Enhancement.

Figures 6.35 (a) and (b) shows the dose enhancement factor as a function of mean photon energy for simulated water and carbon primary targets combined with constant tungsten layers in 0.1 MV energy intervals. The concentration as documented by Hainfield and the size of nanoparticles was kept constant as explained before. The plots show that dose enhancement is higher around the low kV photon energies of approximate 400kV and decreases with increase in photon energy. The uncertainty in the DEFs is 1.5%.

(a)

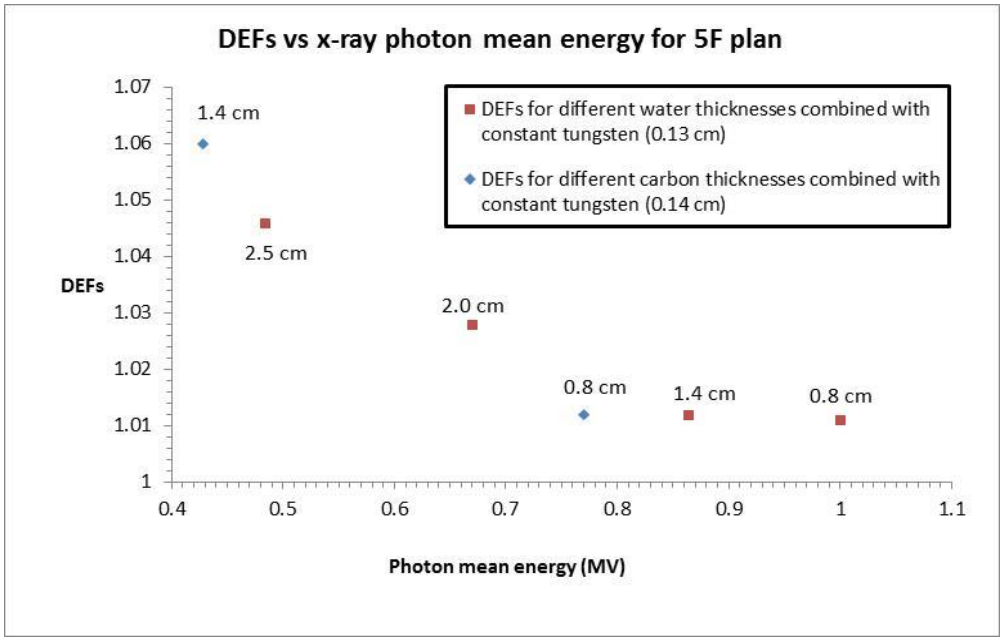

(b)

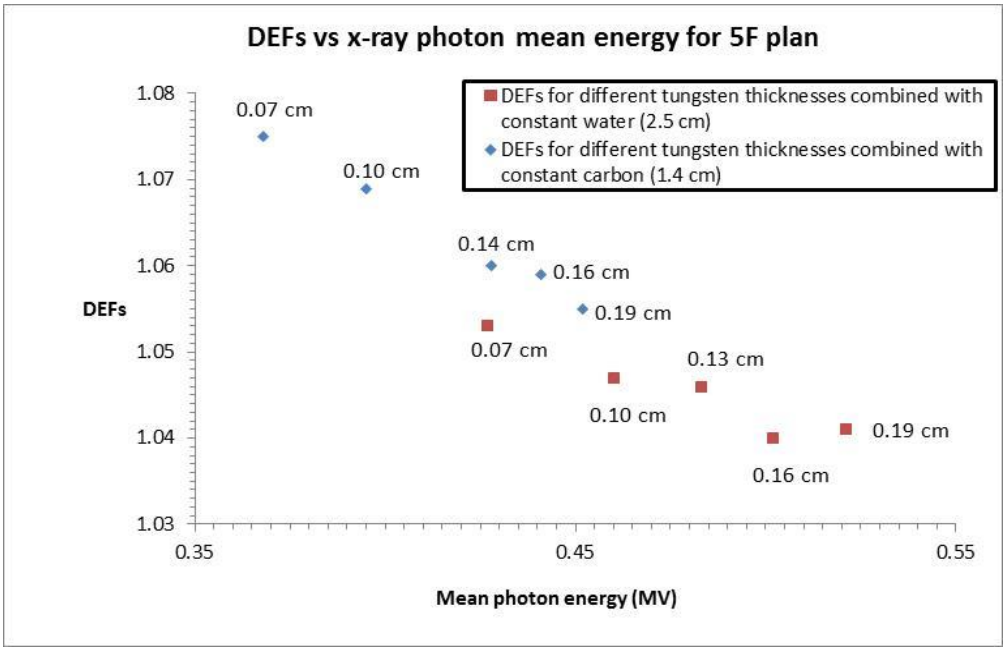

Figure.6.35: Dose enhancement factors vs mean photon energy for different Bremsstrahlung target thickness combinations for 5F plan for: (a) Constant tungsten layers. (b) Different tungsten layers.

The optimum energy for maximum dose enhancement in the tumour region at the isocentre of the beam was found to be about 0.4-0.5 MV. The absorbed dose enhancement is explained by production of additional short range Auger electrons that travels small ranges in tissue. The maximum DEFs obtained were around 7.5% with uncertainty of 1.5% at energies close to 0.4 MV and dropped to a minimum value of 0.1% using higher energy beams of approximately 1 MV.

Based on the results obtained, it is clear from figure 6.35 (a) above that the effective dose enhancement increases with increase in carbon or water target thickness combined with a constant tungsten layer of 0.13 cm and 0.14 cm for water and carbon respectively. When using carbon, dose enhancement increase to a maximum value at a thickness of approximately 1.4 cm and then drops as the thickness increases. As for water, dose enhancement increases to maximum at approximately 2.5 cm thickness. For water and carbon at 2.5 cm and 1.4 cm thickness respectively, it is where the lowest energy electron beams are produced before falling in on tungsten Bremsstrahlung target, hence higher dose enhancement.

6.8 Treatment Plan Dependence on NPs Dose Enhancement

According to figure 6.36 and 6.37, five fields setup demonstrates highest dose enhancement followed by 4 fields setup and 6 fields setup.

(a)

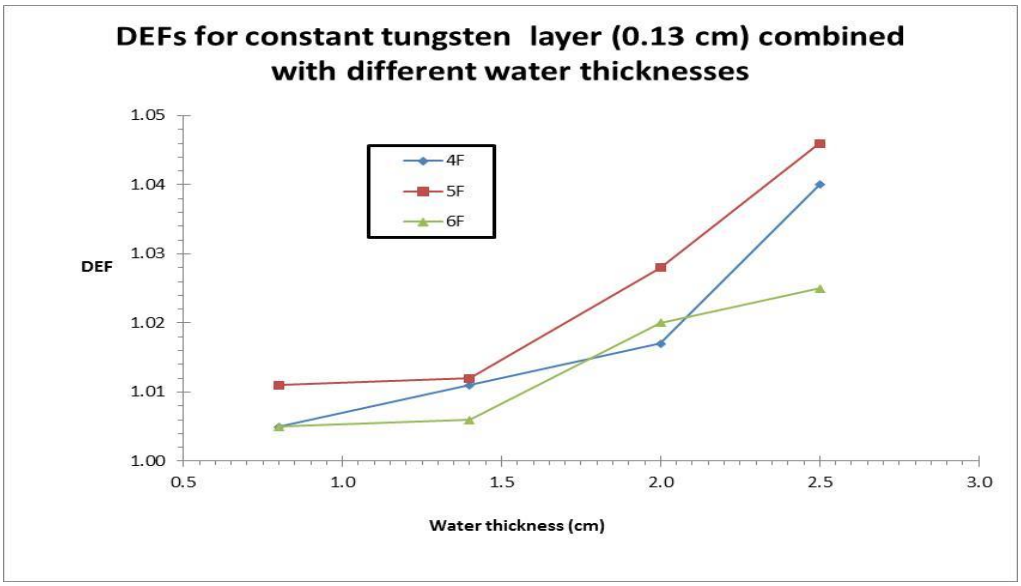

(b)

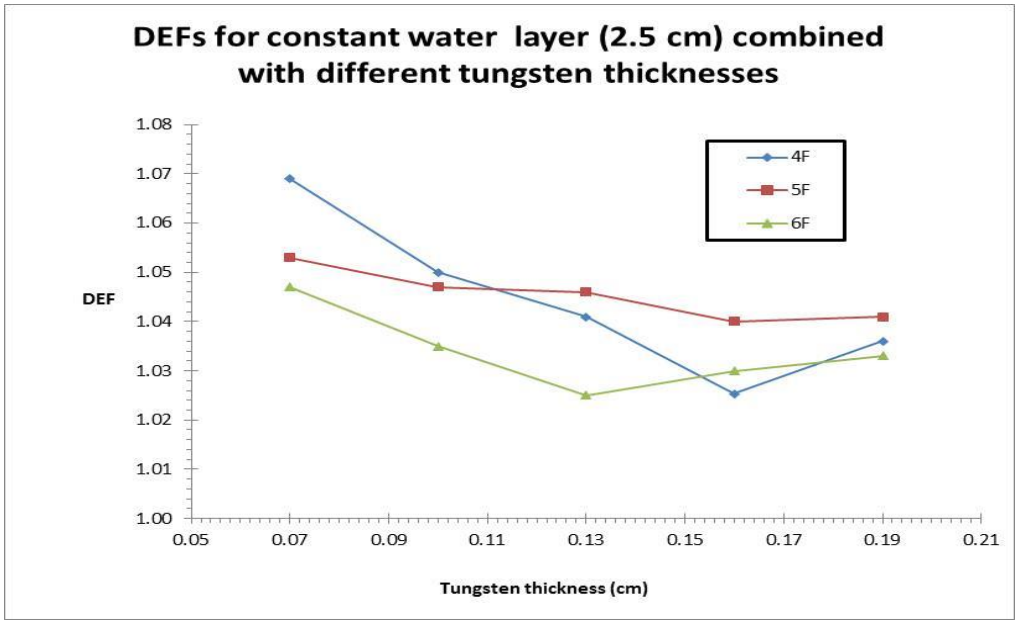

Figure 6:36 Dose enhancement factor vs. Bremsstrahlung target thickness for different target combinations for 4F, 5F and 6F plan. (a) Constant tungsten layer and different water thicknesses. (b) Different tungsten layers and a constant water layer.

(a)

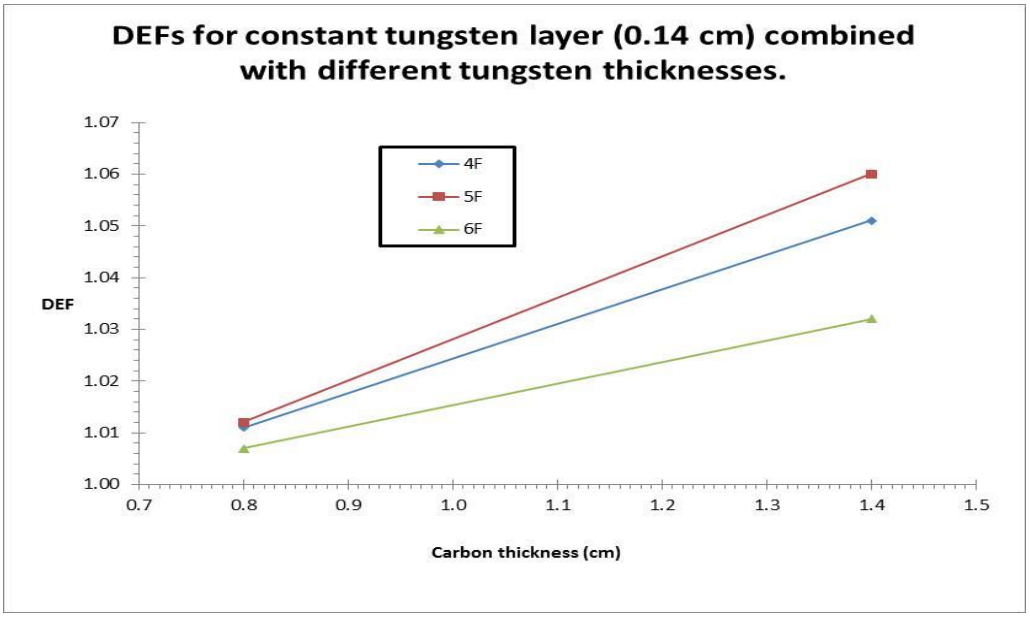

(b)

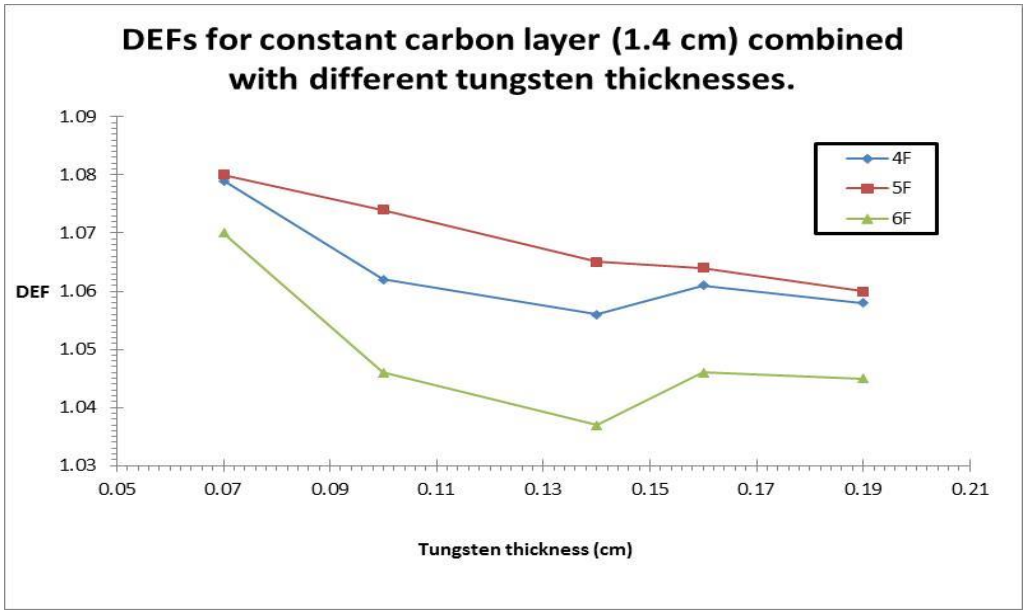

Figure 6:37 Dose enhancement factor vs Bremsstrahlung target thickness for different target combinations for 4F, 5F and 6F plan. (a) Constant tungsten layer and different carbon thicknesses. (b) Different tungsten layers and constant carbon layer.

The results in this chapter show the possibility of enhancing dose in tumour seeded with NPs using photon beams generated using a spectrum of electrons obtained after the 6 MeV beam exits from the waveguide and is slowed by either water or carbon. The atomic numbers of these targets were chosen to avoid excessive generation of unwanted Bremsstrahlung. Loading a tumour with high-Z material may improve selective dose delivery and minimize damage to surrounding normal tissue.

High-Z material have significantly higher photoelectric cross-sections than soft tissue for sub-MeV energies hence can produce low-energy Auger electrons which travels short distance that can locally enhance the effective radiation dose as reported by Kobayashi *et al.* (2010). The photoelectric effect dominates below the electron rest energy of 511 keV which is more relevant for radiation dose enhancement. Considering our results highest DEFs were obtained below 511 keV energy.

The effects of Au NPs seeded into the tumour on the dose enhancement shown on all the DPs in this study obtained along the central axis of the beam, presents the processes associated with physics of photon-matter and particle-matter interaction. These processes are the ones that lead to the deposition of dose into the PTV. A dose peak at the volume of interest that drops off quickly with increasing distance from the PTV along the central axis is usually due to electrons backscattered from the surface of the high Z material (Au NPs). The backscatter effect was not pronounced on the DPs since the amount of gold in the target was very low at 7mg/g tumour concentration. The energy of backscattered secondary charged particles is small at low photon energies, causing a rapid absorption of the scattered photons and charged particles in the medium within the region of interest since they traverse a short distance.

Nevertheless, the total dose in the tumour is the sum of the dose from the relatively long range energetic secondary charged particles (electrons and positrons) that are first released in the patient by photon interactions (photoelectric effect, Compton effect, pair production) and the dose due to the electrons/positrons backscattered into the same region by the NPs. Photoelectric effect is the primary photon interaction process in a high-Z material for photon energies below 1 MV. In this study, most energies generated had their average energy below 1

MV, therefore the photoelectric effect was more predominant, hence it was the main contributor to dose enhancement in the targeted volume.

Gold NPs were selected for this study and the results shown in this chapter shows that loading cancer cells with NPs of gold prior to a course of radiotherapy would promote their radiosensitisation. The DPs shows the difference only at the isocentre, at the PTV were the NPs were loaded. Previous computational studies by Cho *et al.* (2009) have also demonstrated the possibility of enhancing tumour dose using high-Z materials.

There are several studies that have been carried out to date regarding the use of NPs of high-Z material to enhance radiation dose, but several of these studies focused on the size, shape, concentration and depth of nanoparticle and not the energy of the beam [1,2].

These studies were carried out mostly by irradiating NPs using photon beams from conventional accelerators that use tungsten Bremsstrahlung targets. There is less information on the use of other Bremsstrahlung targets to investigate the effect of altered photon spectra. Hence this study was done to explore the use of an electron moderator (primary target) to generate lower energy Bremsstrahlung photon spectra in a secondary tungsten target. The results obtained were influenced mostly by the mean beam energy and the Bremsstrahlung target thickness. Thinner Bremsstrahlung targets favoured the emission of lower energy photons.

A similar study was done by Robar (2006) where he investigated NPs dose enhancement using experimentally generated x-ray beams using aluminium and beryllium targets. Our results agree in the sense that DEFs depends strongly on the energy of the beam and less on the target thickness. Also beams created with low-Z targets show significant changes in energy spectra compared to conventional tungsten targets. Several other studies have also demonstrated the possibility of higher dose enhancement at energies between 10 kV and 500 kV where the photoelectric effect is dominant.

Using a moderator such as water or carbon demonstrated in this study to produce softer x-ray beams in the secondary Bremsstrahlung target. The use of moderators led to a significant dose enhancement in NPs seeded in tumours, since a maximum of approximately 7.5% was obtained at the prostate tumour in this study. The tumour was located at 11 cm depth of the patient from AP direction. At 7.5% dose enhancement, the beam energy (0.368 MV) was the softest among the beams simulated at a constant carbon layer thickness of 1.4 cm as it can be noticed in table 6.11 and figure 6.35. At this low energy the most contributor of dose enhancement is from the photoelectric effect which depends on the inverse of the third power of photon energy ($1/E^3$).

The dependence of dose enhancement on the beam energy was also demonstrated by Cho. They estimated the DEF for various geometric set-ups of different AuNPs concentrations, at gamma rays, KV and MV photon by MC methods [1]. They found a less than 5% DEF at higher energy (18 MV) with a relatively high concentration (20-30 mg/ml) of radiosensitisation, which is lower than our results (7.5%) with a 7mg/g tumour concentration. For 18 MV beam the pair production process is the most dominant process in the high-Z element were it converts the photon energy to the energy of the secondary electrons/positrons. The results we obtained were also similar to a study by Cho (2005) that investigated teletherapy and brachytherapy applications of high-Z material using MC simulations. For photon energies of 6 MeV dose enhancement of 7.4% was achieved at a maximum Au concentration of 30 mg/g which was more than the concentration used in our study (7mg/g).

Softer beams are richer in low energy photons. Based on the conditions of this study 0.5% dose enhancement was obtained using an original FFF 6 MV beam and a maximum of 7.5% was also obtained using photon beams produced by water/carbon moderated electrons which is 15 times more than the original beam. Leung et al. also previous demonstrated that the interaction of a low energy photon beam (kV range) with AuNPs was stronger than the interaction of a 6 MV photon beam with AuNPs by two to three orders of magnitude [3]. This signifies that the use of altered photon spectra can improve dose enhancement in NPs seeded

tumours. The percentage combined error in dose enhancement factor values was less than 1.5% based on the number of MC histories simulated which were in the range of 10^9.

The two moderators were chosen for investigation due to their non-toxicity, low atomic number and also their availability that makes it cost effective. Carbon has a higher density than water and also has a high melting point which can sustain high energy electron beams incident on it, but also it might have to be cooled off with water. Due to its physical appearance, it can practically be fitted easily into the linac head. In terms of the mean energies calculated, the lowest energies were obtained using a carbon moderator and also the highest DEF was obtained using carbon. High DEF can be obtained with water too, but was not critically investigated.

MC simulations used in this study have been used previously to investigate radiation dose enhancement using NPs of high atomic number. Most simulations used a water phantom model with nanoparticles inside, which differs from this study where a real patient CT phantom with NPs seeded tumour was simulated. The DEFs results obtained here showed some relationship with previous studies especially in terms of photon energies.

The beams that we investigated had mean energies ranging between 0.3 MV and 1.4 MV. These beam energies were high enough to maintain skin sparing effect since the Monte Carlo simulations reported by Garnica-Garza (2011) showed that photon beam spectra with peak energies below 150 keV would cause unacceptably high skin irradiation. The results obtained for DEFs also agrees well with other previous studies that looked at the effect of beam energy on NPs dose enhancement that demonstrated the potential of kilovoltage irradiation as a better energy choice compared to higher photon energies [1.2,5].

It should be noted that the purpose of this study was to evaluate DEF factors obtained during the use of an x-ray photon beam obtained from a spectrum of electrons during irradiation of tumour seeded with nanoparticles. Therefore only a 6 MeV beam was selected for investigation as it is one of the major beam used in radiotherapy. Other beam energies such as 4, 10 and 18

MeV were not looked into. As for those energies above 6 MeV, their average photon energy is likely to be more than 1 MV which becomes irrelevant to photoelectric effect that contributes to dose enhancement. For energies below 6 MeV such as 4 MeV beam, DEFs are expected to be higher compared to 6 MeV as more kV photon energies relevant to dose enhancement are expected to be generated. Robar *et al.* looked at the effect of various MV photon energies on NPs at a 30 $mgml^{-3}$ gadolinium tumour concentration and 8.4%, 10.8%, 13.7% and 23.1% dose enhancements were achieved for 18 MV, 6 MV, 4 MV and 2 MV unflattened beams, respectively [6]. This study provided information of what could be expected when using different energy beams. Therefore our study can be investigated further for various beam energies. The effect of concentration, location and size of nanoparticles were not investigated. Therefore a maximum DEF of 7.5% was obtained which can improve in terms of the value which can be attributed to size, location and concentration of nanoparticles selected for this study. Furthering this study can possibly produce a higher dose enhancement. For example, different target combinations were investigated and their beams had different penetrating power although the depth of NPs was the same for all the beams. Also in other previous studies it was found that an ideal diameter of GNPs should be around 50 nm which was also reported by Berrezoug *et al.* (2015). This study used gold atoms which have a diameter of approximately 0.27 nm which is smaller compared to the ideal diameter. Therefore investigating some of these factors may lead to higher dose enhancement values.

All DOSXYZnrc simulations to obtain dose distributions where run with histories between 3 x 10^9 and 6 x 10^9 ensuring the average uncertainty is below 1%. The uncertainty in the DEFs is 1.5%.

References

1. Cho SH, 2005. Estimation of tumour dose enhancement due to gold nanoparticles during typical radiation treatments: a preliminary Monte Carlo study. Phys Med Biol; 50:163–173.

2. Cho SH, Jones BL, Krisnan S, 2009. The dosimetric feasibility of gold nanoparticle-aided radiation therapy (GNRT) via brachytherapy using low-energy gamma-/X-ray sources. Phys Med Biol; 54: 4889–4905.

3. Leung MK, Chow JC, Chihrani BD *et al.,* 2011. Irradiation of gold nanoparticles by X-rays: Monte Carlo simulation of dose enhancements and the spatial properties of the secondary electrons production. Med Phys 38;2:624–631.

4. Robar JL (2006) Generation and modelling of megavoltage photon beams for contrast-enhanced radiation therapy. Phys Med Biol, 51: 5487-5504.

5. Lechtman E, Chattopadhyay N, Cai Z, *et al.,* 2011. Implications on clinical scenario of gold nanoparticle radiosensitization in regards to photon energy, nanoparticle size, concentration and location. Phys Med Biol; 56:4631–4647.

6. Robar JL, Riccio SA, Martin MA, 2002. Tumour dose enhancement using modified megavoltage photon beams and contrast media. Phys. Med. Biol; 47:2433-2449.

Chapter 7: CONCLUSIONS AND FUTURE WORK

6.1 Conclusion

The results of this study are presented to supplement data on published previous results and expand the amount of data available to direct future work in the field of using megavolt energy beams for NPs dose enhancement. The work demonstrated the possibility of using targets comprising firstly a primary target to slow down megavolt electrons, and secondly to allow these electrons to hit a secondary target made of tungsten. Water/tungsten and carbon/tungsten primary/secondary target combinations where investigated.

A flattening filter free (FFF) linac was simulated to avoid excessive beam filtering. The electron spectra obtained just after the water or carbon target was used as the incident beam to the tungsten target in the linac head. BEAMnrc was used to simulate a 6 MeV FFF Elekta precise linac head. A 6 MeV beam was selected for this study as it is one of the most frequently beams used in radiotherapy. The exit photon beams were characterised in terms of their energy spectra.

DOSXYZnrc modelled dose distributions in a water tank phantom and in a constructed patient CT phantom. Water phantom simulations were carried out to characterise the modelled photon beams from various Bremsstrahlung target combinations. A patient CT phantom which provided the actual densities of all materials found in human tissue was used to evaluate dose enhancement of altered beams in tumour seeded with gold NPs.

The results of our studies show that adding more thickness to the water or carbon target in the electron beam path before it hits the tungsten Bremsstrahlung target can alter the photon spectra by slowing down the electrons. Depending on the thickness of the target material, the population of low energy photons could be increased thereby leading to a significant dose enhancement in tumours that contain NPs.

Based on the results, carbon is more efficient at moderating the electron beam to generate photon beams for dose enhancement at a lower thickness (approximately 1.4 cm) compared to water (approximately 2.5 cm), although water can just be as good at larger thickness. At these thicknesses the mean photon beam energy is approximately 0.4 MV. For example at constant tungsten thickness (secondary target) of 0.13 cm combined with various water layers, at 0.8 cm water thickness, DEF was 1% and at a thicker water layer of 2.5 cm it was 4.6% . Also for carbon/tungsten target combination at constant tungsten target thickness (0.14 cm), a higher DEF of 6% was obtained at thicker target of 1.4 cm, and a lower DEF of 1.2% was obtained at a thinner target of 0.8 cm all for 5F plan. . The percentage combined error in dose enhancement factor values was less than 1.5% based on the number of histories simulated which were in the range of 10^9.Several factors including concentration, depth and size of nanoparticles were kept constant in this study.

Monte Carlo results obtained in this study demonstrate that carbon/tungsten Bremsstrahlung target combinations yields highest dose enhancement of approximately 7.5% whereas the one for water/tungsten is approximately 7% at a thinner tungsten layer of 0.07 cm thick. A beam from conventional linac with an unaltered Bremsstrahlung target was also investigated and a dose enhancement in tumour seeded with NPs of 0.5% was obtained, which was lower than the altered beams. Therefore the treatment beam quality also has an effect on dose enhancement. The treatment strategy also has an effect on dose enhancement. Dose enhance is quiet high using beams from oblique angles compared to anterior-posterior and lateral beams.

It is important to note that this study focused mainly on the effects of source spectra for NPs dose enhancement. The use of Monte Carlo simulations ensured the generation of electron and x-ray beams is successfully modelled. They also enabled the calculation of dose distributions in water and patient CT phantom; hence they are currently the most suitable tools for radiation dosimetry in radiation therapy. The hope is that this work provides a guide on the development of optimum condition to enhance tumour dose to NPs seeded tumours.

6.2 Future Work

Several factors to maximize NPs dose enhancement have been investigated before, therefore in this work some assumptions were made in the modeling of the tumour and tumour/nanoparticles mixture. Although these assumptions yielded results that are sufficient to explain the effect of altered beams on dose enhancement, it is important to have a more detailed model to maximize quantification of dose enhancement as well as to investigate thoroughly the clinical application of those altered beams.

Firstly it was assumed that the nanoparticles where made of atoms of gold, yet the size of nanoparticles can determine the magnitude of dose enhancement. In reality, NPs can be made of various sizes and shapes to maximize enhancement. Then, the concentration was assumed to be 7mg/g of tumour as reported by Hainfeld, which could be an effect on the values of DEFs that were obtained. The depth of the tumour was kept constant due to the 3DCRT that was used yet the modelled beams varied in their penetrating power which can lead to different DEFs. Therefore this work will be followed by investigating effects of size and concentration of nanoparticles and the effect of depth of location of nanoparticles to determine the possibly achievable maximum dose enhancement.

Nevertheless it is also worth mentioning that while this study acknowledges the limitations of determining the maximum dose enhancement achievable from altered photon spectral due to other conditions made, the work presented here provides some information that can be used in future to improve and maximize the knowledge in investigating the use of nanoparticles as option to enhance delivery of lethal dose to tumours. Lastly, the simulated results need to be verified with more biological experiments on cell lines and animal models. This will help to clarify the effects of these beams obtained using other Bremsstrahlung targets other than the conventional target on NPs in treatment of cancer cells.

APPENDICES

APPENDIX A: Permission Statement

Dr F.C.P. du Plessis
Senior Manager: Medical Physics
Universitas Hospital
BLOEMFONTEIN
Free State Our Ref. E17
Date: 28 February 2017

ELEKTA Agreement For Using Proprietary Radiation Machine Information In Research

Dear Sir,

Permission is hereby given to use proprietary information on our radiation equipment for research purposes with the following conditions;

That the information may only be used for research purposes.
That no information should be made public that could disclose the materials and exact dimensions of all components used for research purposes.
This agreement holds only for the Medical Physics department at the University of the Free State.

Yours faithfully

Yunus Munga | Business Unit Manager - Africa
Elekta (Pty) Ltd

Elekta (Pty) Ltd
2000/018814/07

Telephone
+27 11 075 1900

www.elekta.com

Maxwell Office Park
First Floor Building 3
Magwa Crescent
Waterfall City
Midrand, Johannesburg, 2090
South Africa

PostNet Suite 72
Private Bag X81
Halfway House
1685

Directors
JE Leksell (Swedish)
FG Pointurier (French)

VAT Number
402 019 1930

APPENDIX B: Detailed cross–sectional view of the Elekta Precise linac head components and the geometries used in the input files that follow.

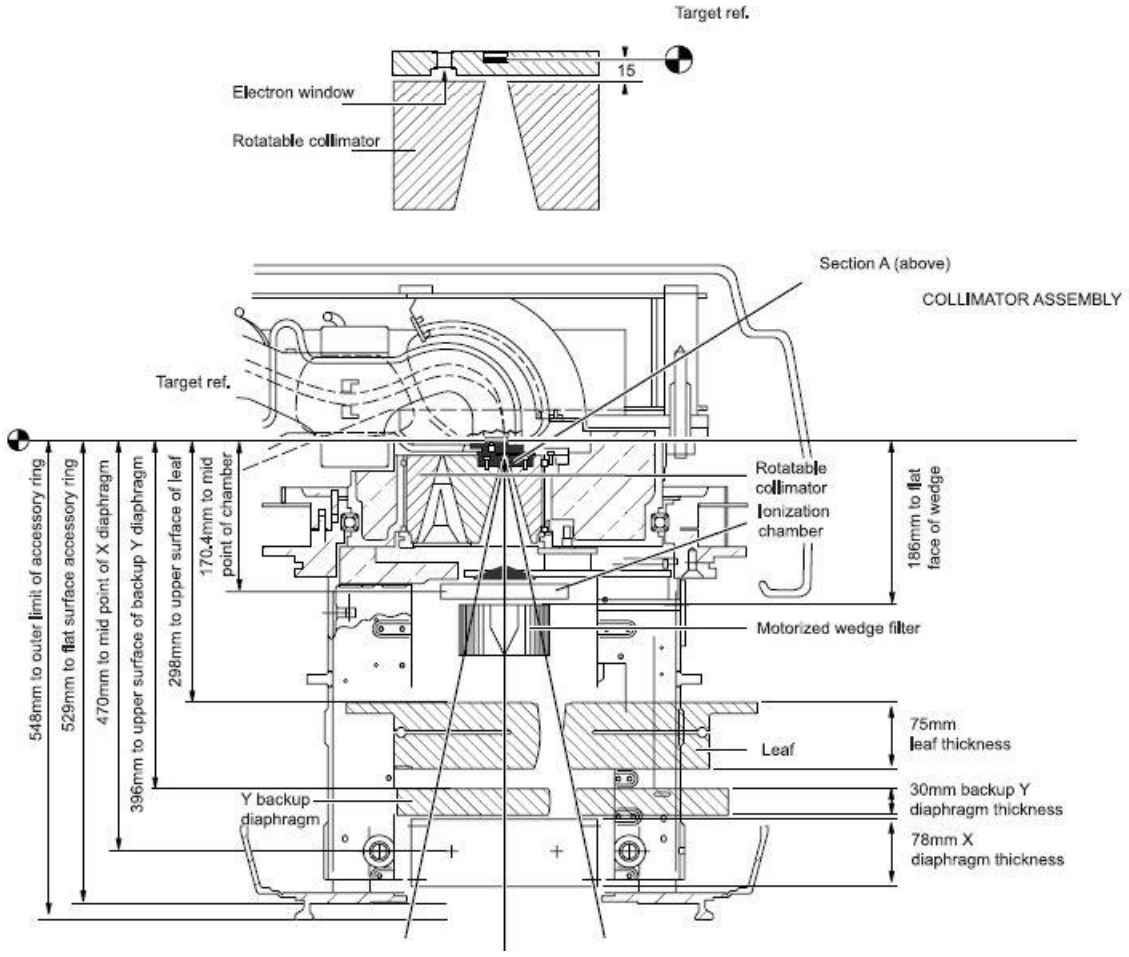

APPENDIX C: Sample input files from BEAMnrc and DOSXYZnrc MC simulations run in this work.

i) Linac head components simulation input file sample from BEAMnrc.

```
AFINAL                                                          #!GUI1.0
AIR700ICRU
0, 0, 0, 0, 0, 3, 0,  IWATCH ETC.
400000000, 330, 497, 100, 0, 0, 0, 0,  NCASE ETC.
-1, 0, 0.1, 0, 0, 1,  0.0, 0.0, 0.0, 0.0,  IQIN, ISOURCE + OPTIONS
1, SPECTRUM
/home/beamnrc/HEN_HOUSE/spectra/0h25.spectrum
1
0, 0, 0.521, 0.01, 0, 0, ,  0 , ECUT,PCUT,IREJCT,ESAVE
0, 0, 0, 0, 0,  PHOTON FORCING
1, 4,  SCORING INPUT
0,1
0,  DOSE COMPONENTS
0.0, Z TO FRONT FACE
********** start of CM SLABS with identifier targ  **********
4, RMAX
targ
1, NSLABS
0.01, ZMIN
0.07, 0.521, 0.01, 0, 1, 0
W700ICRU
********** start of CM FLATFILT with identifier primcol  **********
15, RMAX
primcol
1, ZMIN
1, NUMBER OF LAYERS
1, 10, # CONES, ZTHICK OF LAYER 1
2,
5,
0.521, 0.01, 0, 2,
AIR700ICRU
0.521, 0.01, 0, 2,
HMA700icru
********** start of CM MLCQ with identifier multleaf  **********
25, RMAX
multre
1, IDMLFC
29.8, ZMIN
7.5, ZTHICK
40, 40, # LEAVES, TOTAL WIDTH
1000, ZFOCUS(1)
17, 33.55, R0LEAF, Z0LEAF
-17, 17, 16
-20.355, 20.355, 8
-17, 17, 16
0.521, 0.01, 0, 1,
AIR700ICRU
0.521, 0.01, 0, 1,
HMA700icru
********** start of CM JAWS with identifier jolss  **********
25, RMAX
jolz
2, # PAIRED BARS OR JAWS
Y
39.6, 42.6, 3.96, 4.26, -3.96, -4.26,
X
43.1, 50.9, 4.31, 5.09, -4.31, -5.09,
0.521, 0.01, 1, 1,
0.521, 0.01, 1, 1,
HMA700icru
0.521, 0.01, 1, 1,
HMA700icru
**********end of all CMs**********
 ########################
 :Start MC Transport Parameter:

 Global ECUT= 0.521
 Global PCUT= 0.01
 Global SMAX= 5
 ESTEPE= 0.25
 XIMAX= 0.5
```

```
Boundary crossing algorithm= EXACT
Skin depth for BCA= 0
Electron-step algorithm= PRESTA-II
Spin effects= On
Brems angular sampling= Simple
Brems cross sections= BH
Bound Compton scattering= Off
Compton cross sections= default
Pair angular sampling= Simple
Pair cross sections= BH
Photoelectron angular sampling= Off
Rayleigh scattering= Off
Atomic relaxations= Off
Electron impact ionization= Off
Photon cross sections= PEGS4
Photon cross-sections output= Off

:Stop MC Transport Parameter:
##########################

```

(ii) Water phantom simulation input file sample from DOSXYZnrc .

```
6mvlinacstra                                                    #!GUI1.0
1
H20700ICRU
0.521, 0.01, 0, 0
-1, -1, -1, 1
-20
0.2, 200
-20
0.2, 200
0
0.2, 200
0, 0, 0, 0, 0, 0, 0, 0
0, 0, 0, 0, 0, 0, 0, 0
0, 0, 0, 0, 0, 0, 0, 0
2, 2, 0, 0, 0, 180, 0, 49.1, 270, 0, 0, 0, 0, 0
2, 0, 0, 49.1, 0, 0, 0, 0
/home/beamnrc/egsnrc_mp/BEAM_AFINALOUT/10hw0[illegible].egsphsp1
3000000000, 0, 100, 33, 97, 10, 1, 0, 0, 0, , 0, 0, 0, 1, 1
 ##########################
 :Start MC Transport Parameter:

 Global ECUT= 0.521
 Global PCUT= 0.01
 Global SMAX= 5
 ESTEPE= 0.25
 XIMAX= 0.5
 Boundary crossing algorithm= PRESTA-I
 Skin depth for BCA= 0
 Electron-step algorithm= PRESTA-II
 Spin effects= On
 Brems angular sampling= Simple
 Brems cross sections= BH
 Bound Compton scattering= Off
 Compton cross sections= default
 Pair angular sampling= Simple
 Pair cross sections= BH
 Photoelectron angular sampling= Off
 Rayleigh scattering= Off
 Atomic relaxations= Off
 Electron impact ionization= Off
 Photon cross sections= PEGS4
 Photon cross-sections output= Off

 :Stop MC Transport Parameter:
 ##########################

```

(iii) Patient CT phantom simulation input file sample from DOSXYZnrc .

```
6 MV Elekta                                                                    #!GUI1.0
0
/home/beamnrc/egsnrc_mp/dosxyznrc/TUMOUR.egsphant
0.521, 0.01, 0
1, 0, 0,
2, 2, 0.56, 1.19, -3.9, 90, -90, 49.1, 270, 0, 0, 0, 0, 0
2, 0, 1, 50, 0, 0, 0, 0
/home/beamnrc/egsnrc_mp/BEAM_AFINALOUT/0wc14a.egsphspl
500000000, 0, 200, 33, 97, 3, 0, 0, 1, 0, , 0, 0, 0, 1, 0
 ########################
 :Start MC Transport Parameter:

 Global ECUT= 0.521
 Global PCUT= 0.01
 Global SMAX= 5
 ESTEPE= 0.25
 XIMAX= 0.5
 Boundary crossing algorithm= PRESTA-I
 Skin depth for BCA= 0
 Electron-step algorithm= PRESTA-II
 Spin effects= On
 Brems angular sampling= Simple
 Brems cross sections= BH
 Bound Compton scattering= Off
 Compton cross sections= default
 Pair angular sampling= Simple
 Pair cross sections= BH
 Photoelectron angular sampling= Off
 Rayleigh scattering= Off
 Atomic relaxations= Off
 Electron impact ionization= Off
 Photon cross sections= PEGS4
 Photon cross-sections output= Off

 :Stop MC Transport Parameter:
 ########################
```

APENDIX D: IDL code to modify material density information in a patient CT phantom.

```
pro egs4phant,event
common block1,rho
common block2, med, region
common block3, dimxyz
common block4, xbound,ybound,zbound
common block11, tarx,tarz
common block12, cnt
common block21, angle
common block41, sliceindex
common block40, copyflag,x1arrow,y1arrow,x2arrow,y2arrow
common block47, nmed, media, estepe,medq,regq,rhoq
common block77, mask, medm
;
file = dialog_pickfile(/read,path = 'C:\Users\Medphys\Desktop\IDL_CODE - Copy (2)',filter='*.egs4phant')
;
;*************************readegsphant*************************************
;* To read egs4phant data
;*****************************************************************************
;
dimxyz = intarr(3)
nmed = intarr(1)
rhor = fltarr(10000000)
estepe = fltarr(30)
newrhor = fltarr(300,300,300)
newregion = bytarr(300,300,300)
kindex = intarr(300)
fileindex = intarr(300)
;Open egsphantfile
xyouts, 0.7, 0.25,'Reading EGS4PHANT file',/normal
openr, 1, file, /get_lun
readf,1, nmed
media = strarr(nmed)
estepe = fltarr(nmed)                    ;number of media
readf,1, media
readf,1, estepe
readf,1, dimxyz
print, nmed
print, dimxyz
xbound = fltarr(dimxyz(0)+1)
ybound = fltarr(dimxyz(1)+1)
zbound = fltarr(dimxyz(2)+1)
med = bytarr(dimxyz(0),dimxyz(1),dimxyz(2))
mask = bytarr(dimxyz(0),dimxyz(1),dimxyz(2))
medq = bytarr(dimxyz(0))
medm = bytarr(dimxyz(0))
region = intarr(dimxyz(0),dimxyz(1),dimxyz(2))
regq = intarr(dimxyz(0))
rho = fltarr(dimxyz(0),dimxyz(1),dimxyz(2))
rhoq = fltarr(dimxyz(0))
space = strarr(1)
tarx = fltarr(3000)
tarz = fltarr(3000)
cnt = intarr(1)
;
readf,1, xbound
readf,1, ybound
readf,1, zbound
;print,xbound
;print,ybound
;print,zbound
voxsize = abs(xbound(1)-xbound(2))
voxyzize = abs(ybound(1)-ybound(2))
zvoxelsize = abs(zbound(1)-zbound(2))
;
;read in the media data
;
for k = 0, dimxyz(2)-1 do begin
for j = 0, dimxyz(1)-1 do begin
READF, 1, $
   FORMAT = '(300I1)', medq
for i = 0, dimxyz(0)-1 do begin
med(i,j,k) = medq(i)
endfor
endfor
readf,1,space
endfor
;readf,1,space
xyouts, 0.7, 0.2,'Completed reading media',/normal
;
;Reading in media density data
;
for k = 0, dimxyz(2)-1 do begin
for j = 0, dimxyz(1)-1 do begin
READF, 1, rhoq
for i = 0, dimxyz(0)-1 do begin
rho(i,j,k) = rhoq(i)
endfor
endfor
```

```
readf,l,space
endfor
;readf,l,space
xyouts,0.7, 0.15,'Completed reading media densities',/normal
;
;Reading in volumes to change media data of EGS4PHANT file.
;
for k = 0, dimxyz(2)-1 do begin
for j = 0, dimxyz(1)-1 do begin
READF, l, $
   FORMAT = '(300I2)', medm
for i = 0, dimxyz(0)-1 do begin
mask(i,j,k) = medm(i)
;put Titanium in the mask
if (mask(i,j,k) eq 1) then begin
med(i,j,k) = nmed + 1
rho(i,j,k) = 1.6025
endif
endfor
endfor
readf,l,space
endfor
;
xyouts,0.7, 0.1,'Completed reading mask data',/normal
;
;Now we display regions and media in one window and select slices with slider
;
win1=widget_base(title='image display selection',/column)
copyflag = 0
xslider = widget_slider(win1,min = 0, max = dimxyz(2),title = 'select slice',event_pro='showslice',xsize=350)
checkplan3 = widget_button(win1,value='write EGS4PHANT file',event_pro='egs4phantwrite')
widget_control,win1,/realize
state1 = {xslider:xslider}
widget_control, win1,set_uvalue=state1
free_lun,l
END

pro showslice,event
common block1, rho
common block2, med, region
common block3, dimxyz
common block4, xbound,ybound,zbound
common block5, res
common block6, slice
 common block11, tarx,tarz
 common block12, cnt
 common block13, zslice
 common block40, copyflag,x1arrow,y1arrow,x2arrow,y2arrow
 common block41, sliceindex
 common block47, nmed, media, estepe,medq,regq,rhoq
 common block77, mask, medm
 widget_control, event.top, get_uvalue = state1
 widget_control, state1.xslider, get_value = slice
 slice = round(slice)
 zslice = slice
 y = fltarr(10,3000)
 z = fltarr(10,3000)
 window,0,xsize = dimxyz(0)*2,ysize = dimxyz(1)*2
 xs = dimxyz(0)*2 & ys = dimxyz(1)*2
 result = congrid(rho(*,*,zslice) + med(*,*,zslice), dimxyz(0)*2, dimxyz(1)*2,/interp)
 tvscl, result
 xyouts, 0.1,0.7,string('z=',zbound(zslice))
 end

 pro egs4phantwrite,event
 common block1, rho
 common block2, med, region
 common block3, dimxyz
 common block4, xbound,ybound,zbound
 common block5, res
 common block6, slice
 common block11, tarx,tarz
 common block12, cnt
 common block13, zslice
 common block40, copyflag,x1arrow,y1arrow,x2arrow,y2arrow
 common block41, sliceindex
 common block47, nmed, media, estepe,medq,regq,rhoq
 estepeout = fltarr(nmed+1)
 common block77, mask, medm
 wset,0
 xyouts, 0.1, 0.25,'Writing EGS4PHANT file',/normal
 file = 'C:\Users\Medphys\Desktop\IDL_CODE - Copy (2)\AuGoICRU700.egs4phant'
 openw, 1, file, /get_lun
 printf,1, nmed + 1
 printf,1, media(0)
 printf,1, media(1)
 printf,1, media(2)
 printf,1, media(3)
 printf,1,'Gold7ICRU700'
 estepeout(*) = 1.0000
 printf,1, estepeout
 printf,1, dimxyz
 printf,1, format = '(300(f7.3," "))',xbound
 printf,1, format = '(300(f7.3," "))',ybound
 printf,1, format = '(800(f7.3," "))',zbound
 ;
```

```
;writing media data
;
for k = 0, dimxyz(2)-1 do begin
for j = 0, dimxyz(1)-1 do begin
for i = 0, dimxyz(0)-1 do begin
medq(i) = med(i,j,k)
endfor
printf, l, $
   FORMAT = '(300I1)', medq
endfor
printf,l,' '
endfor
;
xyouts, 0.2, 0.2,'Completed writing media',/normal
;
;Reading in media density data
;
for k = 0, dimxyz(2)-1 do begin
for j = 0, dimxyz(1)-1 do begin
for i = 0, dimxyz(0)-1 do begin
rhoq(i) = rho(i,j,k)
endfor
printf,l,format='(300(f8.2," "))',rhoq
endfor
printf,l,' '
endfor
;
xyouts,0.3, 0.15,'Completed writing media densities',/normal
;
;Reading in DVH regions of interest
;
for k = 0, dimxyz(2)-1 do begin
for j = 0, dimxyz(1)-1 do begin
for i = 0, dimxyz(0)-1 do begin
regq(i) = region(i,j,k)
endfor
printf,l,format='(300(I1," "))',regq
endfor
printf,l,' '
endfor
;
xyouts,0.4, 0.1,'Completed writing region data',/normal
xyouts,0.3, 0.1,'Completed writing EGS4PHANT file',/normal

end

pro exit,event
widget_control,event.top,/destroy
exit
end

pro editegs4phantfile
```

APPENDIX E: dcombine.f a FORTRAN code to combine 3D dose files from DOSXYZnrc simulations.

```
c   dcombine.f
c   Code combines .3ddose files

    Integer IMAX,JMAX,KMAX,nfiles,nf
    Real dose(340,340,340),errors(340,340,340)
    Real xbound(340),ybound(340),zbound(340)
    Real dosecomb(340,340,340), errcomb(680,680,680)
    Real err(680,680,680)
    Character*60 fnam(40)

    write(*,*) 'Number of files to add:'
    read(*,*) nfiles

        do nf=1,nfiles

        write(*,*) 'Give name of file',nf,':'
        read(*,*) fnam(nf)

    Open(unit=12,file=fnam(nf),access='sequential',status='unknown')

        Read(12,*)IMAX,JMAX,KMAX

        Read(12,*) (xbound(I),I=1,IMAX+1)
        Read(12,*) (ybound(I),I=1,JMAX+1)
        Read(12,*) (zbound(I),I=1,KMAX+1)

        Read(12,*) (((dose(i,j,k),i=1,IMAX),j=1,JMAX),k=1,KMAX)
        Read(12,*) (((errors(i,j,k),i=1,IMAX),j=1,JMAX),k=1,KMAX)

        write(*,*) nf,'succesfully read'

    Close(12)

    Do 110 i = 1, IMAX+1
    Do 210 j = 1, JMAX+1
    Do 310 k = 1, KMAX+1

    dosecomb(i,j,k) = dosecomb(i,j,k) + dose(i,j,k)
    err(i,j,k) = err(i,j,k)**2 + errors(i,j,k)**2

310 Continue
210 Continue
110 Continue

    enddo

    Do 410 i = 1, IMAX+1
    Do 510 j = 1, JMAX+1
    Do 610 k = 1, KMAX+1

    errcomb(i,j,k) = (sqrt(err(i,j,k))) / nfiles

610 Continue
510 Continue
410 Continue


    Open(unit=13,file='c_dose.3ddose',access='sequential',
     &  status='unknown')

        Write(13,*)IMAX,JMAX,KMAX

        Write(13,*) (xbound(I),I=1,IMAX+1)
        Write(13,*) (ybound(I),I=1,JMAX+1)
        Write(13,*) (zbound(I),I=1,KMAX+1)

        write(13,*) (((dosecomb(i,j,k),i=1,IMAX), j=1,JMAX),k=1,KMAX)

        write(13,*) (((errcomb(i,j,k),I=1,IMAX),J=1,JMAX),K=1,KMAX)

    Close(13)

    write(*,*) 'Dose combined in file: c_dose.3ddose'

    End
```

AUTHOR'S BIOGRAPHY

Stalyn Mutsakanyi was born on May 22, 1983 at St Paul's Mission Hospital in Murewa and grew up in Harare, Zimbabwe. He attended all his primary and secondary education in Harare and then attended National University of Science and Technology in Bulawayo, Zimbabwe and received a Bachelor of Science (Hons) degree in Applied Physics in 2008. After graduation Stalyn went on to teach mathematics, physics and chemistry at various high schools in the neighboring country South Africa from year 2009 to 2012. In 2013 he joined University of Pretoria, South Africa, to study a BSc Honours Medical Physics degree that was completed the same year. In July 2014 he joined University of the Free State, South Africa, to carry a research in medical physics to present. After completion of graduate work, Stalyn plans to pursue a PHD in Medical Physics.